Magnetically levitated planar actuator with moving magnets: Electromechanical analysis and design

PROEFSCHRIFT

ter verkrijging van de graad van doctor aan de
Technische Universiteit Eindhoven, op gezag van de
Rector Magnificus, prof.dr.ir. C.J. van Duijn, voor een
commissie aangewezen door het College voor
Promoties in het openbaar te verdedigen
op woensdag 28 november 2007 om 16.00 uur

door

Jacob Willem Jansen

geboren te Wijchen

Dit proefschrift is goedgekeurd door de promotoren:

prof.dr.ir. A.J.A. Vandenput
en
prof.dr.ir. P.P.J. van den Bosch

Copromotor:
dr. E.A. Lomonova MSc

Coverdesign by AtelJ van Lierop Bladel and Studio Interpoint Netersel

Abstract

Magnetically levitated planar actuator with moving magnets: Electromechanical analysis and design

Magnetically levitated planar actuators are developed as alternatives to xy-drives, which are constructed of stacked linear motors in high-precision industrial applications. The translator of these planar actuators is suspended above the stator with no support other than magnetic fields. Because of the active magnetic bearing the translator can move in six degrees-of-freedom. This thesis presents the electro-mechanical analysis and design of a contactless, magnetically levitated, planar actuator with moving magnets. This planar actuator consists of a stationary coil array with concentrated non-overlapping windings and a translator with a permanent-magnet array with a quasi-Halbach magnetization. As only the coils below the magnet array can produce significant force and torque, the set of active coils is switched during the movements of the translator in the xy-plane. As a result, the stroke in the xy-plane can be made, in theory, infinitely long.

The ironless planar actuator has a three-dimensional, non-periodical and non-symmetrical electromechanical structure, which require a multi-physical approach to analyze. To predict the force and torque in this type of structures, three different magnetostatic models have been developed. These models differ in accuracy and calculation time, and are applied for the analysis, design and control of the planar actuator. The models are based on different analytical solutions of the magnetic flux density distribution of the permanent magnet array and on both analytical and numerical solutions of the Lorentz force and torque integrals.

Due to the integration of propulsion in the xy-plane with an active magnetic bearing, standard decoupling schemes for synchronous machines cannot be applied

in the planar actuator to decouple and linearize the force and the torque. To commutate the planar actuator a method has been developed which inverts a fully analytical mapping of the force and torque exerted by the active coils as function of the position and orientation of the translator using a minimal energy constraint and smooth weighing function to enable switching between different coils sets. The resulting current waveforms in the individually excited coils are non-sinusoidal.

The synthesis and design process of the planar actuator has been split into two steps. As the power dissipation is an important design criterion, the dimensions of the permanent magnets and coils have been optimized to maximize the efficiency of the force production. Design rules have been established for the magnet and coil dimensions. Subsequently, several planar actuator configurations have been synthesized with these optimized coil and magnet dimensions. The power dissipation and the force and torque ripples of these actuators have been compared. Furthermore, the causes of the force and torque ripples have been identified.

Based on the comparison, a planar actuator with rectangular coils arranged in a herringbone pattern has been selected and this actuator has been manufactured. The actuator has 84 coils in total, of which 24 are simultaneously used for the propulsion and levitation of the translator. The three magneto-static models and the commutation algorithm have been verified and the planar actuator has been successfully tested.

Contents

Chapter 1

Introduction

Flying has fascinated mankind for ages. In amongst others the Arab mythology, flying or magic carpets can be found [7]. These carpets float above the ground and are used for traveling. The planar actuator described in this thesis has similarities with these legendary carpets. A plate with permanent magnets, the carpet, is levitated above an array of coils. The plate has an, in principle, unlimited stroke in the horizontal plane. Instead of magic, magnetic fields are applied to levitate and to propel the carpet.

1.1 Background

Many industrial apparatus, e.g. semiconductor lithography scanners, pick-and-place machines and inspection systems are equipped with accurate positioning systems. Usually, these multi-degree-of-freedom (DOF) positioning systems are constructed of stacked long- and short-stroke single-degree-of-freedom linear and rotary drives, which are supported by roller or air bearings. An example of such a system is shown in Figure 1.1. This xy-positioning system consists of three linear motors. Two linear motors are placed in parallel and move in the y-direction (indicated with $y1$ and $y2$ in Figure 1.1). The third motor (indicated with x in Figure 1.1) is mounted in between the $y1$- and $y2$-translators and can move in the x-direction. Because of its shape, this positioning system is called an H-drive. The H-drive is amongst others applied in pick-and-place machines for the assembly of printed circuit boards. To obtain a high servo bandwidth, the system is stiff and, as a result, the moving mass is large compared to the load. Because of the demand
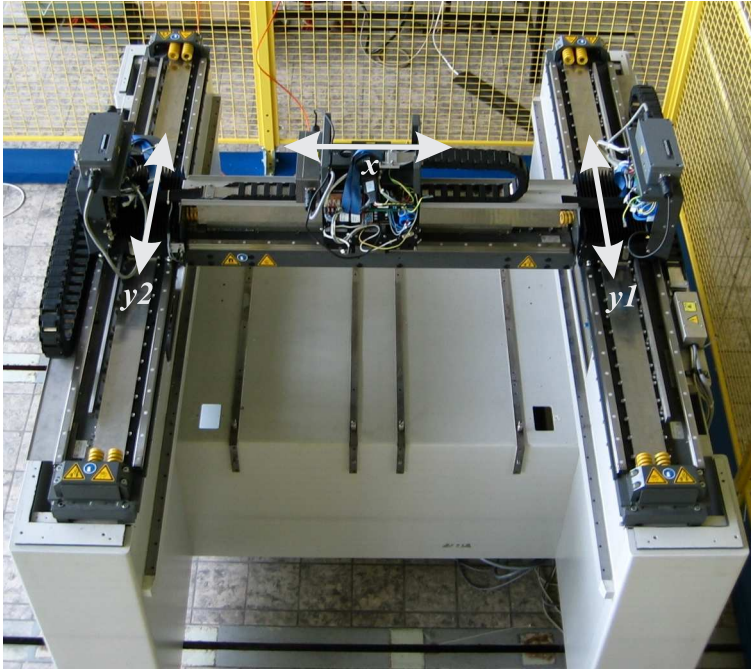
Figure 1.1. *Assembléon H-drive: xy-positioning system with three linear motors (laboratory EPE).*

for a high throughput, the acceleration levels, and, consequently, the required force levels are high. Instead of stacking one-degree-of-freedom drives, multiple degrees-of-freedom can be combined in one actuator. An example of such a drive is a planar actuator, which has a single translator that is magnetically levitated and moves in the xy-plane over the stator surface (Figure 1.2). Because of the lower moving mass, the force levels can be significantly reduced.

In recent years, planar actuators became of interest to the semiconductor industry, which is constantly striving for smaller devices, that contain more functionality for a lower price. A shorter wavelength of the light, which is used in the lithographical steps, allows for smaller features on the chips. Currently, lithography systems are developed and tested which have an extreme-ultraviolet light source. To prevent contamination of optical elements and absorption of the extreme-ultraviolet
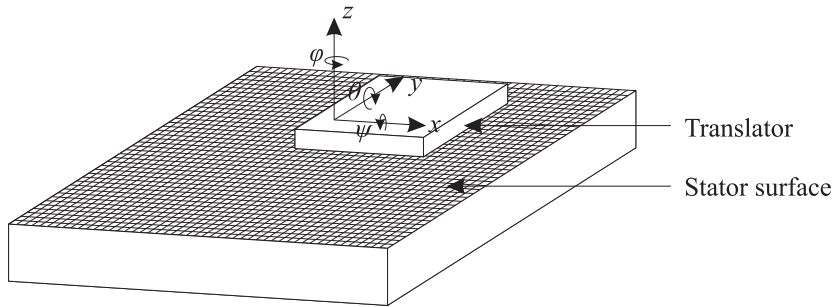
Figure 1.2. *Planar actuator.*

light by air, the wafers (silicon substrates) are exposed in a high-vacuum environment [47]. To accurately position the wafers in vacuum, magnetically levitated planar drives have been researched [48, 14, 28, 49, 15]. Because of the magnetic bearing, the vacuum is not contaminated by lubricants and there is no mechanical wear. The planar actuator is controlled in six degrees-of-freedom, and consequently, the translator can not only be positioned in the xy-plane but also the orientation in three degrees-of-freedom and the z-position can be adjusted. Contrary to other magnetically levitated systems, such as active magnetic bearings for rotary machine shafts and magnetically levitated trains, there is no physical decoupling of the levitation and the propulsion functions. These functions are controlled by the same coils and magnets.

As any permanent-magnet machine, planar actuators can be constructed in two ways. They have either moving coils and stationary magnets, or moving magnets and stationary coils. Figures 1.3 and 1.4 show artist's impressions of these two respective actuator types. Contrary to a moving-coil planar actuator, the translator of the moving-magnet planar actuator is truly contactless because no cable to the moving part is necessary, since the coils, which require power and cooling, are on the stationary part of the actuator. Consequently, the disturbances on the translator are significantly reduced. The advantage of a moving-coil planar actuator is that the stroke in the xy-plane can be simply increased by adding extra magnets to the magnet array and only a small amount of power amplifiers, which are expensive components, are needed to supply the coils. In a moving-magnet planar actuator, only the coils below and near the edges of the magnet array can exert force and torque on the magnet array. When long-stroke motion in the xy-plane is desired,
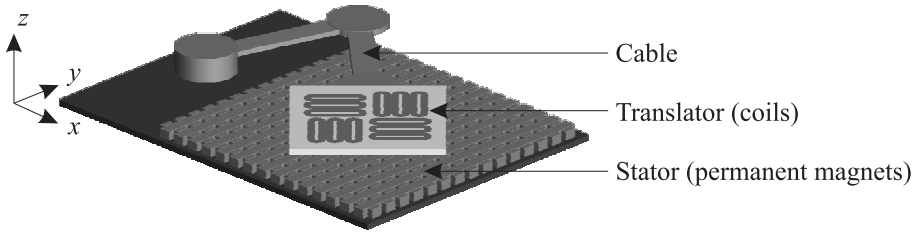
Figure 1.3. *Moving-coil planar actuator [14].*
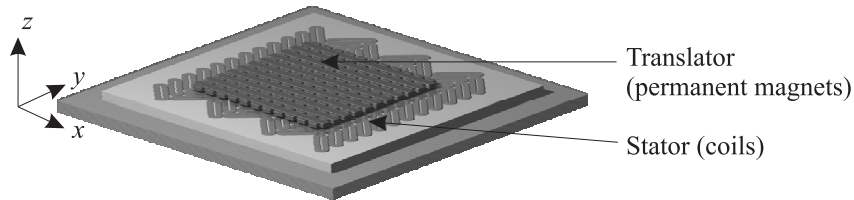
Figure 1.4. *Moving-magnet planar actuator [38].*

the set of active coils has to be switched.

Because of the integration of bearing and propulsion and the necessity to switch between different sets of active coils, a dedicated control strategy should be applied and, therefore, these planar actuators can be considered as a new and special class of multi-phase synchronous permanent-magnet motors.

1.2   Research goal and objectives

The goal of this project is to create the theory for this new class of actuators and to realize a long-stroke, magnetically levitated planar actuator with moving-magnets. The long-stroke movement in the xy-plane is achieved by switching between coil sets and, therefore, the stroke in the xy-plane can be enlarged by adding extra stator coils, without the necessity to redesign the actuator. Due to the switching between different coil sets, the effective electromechanical configuration of the planar

actuator changes constantly. Nevertheless, the produced force and torque should not be affected by it. This last requirement can only be met by combining the fields of electromechanics and control engineering in the design of the planar actuator.

This general project objective is split into four sub-objectives:

1. *The modeling and analysis of the force and torque in the planar actuator.*
   The torque and force in rotary and linear motors are obtained from the analysis of the electromagnetic phenomena in the airgap of the motor. The complexity of the problem can usually be reduced by applying periodical boundary conditions and simplifying the three-dimensional magnetic flux density distribution to a one- or two-dimensional distribution. Both simplifications cannot be applied to planar actuators because of the truly three-dimensional magnetic flux density distribution and the non-periodical magneto motive force. In order to analyze fast the force and torque acting in the ironless planar actuator, not the magnetic fields in the airgap are considered of primary interest but the Lorentz force and torque, as calculating these quantities only requires the prediction of the magnetic flux density distribution of the permanent magnets.

2. *Research into commutation strategies, which decouples and linearizes the force and torque in the planar actuator.*
   In the control of electrical machines, transformations, e.g. Park's transformation, are applied to linearize the torque or force. As a result, the torque or force in the commutated electrical machine can be controlled similar to a DC-motor. When Park's transformation is applied to the 6-DOF planar actuator, it would only decouple the force components and not the torque components. To decouple them both, a new transformation has been investigated. For this transformation, a model based approach is selected.

3. *Research into design methodologies for moving-magnet planar actuators.*
   The design of electrical machines starts usually from standard sizing equations, which consider amongst others, the volume, the magnetic, electrical and thermal loading of the machine and the torque or force requirements. As the planar actuator is also a magnetic bearing, the force and torque requirements depend on the mass of the levitated object. Moreover, the levitated mass itself consists for a considerable part of permanent-magnets, which define the magnetic loading. For this reason, the standard sizing equations are not translated to planar actuators and a different design approach is chosen. Because of the linear material properties, the superposition principle can be applied to the force and torque calculation in the planar actuator and the coil and magnet sizes are optimized first. Sec-

ondly, planar actuators are synthesized with these coils and magnets and the controllability is verified. Finally, the performance of the commutated planar actuators is analyzed in terms of power dissipations and the force and torque ripples.

4. *The realization and test of a prototype.*

    Validation of an electrical machine design is often carried out with finite element analyses. Due to the long calculation time, the analysis of large planar actuator design is not practical with finite element packages. Because of that, a prototype is realized to validate the design and the analysis tools. As measurements on the realized actuator are the only way to accurately validate the models and design, it is produced with tight tolerances.

The research has been carried out by two PhD students and the results are described in two theses. This thesis focusses on the modeling and design of the planar actuator, whereas the thesis of Nelis van Lierop [73] focusses on the commutation, the controllability of planar actuator designs and the controllers of the realized planar actuator.

1.3   Organization of the thesis

Chapter 2 gives an overview of magnetic levitation techniques and the state-of-art of magnetically levitated planar actuator technology. A magneto-static modeling framework of ironless planar actuators is presented in Chapter 3. The framework includes three different models, which are used for the analysis, design and real-time control of the planar actuator, respectively. Because of the three-dimensional structure of the planar actuator, reduction of the calculation time of the models is considered an important issue. In this chapter also the two basic coil and magnet configurations are discussed. Chapter 4 explains the commutation strategy for planar actuators. This decoupling and linearization algorithm allows to smoothly switch between different sets of active coils. The algorithm is based on the analytical model obtained in Chapter 3. Chapter 5 describes a design methodology for planar actuators. In the optimization the planar actuator is not considered as a poly-phase machine, but as an assembly of independent short-stroke linear actuators of which the dimensions have been optimized. Next, several planar actuator topologies are compared. In the comparison, the commutation algorithm is taken into account. Several important design issues are addressed in Chapter 6. The working points of the permanent magnets, eddy-current damping, thermal aspects and the selection of the power amplifiers are discussed. In Chapter 7, the models and algorithm derived in Chapter 3 and 4 are validated on the realized planar ac-

tuator. Furthermore, the behavior of the planar actuator under 6-DOF control is presented. Conclusions of the research and recommendations for future work are given in Chapter 8.

Chapter 2

Magnetically levitated planar actuator technology

Both magnetic bearing systems and planar actuators are known for many years. Research into magnetic levitation has been conducted since the end of the 19th century [44]. Magnetic bearings are applied to support, for example, high-speed machine shafts and trains. The advantage of a magnetic bearing over a mechanical bearing is that there is no contact, no mechanical wear and low friction.

In 1968 an early planar actuator patent was filed [64]. This planar switched-reluctance motor was developed for an xy-plotter. Afterwards, also planar permanent-magnet motors [2, 30] and planar induction motors [21] have been developed. These planar or surface motors have either two degrees-of-freedom (the actuator can move in the xy-plane) or three degrees-of-freedom (the actuator can move in the xy-plane and rotate about the z-axis). The actuators are supported by air or other mechanical bearings.

The integration of both techniques, however, is only investigated in recent years. In this chapter an overview of magnetic levitation techniques is given and the state-of-art of magnetically levitated planar actuators is discussed. Three types of planar actuators are distinguished. Planar actuators constructed of several multi-DOF actuator segments, planar actuators with multiple layers of long coils and planar actuators with short coils. A number of these actuators is only described in the patent literature. Consequently, a comparison of these actuators cannot be made.

2.1   Principles of magnetic levitation

Magnetic levitation or suspension is a technique to suspend an object with no other support than an electromagnetic field. An extensive overview of magnetic suspension techniques is given in [44]. In [44], nine different levitation techniques are distinguished. In the field of electrical machines only two types are of interest: electromagnetic suspension with a static magnetic field and electrodynamic suspension, which uses induced currents.

2.1.1   Electromagnetic suspension

In 1842, Samuel Earnshaw proved that passive levitation with static magnetic fields is not possible [18]. To stabilize a magnetically levitated system, a feedback controller is required. There is one exception to this rule. When a part of the system contains diamagnetic materials, which have a relative permeability $\mu_r < 1$, passive levitation is possible. Bismuth and water are examples of diamagnetic materials. An ideal diamagnetic material is a superconductor ($\mu_r = 0$), as superconductors reject magnetic fields, which is called the Meissner effect.

An example of an electromagnetic suspension system is shown in Figure 2.1. An iron ball is suspended below an electromagnet. The gravitational force on the ball is compensated by the attraction force of the electromagnet. The distance between the ball and the electromagnet is measured with an optical sensor and the current i is controlled by a feedback controller. This magnetic suspension system is based on the reluctance force. The reluctance force originates from the change of the reluctance in a magnetic circuit. This bearing can be pre-stressed by a permanent magnet in the ball, which creates a bias field. The advantage of this hybrid magnetic bearing, which contains both electromagnets and permanent magnets, is that a certain distance between the ball and the electromagnet, the attraction force created by the permanent magnet compensates the gravitational force. When the ball is controlled at that position, the electromagnet should only counteract the disturbances. Hence, the power dissipation in the electromagnet is small.

The reluctance force can only attract iron objects and not repel them. To repel objects a bearing based on the Lorentz force, which is also called the Laplace force, can be used. The Lorentz force is the force on a current carrying conductor in an external magnetic field. The Lorentz force $\vec{F}$ is expressed as:

$$\vec{F} = \int_V \vec{J} \times \vec{B} \mathrm{d}V, \tag{2.1}$$

where $\vec{J}$ is the current density in the conductor, $\vec{B}$ is the magnetic flux density
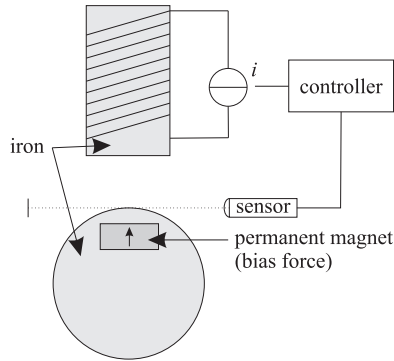
Figure 2.1. *Magnetically levitated ball.*

distribution not originated from the current in the conductor, and V is the volume of the conductor. In Figure 2.2 the principle of such a bearing is shown. Figure 2.2 shows a stationary magnet array with its flux lines and two coils. The Lorentz force on the conductors are indicated by the arrows. Both levitation force in the z-direction, which is proportional to the B_x-component of the magnetic flux density, and propulsion force in the x-direction, which is proportional to the B_z-component, can be produced. The direction of the force vector is dependent on the position of the coil with respect to the magnets. This magnetic bearing is not pre-stressed by a bias flux. Consequently, power is constantly dissipated in the coils to overcome gravity.

When the Lorentz force is applied for levitation, no back-iron behind the coils is used because the iron will be attracted by the permanent-magnet array. To increase and concentrate the magnetic flux density near the coils, a Halbach permanent-magnet array could be applied. Although Halbach magnet arrays were originally developed for particle accelerators [25], this type of magnet array is also used in electrical machines. Machines with a Halbach magnet array have a sinusoidal airgap flux density distribution and do not require back-iron [79]. Figure 2.2 shows the flux lines of a magnet array with only north-south (NS) oriented magnets. The flux lines of a magnet array with a quasi-Halbach magnetization with two magnet segments per pole are shown in Figure 2.3. The horizontally magnetized magnets in this magnet array focus the flux lines to the top side of the magnet array where the magnet flux density levels are increased compared with those of the NS-array.
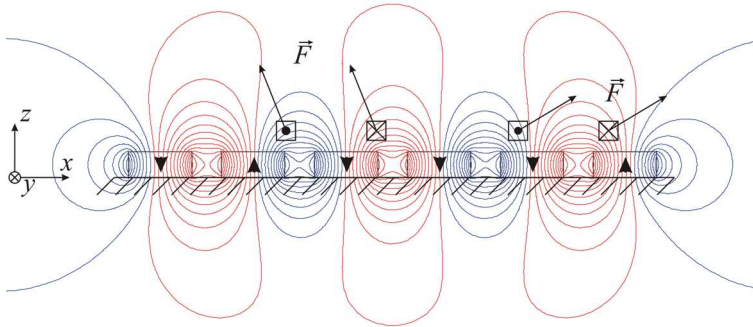
Figure 2.2. *Lorentz force on current carrying conductors in a magnetic field of a NS magnet array.*
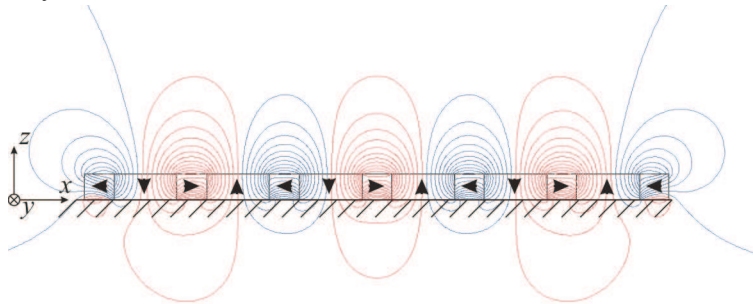
Figure 2.3. *Flux lines of a quasi-Halbach magnet array with two magnet segments per pole.*

2.1.2   Electrodynamic suspension

In electrodynamic suspension systems a repulsion force originates from an electromagnetic wave and the currents induced in a conductor by that wave. The currents are induced when there is a speed difference between the electromagnetic wave and the conductor. Electrodynamic suspension is, for example, used in magnetically levitated trains. The excitation field can be generated either by superconducting coils [63] or permanent magnets [24] on the train itself. At low speeds, the generated force is not sufficient to levitate the train. Therefore, these trains are supported by

wheels or electromagnets during standstill and start-up. The characteristic of the force is strongly non-linear and, therefore, this type of levitation is not applied in positioning systems and will not be further discussed in this thesis.

2.2 Magnetically levitated planar actuators constructed of multi-DOF actuator segments

There are different ways to build six degree-of-freedom magnetically levitated planar actuators. A method is to combine several multi-degree-of-freedom actuator segments or forcers. Each forcer can produce a levitation force and a propulsion force. This construction is both applied in short-stroke moving-magnet and long-stroke moving-coil planar actuators.

2.2.1 Planar magnetic levitator

One of the first moving-magnet planar actuators for photo-lithography applications was developed in the mid-nineties [48]. This planar levitator consists of four two-degree-of-freedom actuator segments, which are called linear motor bearings. Figure 2.4 shows a linear motor bearing with two controlled degrees-of-freedom. The bearing segment consists of a stationary coil array with a three-phase winding and a moving Halbach magnet array. The magnet array is levitated (z-direction) and can be propelled in the x-direction. The actuator is ironless. The force can be calculated by the Lorentz force law. The force components in the x- and z-directions are decoupled by the $dq0$-decomposition. The propulsion force is proportional to the q-axis current component and the levitation force to the d-axis current component. In section 4.1, the application of the $dq0$-decomposition in planar actuators will be further analyzed.

Four of these linear motor bearings are combined to a six degree-of-freedom short-stroke magnetically levitated planar actuator. A top view of this actuator is shown in Figure 2.5. The levitated platen contains four Halbach magnet arrays. Each magnet array should stay above its own coil array. Consequently, the stroke of this actuator is limited (50x50 mm). An increase of the stroke would require both a redesign of the stator and the translator. Segments I and III can produce force in the y-and z-directions, and segments II and IV in the x- and z-directions. The platen, which has a mass if 5.5 kg, is levitated 250 μm above the coils. At standstill levitation, the rms-position accuracy is less than 30 nm and the power dissipation is equal to 21.6 W.

The disadvantage of this planar magnetic levitator is that only the top side
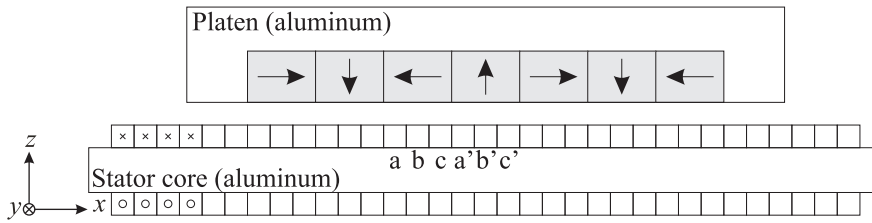
Figure 2.4. *Cross-section of a linear motor bearing [48].*
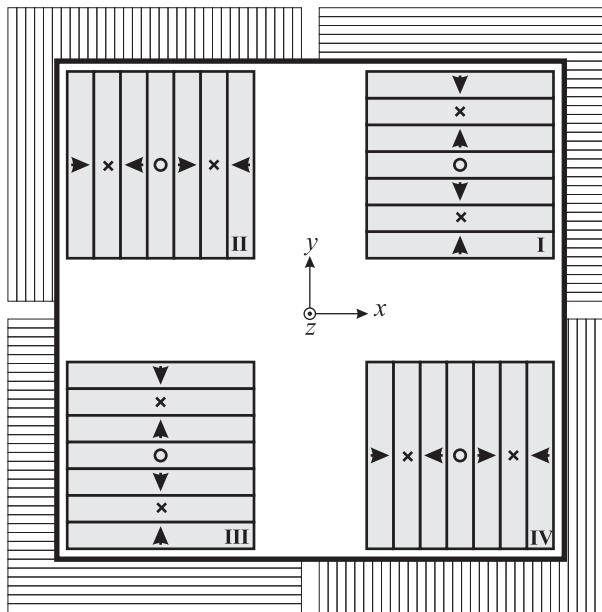
Figure 2.5. *Planar magnetic levitator constructed of four linear motor bearings [48].*

of the coils, which are near the magnet array produce significant force. Because the coils are wound around a non-laminated aluminum core, eddy currents are induced in the core by both time-varying currents in the coils and movement of the translator. The last effect causes damping.

A similar actuator but with a 90 kg moving part is described in [19]. In [45],
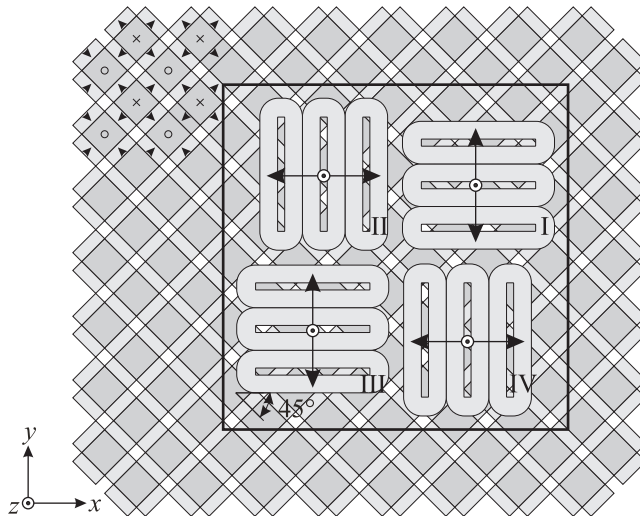
Figure 2.6. *Electro-dynamic planar actuator with moving coils [13].*

a 6-DOF planar actuator is described, in which the same coil and magnet configuration is only applied for production of the propulsion force in the xy-plane. The iron platen is suspended by four electromagnets, which are installed above the platen. A moving-magnet planar actuator with mechanical bearings and a comparable configuration is presented in [65].

2.2.2   Electrodynamic planar motor

The electrodynamic planar motor [13, 14] is a moving-coil planar actuator with a stationary magnet array. It has been developed for a wafer stage of an extreme ultraviolet lithography system. Figure 2.6 shows a top view of this planar actuator. Similar to the planar magnetic levitator (section 2.2.1, [48]), four groups of coils or forcers with a three-phase winding can be recognized. The forcers have two different orientations in the xy-plane. Contrary to [48], all forcers use the same magnet array. This is realized by rotating the coils 45 mechanical degrees with respect to the two-dimensional Halbach permanent-magnet array. As a result, this actuator has an infinitely long stroke in the xy-plane. This coil orientation will be further discussed in section 3.8.

Each of the four forcer is connected to a three-phase power amplifier. Each forcer can produce a force in the z-direction and a force in the x-direction (forcers II and IV) or y-direction (forcers I and III), as indicated by the arrows in Figure 2.6. The locations of the center of each forcer with respect to each other are optimized to cancel the torque produced by the individual forcers, under the condition that forcers I and III and forcers II and IV produce the same force vectors, respectively. When the torque arm in the z-direction cannot be neglected, this condition is not fulfilled during acceleration in the xy-plane. In that case, an advanced feedforward controller should prevent the production of torque components.

A moving-coil planar actuator with mechanical bearing and the same coil configuration is described in [10].

2.3   Magnetically levitated planar with multiple orthogonal layers of long coils

The disadvantage of constructing moving-magnet planar actuators of multiple two-dimensional actuator segments is that the stroke is fundamentally limited. When the actuator segments are integrated or stacked in multiple layers, the stroke of such planar actuator can be increased without the necessity to redesign the translator. Such a configuration for moving-magnet planar actuator is shown in Fig. 2.7. This planar actuators has two layers of coreless coils, one layer conducts the current in the x-direction (and is capable of producing force in the y-and z-directions) and one layer conducts the current in the y-direction (and is capable of producing force in the x-and z-directions). The figure shows two possible translator configurations.

Planar actuators with this concept and mechanical bearings have been studied by [20] (translator type 1) and [54, 70] (translator type 2). Magnetic levitation of the mover of the latter actuator has also been investigated [71]. In [49] a magnetically levitated planar actuator with a translator with a magnet array comparable to translator type 2 is proposed. This actuator has six layers of coils, each coil controlling a different degree-of-freedom. In [11] a planar actuator with translator 1 is presented, in which the translator is magnetically suspended by three electromagnets placed above the translator. The coreless propulsion coils were realized in a printed circuit board.

The concept with multiple coil layers has several disadvantages. Because the coils cover the whole length of the stator, only a single translator can be controlled above one stator. Another disadvantage of the coil configuration is that the coil layers have a different distance to the magnet array. As the magnetic flux density declines with the distance, the ohmic losses in the coils located further from the
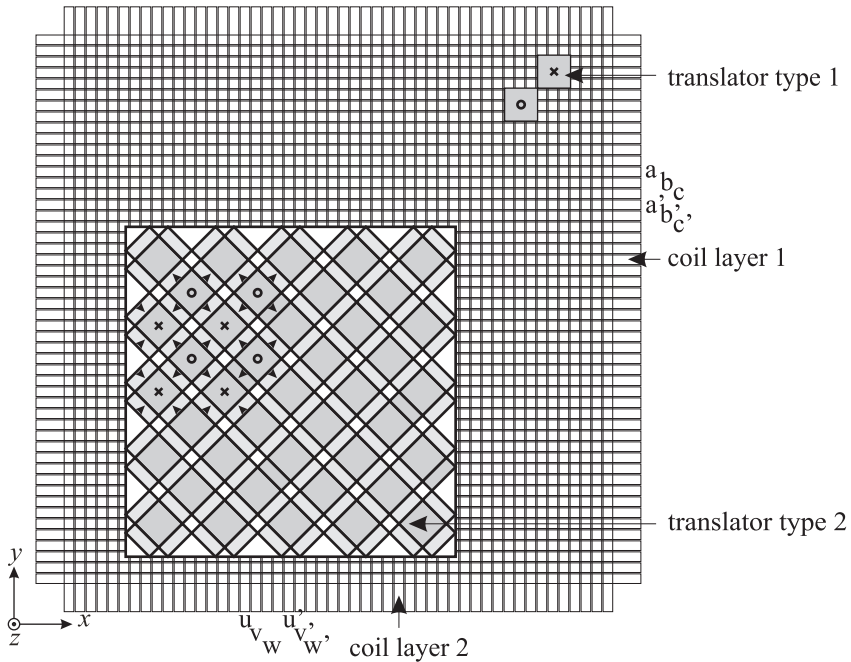
Figure 2.7. *Moving-magnet planar actuator with two layers of stator coils and two types of translators with different magnet arrays.*

magnet array are higher for the production of the same force. Furthermore, power is dissipated in the whole coil, while only a small part of the coil contributes to the levitation and propulsion of the translator. Consequently, when the stroke of the actuator is enlarged, the resistance and power dissipation will increase.

2.4 Magnetically levitated planar with short coils

The disadvantage of the moving-magnet planar actuator with multiple orthogonal layers of long coils can be overcome by decreasing the size of the coils to less than the size of the translator. As a result, only one layer of coils is needed. However, to obtain long-stroke motion, the set of active coils has to be switched. The stroke of these actuators only depends on the size of the stator, which can, in principle, be

(a)

(b)
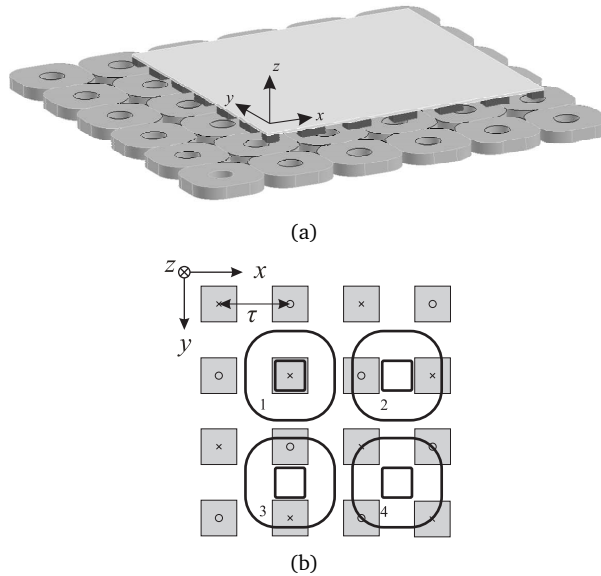
Figure 2.8. *Two-dimensional electric motor [28]: a) Overview, b) coil group.*

made infinitely long by adding extra stator coils. Moreover, multiple translators can be controlled above the same stator.

2.4.1   Two-dimensional electric motor

A planar actuator with moving magnets and small stationary coils for lithography applications is described in [28]. The motor is shown in Figure 2.8a. The translator consists of an NS-magnet array, which has an alternating magnetization of the magnets in both the x- and y-directions. The stator contains square coils with concentrated windings. Sixteen square coils are used simultaneously to levitate and to move the translator. The sixteen coils can be subdivided into four groups of four coils. Such a group is shown in Figure 2.8b. The coils in the group are displaced $\frac{3}{2}\tau$, where τ is the pole pitch. The basic idea of this actuator is that these four coils can exert a force vector in the xyz-plane on the translator, independent of the position of the translator with respect to the coils (see also section 4.1). Four of these groups

are combined to control all six degrees-of-freedom of the planar actuator.

Because this motor is only described in the patent literature, there is no information about its performance. Only the performance of a controller for a planar actuator without active magnetic bearing has been experimentally verified and is discussed in [68]. A planar actuator with this coil configuration is one of the investigated topologies in this thesis. The working principle, the commutation and performance of are treated in the sections 3.8, 4.1, 4.3 and 5.4.

In [4], also an embodiment of this actuator is presented with four layers of short rectangular coils in the z-direction.

2.4.2 Inverted planar motor

One of the disadvantages of a moving-coil planar actuator is the cable-slab attached to the translator which causes disturbances. After the development of the moving-coil planar actuator (section 2.2.2), the inventors inverted this actuator and realized a moving-magnet planar motor with infinite stroke capabilities [15]. This actuator is shown in Figure 2.9. Also in this case, the coils are rotated 45 degrees with respect to the permanent magnets. Nine three-phase systems with concentrated windings can be recognized. However, all 27 coils are individually connected to single-phase current amplifiers in order to control the force and torque exerted on the translator accurately and allow for long-stroke motion, as will be further explained in section 4.2.

Figure 2.10 shows a photo of the demonstrator. The levitated permanent magnet array floats freely above the coils. The position is measured with Hall-sensors located in the stator, which provide a measurement accuracy of 0.3 mm. However, when the position is measured with a laser interferometer system, a position error of 10 to 100 nm is expected [58]. The stator coils of the demonstrator are packaged in a ceramic material to quickly remove the heat produced by the coils.

This moving-magnet planar actuator configuration has been developed in parallel and independently of the moving-magnet planar actuator concept discussed in this thesis.

2.5 Conclusions

Magnetically levitated planar actuators are an emerging field of study. Three types of magnetically levitated planar actuators with moving-magnets have been distinguished. Planar actuator constructed of multi-DOF actuator segments, planar actuator with multiple orthogonal layers of long coils and planar actuators with short
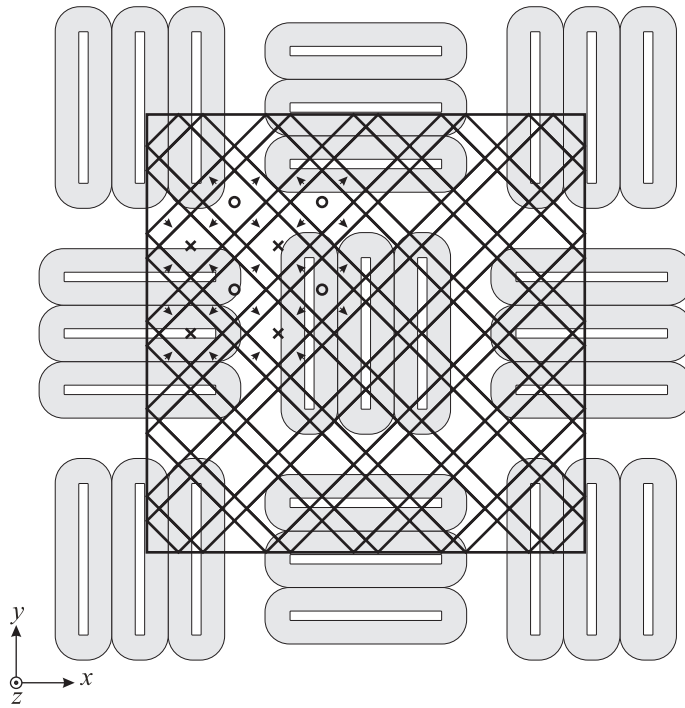
Figure 2.9. *Inverted planar actuator [15].*
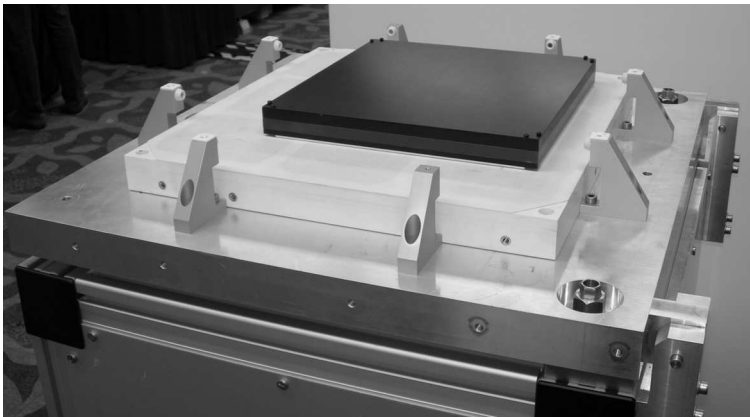
Figure 2.10. *Photo of the demonstrator of the inverted planar actuator (2006 ASPE annual meeting, Monterey, CA).*

coils of which the set of active coils is switched during motion in the xy-plane. The last type is investigated in this thesis as these actuators provide infinitely long-stroke capabilities and multiple translators can be controlled above one stator. The feasibility of this concept has only been demonstrated by the inverted planar actuator (section 2.4.2) and the actuator discussed in this thesis.

Chapter 3

Electromechanical models

The calculation of the magnetic flux density distribution is a crucial step in the analysis and design of electromechanical devices. To determine the torque or force waveforms in a electrical machine, accurate predictions of the magnetic flux density distribution in the airgap between the stator and the rotor are required. These magnetic flux density distributions are usually calculated by using the finite element method (FEM), which is a reliable and flexible method that can deal with regions with non-linear materials and complex shapes. To reduce the computational effort, the three-dimensional problem is often approximated by a two- or one-dimensional problem and by the application of periodical or symmetrical boundary conditions. An other method is to model the device with magnetic equivalent circuits (MEC), in which the flux paths, coils and magnets are modeled by reluctances, magnetomotive force (MMF) sources and flux sources, respectively.

The application of both methods to magnetically levitated planar actuators is not practical for several reasons. Firstly, planar actuator have a truly three-dimensional magnetic flux density distribution, which cannot be simplified to a two-dimensional one. Hence, time-consuming three-dimensional analyses are required. Secondly, the problem size cannot be reduced by the application of periodical or symmetrical boundary conditions because of the finite length of the device and the six degrees-of-freedom of the translator. Lastly, due to the absence of iron, there are no clearly defined flux paths, which can be modeled with reluctances. Moreover, the flux is also not confined within the device. Therefore, Dirichlet boundary conditions, which confine the magnetic flux density in a certain region, should be placed as far as possible from the planar actuator.

In this chapter, a magnetostatic analysis framework for moving-magnet planar actuators is presented. The framework provides three alternative methods to calculate both the force and torque acting in moving-magnet planar actuators. These methods are based on analytical solutions of the magnetic flux density distribution of the permanent magnets and numerical or analytical solutions of the Lorentz force law. Contrary to finite element methods, these models are capable of simulating large planar actuators fast. The first model is based on magnetic surface charges. This numerical model allows to position the translator, which contains the permanent magnets, in six degrees-of-freedom with respect to the coil array. The magnetization of the permanent magnets is modeled by Fourier series in the second model. By this, an expression of the magnetic flux density distribution of the permanent magnets is derived. The Lorentz force and torque integrals are solved semi-analytically and, consequently, the calculation time is short. The third method is a fully analytical method and can be evaluated in real-time. This model is used in the decoupling algorithm of planar actuators. The chapter concludes with an extension of the magnetostatic models to a quasi-static model to solve the voltage equation of the coils. The magnetostatic analysis framework have been published in [41, 34, 36, 33].

3.1   Maxwell's equations

The Maxwell's equations govern the electromagnetic phenomena [27, 62]

$$\nabla \cdot \vec{D} = \rho_c, \tag{3.1}$$

$$\nabla \cdot \vec{B} = 0, \tag{3.2}$$

$$\nabla \times \vec{E} = -\frac{\partial \vec{B}}{\partial t}, \tag{3.3}$$

$$\nabla \times \vec{H} = \vec{J} + \frac{\partial \vec{D}}{\partial t}, \tag{3.4}$$

where $\vec{D}$ is the electrical flux density, ρ_c is the charge density, $\vec{B}$ is the magnetic flux density, $\vec{E}$ is the electrical field strength, $\vec{H}$ is the magnetic field strength, $\vec{J}$ is the current density and t is the time. Material properties are described by

$$\vec{B} = \mu_0(\vec{H} + \vec{M}), \tag{3.5}$$

$$\vec{D} = \epsilon_0 \vec{E} + \vec{P}, \tag{3.6}$$

$$\vec{J} = \sigma \vec{E}, \tag{3.7}$$

where μ_0 and ϵ_0 are the permeability and the permittivity of free space, respectively, $\vec{M}$ is the magnetization, $\vec{P}$ is the polarization and σ is the electrical conductivity.

The forces and torques in the planar actuator are determined with a static analysis. In that case, the Maxwell's equations are decoupled. For magnetostatic problems the Maxwell's equations reduce to

$$\nabla \cdot \vec{B} = 0, \tag{3.8}$$

$$\nabla \times \vec{H} = \vec{J}. \tag{3.9}$$

The solution of these equations can be simplified by the introduction of a magnetic vector potential $\vec{A}$

$$\vec{B} = \nabla \times \vec{A}, \tag{3.10}$$

and imposing $\nabla \cdot \vec{A} = 0$, or by the introduction of a magnetic scalar potential Ψ in current-free regions ($\vec{J} = \vec{0}$)

$$\vec{H} = -\nabla \Psi. \tag{3.11}$$

The electromagnetic force F_x in a system along the x-direction is given by [46]

$$F_x = \frac{\partial \Lambda}{\partial x} i - \frac{\mathrm{d} W_{m0}}{\mathrm{d} x} - \frac{W_{mi}}{\partial x}, \tag{3.12}$$

where Λ is the flux of the permanent magnets linked by the coil, i is the current in the coil, W_{m0} is the magnetic field energy due to the permanent magnets and W_{mi} is the magnetic field energy due to the currents in the coils. The three terms at the right side of (3.12) have different origins:

- The first term is the desired electromagnetic force in the planar actuator. This force originates from the interaction of the magnetic fields of both the stator coils and the permanent magnets.
- The second term is the cogging force. The cogging force is caused by the interaction of the permanent magnets on the translator with the teeth structure of the stator geometry. Since the planar actuator is magnetically levitated, the stator is ironless because the attraction force between the translator with permanent magnets and the iron in stator would compromise the magnetic bearing. Therefore, this force is not present in the planar actuator.
- The third term is the reluctance force. The reluctance force is caused by the change of the inductance of the coreless stator coils due to materials in the translator with a magnetic permeability $\mu_r \neq 1$. Finite element predictions of the reluctance force in the planar actuator designs discussed in section 5.4 (with a current density of $J = 30\,\mathrm{A/mm}^2$ in the coils), show that compared to the desired force, the reluctance force due to the permanent

magnets (with $\mu_r \approx 1.03 - 1.05$) is small ($< 0.3\%$) and can be considered
as a disturbance force. Not considering a (quasi-) Halbach magnetization,
back-iron behind the magnets can be implemented to increase the magnetic
flux density and, hence, the force. The reluctance force due to back-iron is
an order of magnitude larger than the reluctance force due to the mag-
nets ($< 3\%$, for the designs discussed in section 5.4). The use of back-iron
should be carefully considered due to the increased translator mass (see
also section 5.2).

There are several techniques for the calculation of the electromagnetic force.
The Maxwell stress tensor and the virtual work method are two macroscopic meth-
ods. Because the coils in the planar actuator are coreless, the force acts on the
current carrying conductors itself and, consequently, it can be calculated with the
Lorentz force law

$$\vec{F} = Q(\vec{E} + \vec{v} \times \vec{B}), \tag{3.13}$$

where Q is the electric charge, and $\vec{v}$ the velocity of the charge. The advantage of
this method over the virtual work method and the Maxwell stress tensor is that only
the magnetic flux density distribution of the permanent magnets has to be calcu-
lated and not also the magnetic flux density distribution due to the coil currents.

3.2   Force and torque production

The moving-magnet planar actuators, which can be analyzed with the methods pre-
sented in this chapter, are constructed of a permanent-magnet array with cuboidal
magnets and coils with concentrated windings. Although the use of iron behind
the permanent magnets is not desired, back-iron can be included in the models by
the method of imaging [6] or by changing the boundary conditions. The force on
the current carrying conductor is calculated with the Lorentz force law (for mag-
netostatic problems $\vec{E} = \vec{0}$). The force on the magnets opposes the force on the
coils

$$\vec{F} = - \int_{V_{coil}} \vec{J} \times \vec{B} \mathrm{d}V. \tag{3.14}$$

It follows that the torque, $\vec{T} = \vec{r} \times \vec{F}$, on the permanent magnets is given by

$$\vec{T} = - \int_{V_{coil}} \vec{r} \times (\vec{J} \times \vec{B}) \mathrm{d}V, \tag{3.15}$$

where $\vec{r}$ is the vector from the point about which the torque is calculated. Because
the permanent magnets are located at the moving part of the actuator, $\vec{r}$ varies with

(a)

(b)
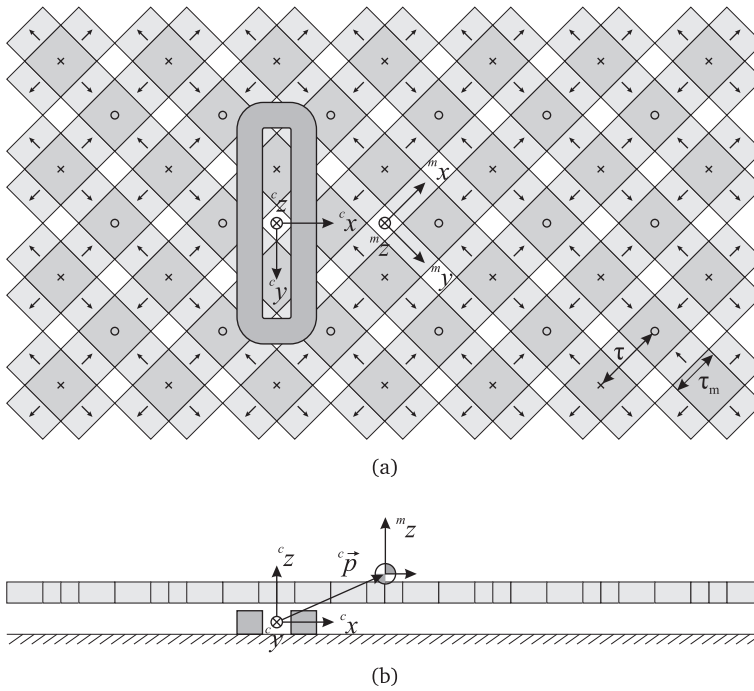
Figure 3.1. *Halbach magnet array and a single coil: a) Bottom view, b) cross section.*

the position of the translator. On the contrary, $\vec{r}$ in a moving-coil planar actuator is independent of the position of the translator, as the coils are located on the moving part of the actuator itself.

   Linear material properties and rigid body dynamics are assumed. As a result, the superposition principle can be applied to the magnetic flux density, force and torque calculations. All the models are derived for a rectangular coil and a two-dimensional Halbach magnet array.

3.3   Coordinate system definitions

Two coordinate systems are defined in the 3-D Euclidian space to model the actuator. Fig 3.1 shows a partial planar actuator, i.e. a Halbach permanent-magnet array

and a single coil. A global coordinate system is located at the stationary part of the actuator. In this coordinate system the stator coils are defined. For that reason it is denoted with the superscript c

$$^c\vec{x} = \left[\begin{array}{ccc} ^cx & ^cy & ^cz \end{array}\right]^{\mathsf{T}}. \tag{3.16}$$

A local coordinate system is fixed to the mass center point of the translator. In this coordinate system the magnets are defined. This coordinate frame is denoted with the superscript m

$$^m\vec{x} = \left[\begin{array}{ccc} ^mx & ^my & ^mz \end{array}\right]^{\mathsf{T}}. \tag{3.17}$$

The vector

$$^c\vec{p} = \left[\begin{array}{ccc} ^cp_x & ^cp_y & ^cp_z \end{array}\right]^{\mathsf{T}}, \tag{3.18}$$

is the position of the local coordinate system, i.e. the mass center point of the translator, in the global coordinate system.

Coordinates are transformed from one system to the other with an orientation transformation and afterwards a translation. The transformation matrix $^c\mathbf{T_m}$ for a position from the local to the global coordinate system is equal to [52]

$$^c\mathbf{T_m} = \left[\begin{array}{cc} ^c\mathbf{R_m} & ^c\vec{p} \\ 0 & 1 \end{array}\right]. \tag{3.19}$$

For convenience, the orientation transformation matrix is defined as

$$^c\mathbf{R_m} = \mathbf{Rot}(^cy, \theta)\mathbf{Rot}(^cx, \psi)\mathbf{Rot}(^cz, \phi), \tag{3.20}$$

where

$$\mathbf{Rot}(^cy, \theta) = \left[\begin{array}{ccc} \cos(\theta) & 0 & \sin(\theta) \\ 0 & 1 & 0 \\ -\sin(\theta) & 0 & \cos(\theta) \end{array}\right], \tag{3.21}$$

$$\mathbf{Rot}(^cx, \psi) = \left[\begin{array}{ccc} 1 & 0 & 0 \\ 0 & \cos(\psi) & -\sin(\psi) \\ 0 & \sin(\psi) & \cos(\psi) \end{array}\right], \tag{3.22}$$

$$\mathbf{Rot}(^cz, \phi) = \left[\begin{array}{ccc} \cos(\phi) & -\sin(\phi) & 0 \\ \sin(\phi) & \cos(\phi) & 0 \\ 0 & 0 & 1 \end{array}\right], \tag{3.23}$$

and where ψ, θ and ϕ are the rotation angles about the ^cx- ^cy-, and ^cz-axes, respectively. Thus, the position and orientation of the translator can be described in six

degrees-of-freedom. The transformation matrix $\mathbf{^mT_c}$ for a position from the global to the local coordinate system is equal to

$$\begin{aligned}\mathbf{^mT_c} \;=\; \mathbf{^cT_m}^{-1} \;&=\; \left[\begin{array}{cc} \mathbf{^cR_m}^\mathsf{T} & -\mathbf{^cR_m}^\mathsf{T}{}^c\vec{p} \\ 0 & 1 \end{array}\right] \\ &=\; \left[\begin{array}{cc} \mathbf{^mR_c} & -\mathbf{^mR_c}{}^c\vec{p} \\ 0 & 1 \end{array}\right], \end{aligned} \tag{3.24}$$

because $\mathbf{^mT_c}$ is orthonormal.

Applying the appropriate transformation matrix, a position is transferred between the coordinate systems, according to

$$\left[\begin{array}{c} ^m\vec{x} \\ 1 \end{array}\right] = \mathbf{^mT_c}\left[\begin{array}{c} ^c\vec{x} \\ 1 \end{array}\right], \tag{3.25}$$

$$^m\vec{x} = \mathbf{^mR_c}\left(^c\vec{x} - {}^c\vec{p}\right), \tag{3.26}$$

and a free vector as defined in [52], e.g. the current density $\vec{J}$, according to

$$\left[\begin{array}{c} ^m\vec{J} \\ 0 \end{array}\right] = \mathbf{^mT_c}\left[\begin{array}{c} ^c\vec{J} \\ 0 \end{array}\right], \tag{3.27}$$

$$^m\vec{J} = \mathbf{^mR_c}\,^c\vec{J}. \tag{3.28}$$

3.4   Magnetic surface charge model

In a moving-magnet planar actuator, a part of the coils will be near the edge of the magnet array. To investigate the influence of the finite length of the magnet array, a model is derived in which all the permanent magnets are modeled individually. A similar type of model has been used in the design of moving-coil planar actuators [13].

3.4.1   Magnetic flux density distribution

The permanent magnets in the planar actuator are assumed to be cuboidal. The magnetic field of such a cuboidal magnet in three dimensions can be derived from Maxwell's equations, using the scalar magnetic potential. This results in a model of the permanent magnet with two surface charges [22]. The surface charges are on the sides of the permanent magnet, which are perpendicular to the magnetization direction. The surface charges $\pm\rho_s$ are equal to $\pm B_r$, the remanent magnetization
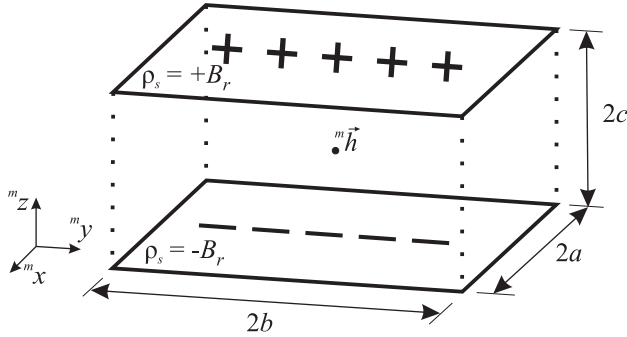
Figure 3.2. *Charge model of a cuboidal magnet magnetized in the positive $^m z$-direction.*

of the permanent magnet. The only assumption made is that the relative permeability $\mu_r = 1$ in and outside the permanent magnet. The error due to this assumption is small because high quality sintered NdFeB permanent magnets have a low relative permeability ($\mu_r \approx 1.03 - 1.05$). Figure 3.2 shows the model of a magnet, magnetized in the positive $^m z$-direction. The sizes of the magnet are $2a$, $2b$, and $2c$ in the $^m x$-, $^m y$-, and $^m z$-direction, respectively. The center of the magnet is located at

$$^m \vec{h} = \begin{bmatrix} ^m h_x & ^m h_y & ^m h_z \end{bmatrix}^\mathsf{T}. \tag{3.29}$$

The magnetic flux density in the local coordinate system

$$^m \vec{B} = \begin{bmatrix} ^m B_x & ^m B_y & ^m B_z \end{bmatrix}^\mathsf{T}, \tag{3.30}$$

of a cuboidal magnet magnetized in the positive $^m z$-direction is equal to [78]

$$^m B_x = \frac{B_r}{4\pi} \sum_{i=0}^{1} \sum_{j=0}^{1} \sum_{k=0}^{1} (-1)^{i+j+k} \log\left(R - T\right), \tag{3.31}$$

$$^m B_y = \frac{B_r}{4\pi} \sum_{i=0}^{1} \sum_{j=0}^{1} \sum_{k=0}^{1} (-1)^{i+j+k} \log\left(R - S\right), \tag{3.32}$$

$$^m B_z = \frac{B_r}{4\pi} \sum_{i=0}^{1} \sum_{j=0}^{1} \sum_{k=0}^{1} (-1)^{i+j+k} \mathrm{atan2}\left(\frac{ST}{RU}\right), \tag{3.33}$$

where atan2 is a four-quadrant arctangent function and

$$R = \sqrt{S^2 + T^2 + U^2},$$ (3.34)

$$S = ({}^{m}x - {}^{m}h_x) - (-1)^i a,$$ (3.35)

$$T = ({}^{m}y - {}^{m}h_y) - (-1)^j b,$$ (3.36)

$$U = ({}^{m}z - {}^{m}h_z) - (-1)^k c.$$ (3.37)

The magnetic field of an array of permanent magnets is equal to the sum of the contributions of the individual magnets.

3.4.2 Force and torque

The force and torque are calculated with the Lorentz force principle. The translator can be positioned in six degrees-of-freedom with respect to the stator coils by using the coordinate transformations. The force on the translator array in the local coordinate system is equal to

$$ {}^{m}\vec{F} = - \int_{V_{coil}} \left(\mathbf{{}^{m}R_{c}} {}^{c}\vec{J}({}^{c}\vec{x}) \right) \times {}^{m}\vec{B} \left(\mathbf{{}^{m}R_{c}} ({}^{c}\vec{x} - {}^{c}\vec{p}) \right) \mathrm{d}^{c}V. $$ (3.38)

The torque in the local coordinate system is equal to

$$ {}^{m}\vec{T} = - \int_{V_{coil}} \left(\mathbf{{}^{m}R_{c}} ({}^{c}\vec{x} - {}^{c}\vec{p}) \right) $$

$$ \times \left(\left(\mathbf{{}^{m}R_{c}} {}^{c}\vec{J}({}^{c}\vec{x}) \right) \times {}^{m}\vec{B} \left(\mathbf{{}^{m}R_{c}} ({}^{c}\vec{x} - {}^{c}\vec{p}) \right) \right) \mathrm{d}^{c}V. $$ (3.39)

The volume integrals are solved numerically using a cuboidal mesh as shown in Figure 3.3a. In every mesh element the integral is solved with the three-dimensional trapezoidal rule [1].

3.5 Harmonic model

The magnetic surface charge model takes into account all the individual magnets in the magnet array of the planar actuator. Because the calculation time of this model is proportional to both the amount of permanent magnets and the amount

(a)   (b)
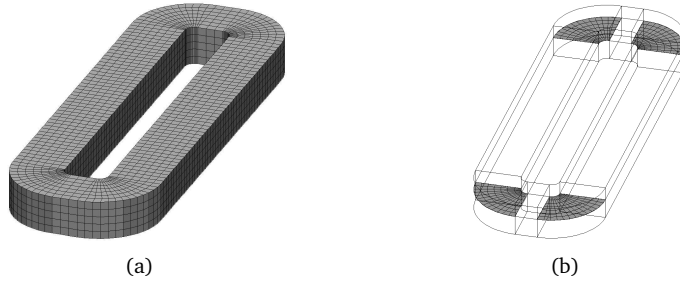
Figure 3.3. *Coil mesh: a) Magnetic surface charge model, b) harmonic model.*

of coils, the analysis of full planar actuators with many coils and magnets is time-consuming. For the optimization of the dimensions of the coils and permanent magnets, the development of commutation algorithms and the comparison of a large numbers of topologies, a reduction of the calculation time is desired because the force and torque have to be calculated for many positions of the translator. The calculation time can be reduced by modeling the permanent magnets as an infinitely large magnet array with Fourier series and by removing the rotational degrees-of-freedom from the model. Hence, the end-effects of the magnet array are neglected.

Fourier series are extensively used in the analysis of electrical machines. In the field of planar actuators, Fourier analysis has been applied to the force calculation in both a short-stroke moving-magnet planar actuator [69] (two-dimensional analysis) and a moving-coil planar xy-motor [10, 9] (three-dimensional analysis). In this section, both a force and a torque calculation method based on Fourier series are derived, which only require numerical integration of the Lorentz force integral in the corner segments of the coils.

3.5.1   Magnetic flux density distribution

The magnetic flux density distribution of the permanent magnets on the translator is calculated in the local coordinate system. The three-dimensional space is divided into three regions of which a cross section is shown in Figure 3.4. Regions 1 and 3 are in air. The permanent magnets in region 2 are located in between $m_b \leq {}^m z \leq m_t$. For region 2, the permeability $\mu = \mu_0 \mu_r$, where μ_r is the relative permeability of the permanent magnets. The magnetic flux distribution is derived
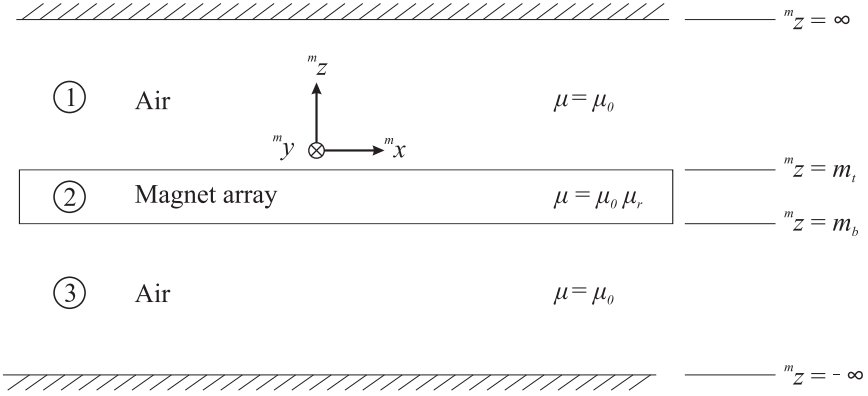
Figure 3.4. *3-D space with magnet array divided into three regions.*

for the magnet array which is shown in Figure 3.1. The air in the permanent-magnet array is modeled as non-magnetized permanent magnet material with $\mu_r > 1$. Because high quality sintered NdFeB permanent magnets will be used in the planar actuator ($\mu_r = 1.03 - 1.05$), the error due to this assumption is neglected.

Table 3.1 contains the field equations in the three regions. A magnetic scalar potential $^m\Psi$ is introduced in all three charge-free regions to solve the problem. The magnetic scalar potential in the air (regions 1 and 3 in Figure 3.4) is governed by the Laplace's equation and in the permanent magnets by the Poisson's equation [80].

In region 2, which contains the permanent magnets,

$$^m\vec{B}_2 = \mu_0(^m\vec{H}_2 + {}^m\vec{M}) = \mu_0\mu_r \,^m\vec{H}_2 + \mu_0 \,^m\vec{M}_0, \tag{3.40}$$

where $^m\vec{M}_0$ is the residual magnetization vector [80]. The residual magnetization vector of an infinitely large Halbach magnet array with the permanent magnets distributed as shown in Figure 3.1 is given by

$$^m\vec{M}_0 = \frac{B_r}{\mu_0} \sum_{k=1}^{\infty} \sum_{l=1}^{\infty} \begin{bmatrix} -a_k b_l \cos\left(\frac{k\pi\,^mx}{\tau}\right) \sin\left(\frac{l\pi\,^my}{\tau}\right) \\ -b_k a_l \sin\left(\frac{k\pi\,^mx}{\tau}\right) \cos\left(\frac{l\pi\,^my}{\tau}\right) \\ b_k b_l \sin\left(\frac{k\pi\,^mx}{\tau}\right) \sin\left(\frac{l\pi\,^my}{\tau}\right) \end{bmatrix}, \tag{3.41}$$

where k and l are the harmonic numbers for the ^mx- and ^my-direction, respectively,

Table 3.1. *Magnetic field equations*

Region 1	Region 2	Region 3
$\nabla \times {}^{m}\vec{H}_1 = \vec{0}$	$\nabla \times {}^{m}\vec{H}_2 = \vec{0}$	$\nabla \times {}^{m}\vec{H}_3 = \vec{0}$
$\nabla \cdot {}^{m}\vec{B}_1 = 0$	$\nabla \cdot {}^{m}\vec{B}_2 = 0$	$\nabla \cdot {}^{m}\vec{B}_3 = 0$
${}^{m}\vec{B}_1 = \mu_0 \, {}^{m}\vec{H}_1$	${}^{m}\vec{B}_2 = \mu_0 ({}^{m}\vec{H}_2 + {}^{m}\vec{M})$	${}^{m}\vec{B}_3 = \mu_0 \, {}^{m}\vec{H}_3$
${}^{m}\vec{H}_1 = -\nabla \, {}^{m}\Psi_1$	${}^{m}\vec{H}_2 = -\nabla \, {}^{m}\Psi_2$	${}^{m}\vec{H}_3 = -\nabla \, {}^{m}\Psi_3$
$\nabla^2 \, {}^{m}\Psi_1 = 0$	$\nabla^2 \, {}^{m}\Psi_2 = \nabla \cdot {}^{m}\vec{M}$	$\nabla^2 \, {}^{m}\Psi_3 = 0$

and

$$a_k = \frac{4}{k\pi} \cos\left(\frac{k\tau_m\pi}{2\tau}\right) \sin\left(\frac{k\pi}{2}\right), \tag{3.42}$$

$$a_l = \frac{4}{l\pi} \cos\left(\frac{l\tau_m\pi}{2\tau}\right) \sin\left(\frac{l\pi}{2}\right), \tag{3.43}$$

$$b_k = \frac{4}{k\pi} \sin\left(\frac{k\tau_m\pi}{2\tau}\right) \sin\left(\frac{k\pi}{2}\right), \tag{3.44}$$

$$b_l = \frac{4}{l\pi} \sin\left(\frac{l\tau_m\pi}{2\tau}\right) \sin\left(\frac{l\pi}{2}\right), \tag{3.45}$$

where τ is the pole pitch and τ_m is the length of the side of the magnets which are magnetized in the ${}^{m}z$-direction (as defined in Figure 3.1). It is assumed that remanent magnetization B_r of the magnets magnetized in the ${}^{m}x$- and ${}^{m}y$-directions and of the magnets magnetized in the ${}^{m}z$-direction is the same.

The differential equations in the three regions are solved by the separation of variables method. The solution of the scalar potential is a product of functions which involve only one variable. In the magnets

$$\nabla^2 \, {}^{m}\Psi_2 = \nabla \cdot \frac{{}^{m}\vec{M}_0}{\mu_r} = \frac{B_r}{\mu_0\mu_r} \sum_{k=1}^{\infty} \sum_{l=1}^{\infty} \left(\frac{a_k b_l k\pi + b_k a_l l\pi}{\tau} \right)$$
$$\cdot \sin\left(\frac{k\pi \, {}^{m}x}{\tau}\right) \sin\left(\frac{l\pi \, {}^{m}y}{\tau}\right). \tag{3.46}$$

Hence, a solution for the scalar potential of the form

$$^m\Psi = \sum_{k=1}^{\infty}\sum_{l=1}^{\infty} Z(\,^m z)\sin\left(\frac{k\pi\,^m x}{\tau}\right)\sin\left(\frac{l\pi\,^m y}{\tau}\right), \tag{3.47}$$

is assumed. In regions 1 and 3 substitution of (3.47) in the Laplace's equation, $\nabla^2\,^m\Psi = 0$, results in

$$-\sin\left(\frac{k\pi\,^m x}{\tau}\right)\sin\left(\frac{l\pi\,^m y}{\tau}\right)\cdot\left(\frac{\mathrm{d}^2 Z(\,^m z)}{\mathrm{d}\,^m z^2} - \lambda^2 Z(\,^m z)\right) = 0, \tag{3.48}$$

where

$$\lambda = \sqrt{\left(\frac{k\pi}{\tau}\right)^2 + \left(\frac{l\pi}{\tau}\right)^2}. \tag{3.49}$$

The general solution of this equation is equal to

$$Z(\,^m z) = K_1 e^{-\lambda\,^m z} + K_3 e^{\lambda\,^m z}, \tag{3.50}$$

where K_1 and K_3 are constants. Because of the Dirichlet boundary conditions (zero scalar potential at $z = \pm\infty$)

$$^m\Psi_1 = \sum_{k=1}^{\infty}\sum_{l=1}^{\infty} K_1 e^{-\lambda\,^m z}\sin\left(\frac{k\pi\,^m x}{\tau}\right)\sin\left(\frac{l\pi\,^m y}{\tau}\right), \tag{3.51}$$

and

$$^m\Psi_3 = \sum_{k=1}^{\infty}\sum_{l=1}^{\infty} K_3 e^{\lambda\,^m z}\sin\left(\frac{k\pi\,^m x}{\tau}\right)\sin\left(\frac{l\pi\,^m y}{\tau}\right). \tag{3.52}$$

In region 2 a non-homogeneous differential equation is obtained

$$-\sin\left(\frac{n\pi\,^m x}{\tau}\right)\sin\left(\frac{m\pi\,^m y}{\tau}\right)\left(\frac{\mathrm{d}^2 Z(\,^m z)}{\mathrm{d}\,^m z^2} - \lambda^2 Z(\,^m z)\right)$$
$$= \frac{B_r}{\mu_0\mu_r}\left(\frac{a_k b_l k\pi}{\tau} + \frac{b_k a_l l\pi}{\tau}\right)\sin\left(\frac{k\pi\,^m x}{\tau}\right)\sin\left(\frac{l\pi\,^m y}{\tau}\right). \tag{3.53}$$

The solution equals

$$Z(\,^m z) = K_{21} e^{-\lambda\,^m z} + K_{22} e^{\lambda\,^m z} - \frac{B_r a_l b_k l\tau + B_r a_k b_l k\tau}{\mu_0\mu_r\pi(k^2 + l^2)}, \tag{3.54}$$

Table 3.2. *Boundary conditions*

$^m z = \infty$	$^m z = m_t$	$^m z = m_b$	$^m z = -\infty$
$^m\Psi_1 = 0$	$^m H_{1,x} = {}^m H_{2,x}$ $^m H_{1,y} = {}^m H_{2,y}$ $^m B_{1,z} = {}^m B_{2,z}$	$^m H_{2,x} = {}^m H_{3,x}$ $^m H_{2,y} = {}^m H_{3,y}$ $^m B_{2,z} = {}^m B_{3,z}$	$^m\Psi_3 = 0$

where K_{21} and K_{22} are constants. The constants K_1, K_{21}, K_{22} and K_3 are calculated with the boundary conditions which are listed in Table 3.2. The expression for the magnetic flux density distribution in the area of interest, region 3, is given by

$$
{}^m\vec{B}_3({}^m\vec{x}) = -\mu_0 \sum_{k=1}^{\infty} \sum_{l=1}^{\infty} K_3 e^{\lambda\, {}^m z}
\begin{bmatrix}
\dfrac{k\pi}{\tau} \cos\left(\dfrac{k\pi\, {}^m x}{\tau}\right) \sin\left(\dfrac{l\pi\, {}^m y}{\tau}\right) \\[2mm]
\dfrac{l\pi}{\tau} \sin\left(\dfrac{k\pi\, {}^m x}{\tau}\right) \cos\left(\dfrac{l\pi\, {}^m y}{\tau}\right) \\[2mm]
\lambda \sin\left(\dfrac{k\pi\, {}^m x}{\tau}\right) \sin\left(\dfrac{l\pi\, {}^m y}{\tau}\right)
\end{bmatrix},
\quad (3.55)
$$

where

$$
K_3(\mu_r = 1) = B_r \left(e^{-m_t\lambda} - e^{-m_b\lambda}\right) \frac{\left(b_k b_l \pi \left(k^2 + l^2\right) + a_k b_l k\lambda\tau + a_l b_k l\lambda\tau\right)}{2\left(k^2 + l^2\right)\pi\lambda\mu_0}. \quad (3.56)
$$

3.5.2   Force and torque

The obtained magnetic flux density distribution (3.55) can be substituted in (3.38) and (3.39). Because the calculation time of the magnetic flux density distribution of the permanent magnets is not proportional anymore to the number of permanent magnets on the translator, the calculation time of the force and the torque are reduced. A further reduction can be obtained when the rotational degrees-of-freedom are removed from the model i.e. $\psi = 0$ rad, $\theta = 0$ rad and $\phi = 0$ rad or $\phi = \pm\frac{\pi}{4}$ rad.

For convenience (3.55) is rewritten to

$$
{}^m\vec{B}_3({}^m\vec{x}) = \sum_{k=1}^{\infty}\sum_{l=1}^{\infty} e^{(\lambda\,{}^m z)}\,{}^m\vec{B}_{3xy}({}^m\vec{x}, k, l), \tag{3.57}
$$

where

$$
{}^m\vec{B}_{3xy}({}^m\vec{x}, k, l) = -\mu_0 K_3
\begin{bmatrix}
\frac{k\pi}{\tau}\cos\left(\frac{k\pi\,{}^m x}{\tau}\right)\sin\left(\frac{l\pi\,{}^m y}{\tau}\right) \\[2mm]
\frac{l\pi}{\tau}\sin\left(\frac{k\pi\,{}^m x}{\tau}\right)\cos\left(\frac{l\pi\lambda\,{}^m y}{\tau}\right) \\[2mm]
\lambda\sin\left(\frac{k\pi\,{}^m x}{\tau}\right)\sin\left(\frac{l\pi\,{}^m y}{\tau}\right)
\end{bmatrix}. \tag{3.58}
$$

The Lorentz force volume integral is split into an integral over ${}^c z$ and a surface integral over ${}^c x$ and ${}^c y$

$$
{}^c\vec{F} = -\sum_{k=1}^{\infty}\sum_{l=1}^{\infty}\int_{V_{coil}} {}^c\vec{J}\times{}^{\mathbf{c}}\mathbf{R_m}\,{}^m\vec{B}_3\left({}^{\mathbf{m}}\mathbf{R_c}\left({}^c\vec{x}-{}^c\vec{p}\right)\right)\mathrm{d}^c V
$$

$$
= -\sum_{k=1}^{\infty}\sum_{l=1}^{\infty}\int_{c_b}^{c_t} e^{\lambda({}^c z-{}^c p_z)}\mathrm{d}^c z\cdot\iint_{S_{coil}} {}^c\vec{J}\times{}^{\mathbf{c}}\mathbf{R_m}\,{}^m\vec{B}_{3xy}\left({}^{\mathbf{m}}\mathbf{R_c}\left({}^c\vec{x}-{}^c\vec{p}\right), k, l\right)\mathrm{d}^c x\mathrm{d}^c y. \tag{3.59}
$$

The integral over ${}^c z$ is solved analytically. The surface integral over ${}^c x$ and ${}^c y$ are also solved analytically in the straight segments of the coil. In the corner segments, the surface integral is solved numerically using quadrilateral mesh elements as shown in Figure 3.3b. In every mesh element the integral is solved with the two-dimensional trapezoidal rule.

The same approach is applied to the torque. The distribution of the force in the volume of the coil has to be taken into account when the torque is calculated. To separate the integrals over ${}^c z$ and over ${}^c x$ and ${}^c y$, an effective torque arm in the ${}^c z$-direction ${}^c r_z$ is introduced

$$
\int_{c_b}^{c_t} ({}^c z-{}^c p_z)e^{\lambda({}^c z-{}^c p_z)}\mathrm{d}\,{}^c z = {}^c r_z\int_{c_b}^{c_t} e^{\lambda({}^c z-{}^c p_z)}\mathrm{d}\,{}^c z. \tag{3.60}
$$

The effective arm is given by

$$
{}^c r_z = c_t - {}^c p_z - \frac{1}{\lambda} - \frac{(c_b-c_t)e^{\lambda c_b}}{e^{\lambda c_b}-e^{\lambda c_t}}, \tag{3.61}
$$
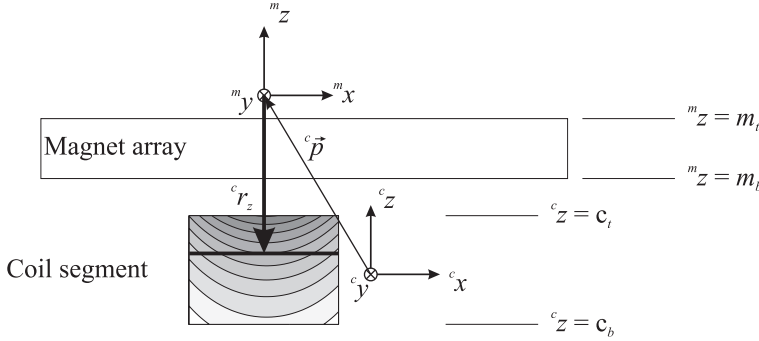
Figure 3.5. *Effective force arm in the ^cz-direction.*

and is dependent on the harmonic numbers k and l. The effective torque arm is illustrated in Figure 3.5. In the cross section of the coil, the magnetic flux density distribution is shown. The highest values of the magnetic flux density in the coil are near the magnet array. In these areas the force density is the highest. The arm ^cr_z for the first harmonic, $k = l = 1$, is shown with the bold arrow. The volume current density of the coil can be replaced by a sheet current, indicated by the bold horizontal line in the coil.

With the introduction of ^cr_z, the volume integral to calculate the torque can also be split into an integral over ^cz, which is solved analytically, and a surface integral over ^cx and ^cy, which is solved analytically in the straight segments of the coil and numerically in the corner segments of the coil

$$
^c\vec{T} = -\sum_{k=1}^{\infty}\sum_{l=1}^{\infty} \int_{V_{coil}} \left(^c\vec{x} - {}^c\vec{p}\right) \times \left({}^c\vec{J} \times {}^{\mathbf{c}}\mathbf{R_m}\,^m\vec{B}_3\left(^{\mathbf{m}}\mathbf{R_c}\left(^c\vec{x} - {}^c\vec{p}\right)\right) \right) \mathrm{d}^cV
$$

$$
= -\sum_{k=1}^{\infty}\sum_{l=1}^{\infty} \int_{c_b}^{c_t} e^{\lambda(^cz - {}^cp_z)}\mathrm{d}^cz \iint_{S_{coil}} \begin{bmatrix} ^cx - {}^cp_x \\ ^cy - {}^cp_y \\ ^cr_z \end{bmatrix}
$$

$$
\times \left({}^c\vec{J} \times {}^{\mathbf{c}}\mathbf{R_m}\,^m\vec{B}_{3xy}\left(^{\mathbf{m}}\mathbf{R_c}\left(^c\vec{x} - {}^c\vec{p}\right), k, l\right) \mathrm{d}^cx\mathrm{d}^cy \right). \quad (3.62)
$$

The analytical solutions of the integrals (3.59) and (3.62) are not given because of their complexity.

3.6   Analytical model

The commutation algorithm of the planar actuator, which is described in section 4.3 decouples the force and torque and the coil currents. The algorithm uses a model of the force and torque in the actuator. This model is evaluated every sample time on a real-time DSP system. The calculation time of the model should be as low as possible and, therefore, an analytical model of the planar actuator is used. The analytical model is derived from the harmonic model.

3.6.1   Magnetic flux density distribution

The analytical model only takes the first harmonic of the magnetic flux density distribution of the permanent-magnet array into account. The consequences of neglecting the higher harmonics in the commutation algorithm will be further investigated in section 5.4. The magnetic flux density expression in (3.55) simplifies to

$$
{}^{m}\vec{B}_3\left({}^{m}\vec{x}\right) = -e^{\frac{\sqrt{2}\pi}{\tau}\,{}^{m}z}
\begin{bmatrix}
B_{xy}\cos\left(\dfrac{\pi\,{}^{m}x}{\tau}\right)\sin\left(\dfrac{\pi\,{}^{m}y}{\tau}\right) \\[2mm]
B_{xy}\sin\left(\dfrac{\pi\,{}^{m}x}{\tau}\right)\cos\left(\dfrac{\pi\,{}^{m}y}{\tau}\right) \\[2mm]
B_{z}\sin\left(\dfrac{\pi\,{}^{m}x}{\tau}\right)\sin\left(\dfrac{\pi\,{}^{m}y}{\tau}\right)
\end{bmatrix},
\tag{3.63}
$$

where B_{xy} and B_z are the amplitudes of the mean value of the first harmonic of the magnetic flux density components in the cross section of the coil (as shown in Figure 3.6b) at ${}^{m}z = 0$. It can be derived from (3.55) that

$$
B_z = \sqrt{2}B_{xy}.
\tag{3.64}
$$

Transformation of this expression into the global coordinate system of the coils

$$
{}^{c}\vec{B}_3\left({}^{c}\vec{x}, {}^{c}\vec{p}\right) = {}^{c}\mathbf{R_m}\,{}^{m}\vec{B}_3\left({}^{m}\mathbf{R_c}\left({}^{c}\vec{x} - {}^{c}\vec{p}\right)\right),
\tag{3.65}
$$

results in (assuming $\phi = -\pi/4$ rad and $\psi = \theta = 0$ rad)

$$
{}^{c}\vec{B}_3({}^{c}\vec{x}, \vec{0}) =
\begin{bmatrix}
-\dfrac{B_{xy}}{\sqrt{2}}e^{\frac{\sqrt{2}\pi}{\tau}\,{}^{c}z}\sin\left(\dfrac{{}^{c}x\sqrt{2}\pi}{\tau}\right) \\[3mm]
\dfrac{B_{xy}}{\sqrt{2}}e^{\frac{\sqrt{2}\pi}{\tau}\,{}^{c}z}\sin\left(\dfrac{{}^{c}y\sqrt{2}\pi}{\tau}\right) \\[3mm]
\dfrac{1}{2}B_z e^{\frac{\sqrt{2}\pi}{\tau}\,{}^{c}z}\left(\cos\left(\dfrac{{}^{c}x\sqrt{2}\pi}{\tau}\right) - \cos\left(\dfrac{{}^{c}y\sqrt{2}\pi}{\tau}\right)\right)
\end{bmatrix}.
\tag{3.66}
$$

If $\phi = \pm\pi/4$, a new pole pitch τ_n can be introduced, which is also indicated in Figure 3.6

$$\tau_n = \frac{\tau}{\sqrt{2}}. \tag{3.67}$$

The clearance between the translator and the stator is small (several millimeters) and, consequently, the rotation angles are limited. The rotation angles can be taken into account with the first order Taylor-expansion for the angles ψ, θ and ϕ

$$^c\vec{B}_3 \approx \left. {^c\vec{B}_3} \right|_{\psi=\theta=0,\ \phi=-\frac{\pi}{4}} + \psi \cdot \left. \frac{\partial\, {^c\vec{B}_3}}{\partial\psi} \right|_{\psi=\theta=0,\phi=-\frac{\pi}{4}}$$

$$+ \theta \cdot \left. \frac{\partial\, {^c\vec{B}_3}}{\partial\theta} \right|_{\psi=\theta=0,\phi=-\frac{\pi}{4}} + \phi \cdot \left. \frac{\partial\, {^c\vec{B}_3}}{\partial\phi} \right|_{\psi=\theta=0,\phi=-\frac{\pi}{4}}. \tag{3.68}$$

3.6.2   Force and torque

The harmonic model calculates the force and torque numerically in the corner segments of the coil. To obtain a fully analytical model, the corner segments are neglected. The coil is modeled by either four surfaces or four filaments. Figure 3.6 shows the two coil models. The locations of the filaments and the surfaces in the ^cz-direction are calculated using the effective torque arm. In the ^cx- and ^cy-directions, the filaments are located in the center of the conductor bundle.

   The Lorentz force on the filaments is calculated by solving a line integral. The force exerted on the translator $^c\vec{F} = \begin{bmatrix} {^cF_x} & {^cF_y} & {^cF_z} \end{bmatrix}^\mathsf{T}$, expressed in the global coordinate system, by one coil, which center is located at (^cx ^cy 0), is equal to

$$\begin{aligned}
{^c\vec{F}} \;=\; & -\oint_C {^c\vec{i}} \times {^c\vec{B}_3} \mathrm{d}l = \\
& -\int_{^cx-w/2}^{^cx+w/2} [i\ \ 0\ \ 0]^\mathsf{T} \times {^c\vec{B}_3}\left([{^cx'}\ \ {^cy} - cl/2\ \ 0]^\mathsf{T}, {^c\vec{p}}\right)\mathrm{d}^cx' \\
& -\int_{^cy-cl/2}^{^cy+cl/2} [0\ \ i\ \ 0]^\mathsf{T} \times {^c\vec{B}_3}\left([{^cx} + w/2\ \ {^cy'}\ \ 0]^\mathsf{T}, {^c\vec{p}}\right)\mathrm{d}^cy' \\
& -\int_{^cx-w/2}^{^cx+w/2} [-i\ \ 0\ \ 0]^\mathsf{T} \times {^c\vec{B}_3}\left([{^cx'}\ \ {^cy} + cl/2\ \ 0]^\mathsf{T}, {^c\vec{p}}\right)\mathrm{d}^cx' \\
& -\int_{^cy-cl/2}^{^cy+cl/2} [0\ \ -i\ \ 0]^\mathsf{T} \times {^c\vec{B}_3}\left([{^cx} - w/2\ \ {^cy'}\ \ 0]^\mathsf{T}, {^c\vec{p}}\right)\mathrm{d}^cy',
\end{aligned} \tag{3.69}$$

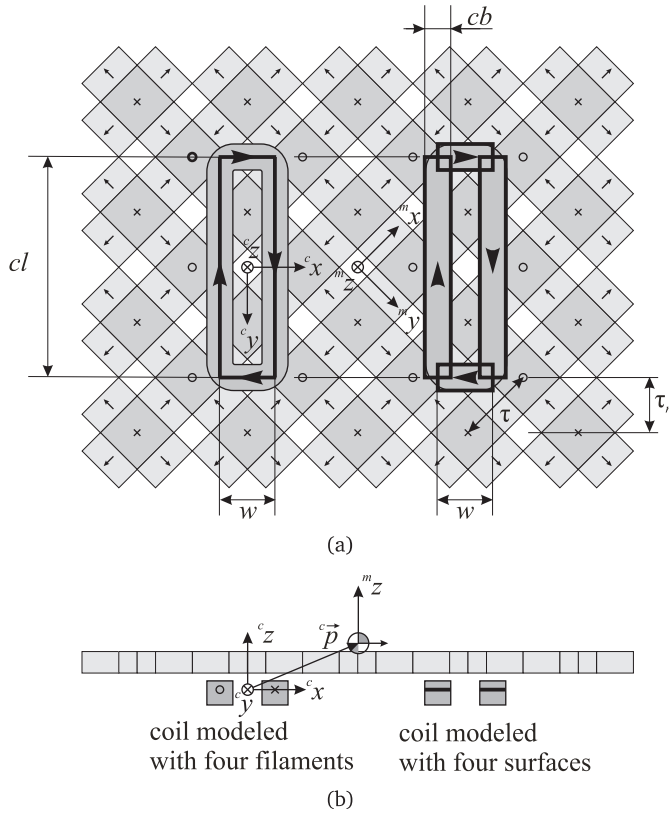**Figure 3.6.** *Coil model with filaments (left) and with surfaces (right): a) Bottom view, b) cross section.*

where w and cl are the sizes of the filament coil along the ^cx- and ^cy-directions, respectively, and i is the current through the coil in Ampere-turns.

The torque exerted on the translator $^c\vec{T} = \begin{bmatrix} ^cT_x & ^cT_y & ^cT_z \end{bmatrix}^\mathsf{T}$, expressed in

the global coordinate system, by the same coil is equal to

$$
\begin{aligned}
{}^c\vec{T} = \ & -\oint_{C_c} \left({}^c\vec{x} - {}^c\vec{p}\right) \times \left({}^c\vec{i} \times {}^c\vec{B}_3\right) \mathrm{d}l = \\
& -\int_{{}^cx-w/2}^{{}^cx+w/2} \left({}^c\vec{x} - {}^c\vec{p}\right) \times \left([i\ 0\ 0]^\mathsf{T} \times {}^c\vec{B}_3\left([{}^cx'\ {}^cy - cl/2\ 0]^\mathsf{T},\ {}^c\vec{p}\right)\right) \mathrm{d}^c x' \\
& -\int_{{}^cy-cl/2}^{{}^cy+cl/2} \left({}^c\vec{x} - {}^c\vec{p}\right) \times \left([0\ i\ 0]^\mathsf{T} \times {}^c\vec{B}_3\left([{}^cx + w/2\ {}^cy'\ 0]^\mathsf{T},\ {}^c\vec{p}\right)\right) \mathrm{d}^c y' \\
& -\int_{{}^cx-w/2}^{{}^cx+w/2} \left({}^c\vec{x} - {}^c\vec{p}\right) \times \left([-i\ 0\ 0]^\mathsf{T} \times {}^c\vec{B}_3\left([{}^cx'\ {}^cy + cl/2\ 0]^\mathsf{T},\ {}^c\vec{p}\right)\right) \mathrm{d}^c x' \\
& -\int_{{}^cy-cl/2}^{{}^cy+cl/2} \left({}^c\vec{x} - {}^c\vec{p}\right) \times \left([0\ -i\ 0]^\mathsf{T} \times {}^c\vec{B}_3\left([{}^cx - w/2\ {}^cy'\ 0]^\mathsf{T},\ {}^c\vec{p}\right)\right) \mathrm{d}^c y'.
\end{aligned}
$$
$$(3.70)$$

If the length of the coil $cl = 2n\tau_n$, where n is an integer, and if $\phi = -\pi/4$ rad and $\psi = \theta = 0$ rad, the coil only produces force in the ${}^cx$- and ${}^cz$-directions and the force is independent of the ${}^cp_y$-position of the magnet array. The force and torque expressions for a coil with $w = \tau_n$ and $cl = 4\tau_n$ are given by

$$
{}^cF_x = -2\sqrt{2}B_z i\tau e^{-\frac{\sqrt{2}\pi}{\tau}\,{}^cp_z} \sin\left(\frac{\sqrt{2}\pi\left({}^cp_x - {}^cx\right)}{\tau}\right), \tag{3.71}
$$

$$
{}^cF_y = 0, \tag{3.72}
$$

$$
{}^cF_z = -4B_{xy} i\tau e^{-\frac{\sqrt{2}\pi}{\tau}\,{}^cp_z} \cos\left(\frac{\sqrt{2}\pi\left({}^cp_x - {}^cx\right)}{\tau}\right), \tag{3.73}
$$

$$
{}^cT_x = \left({}^cy - {}^cp_y\right){}^cF_z - \sqrt{2}B_{xy} i\tau^2 e^{-\frac{\sqrt{2}\pi}{\tau}\,{}^cp_z} \sin\left(\frac{\sqrt{2}\pi\left({}^cp_y - {}^cy\right)}{\tau}\right), \tag{3.74}
$$

$$
{}^cT_y = \left({}^cp_x - {}^cx\right){}^cF_z - {}^cp_z{}^cF_x, \tag{3.75}
$$

$$
{}^cT_z = {}^cF_x\left({}^cp_y - {}^cy\right). \tag{3.76}
$$

Because of (3.64) the amplitudes of the ${}^cx$- and ${}^cz$-components of the force are equal. The torque component ${}^cT_x$ cannot be expressed as an arm multiplied by a force. Therefore, a single attaching point of the force in the ${}^cy$-direction cannot be defined. Hence, for accurate torque calculation, the distribution of the force over the coil should be taken into account.

The coil model with four filaments assumes that the force can be modeled to act on the center of the conductor bundle. In reality, the distribution of the force

over the conductor bundle changes with the relative position of the coil with respect to the magnet array. This can be shown by modeling the conductor bundle with a sheet or surface current. The force and torque expression for a coil with $w = \tau_n$, $cl = 4\tau_n$ and a conductor bundle width $cb = \tau_n/2$ can be expressed as ($\phi = -\pi/4$ rad and $\psi = \theta = 0$ rad)

$$^{c}F_x = -2\sqrt{2}B_z i\tau e^{-\frac{\sqrt{2}\pi}{\tau}{}^{c}p_z} \sin\left(\frac{\sqrt{2}\pi({}^{c}p_x - {}^{c}x)}{\tau}\right), \tag{3.77}$$

$$^{c}F_y = 0, \tag{3.78}$$

$$^{c}F_z = -4B_{xy} i\tau e^{-\frac{\sqrt{2}\pi}{\tau}{}^{c}p_z} \cos\left(\frac{\sqrt{2}\pi({}^{c}p_x - {}^{c}x)}{\tau}\right), \tag{3.79}$$

$$^{c}T_x = ({}^{c}y - {}^{c}p_y){}^{c}F_z - \sqrt{2}B_{xy}\, i\tau^2 e^{-\frac{\sqrt{2}\pi}{\tau}{}^{c}p_z} \sin\left(\frac{\sqrt{2}\pi({}^{c}p_y - {}^{c}y)}{\tau}\right), \tag{3.80}$$

$$^{c}T_y = ({}^{c}p_x - {}^{c}x){}^{c}F_z - {}^{c}p_z{}^{c}F_x + {}^{c}F_x\frac{B_{xy}(\pi - 4)\tau}{4B_z\pi}, \tag{3.81}$$

$$^{c}T_z = {}^{c}F_x({}^{c}p_y - {}^{c}y). \tag{3.82}$$

The obtained force and torque expressions are similar to the expressions for the coil modeled with four filaments, except for the ${}^{c}T_y$ term (3.81). ${}^{c}T_y$ contains an extra term proportional to ${}^{c}F_x$, which represents the torque caused by the change of the attaching point of the force in the conductor bundle of the coil. In the further analyses in this thesis and in the controller of the realized planar actuator, the model based on the sheet currents is used.

3.7 Transient model

The three analysis methods, described in the sections 3.4 - 3.6 are magnetostatic. The results of these methods are also valid during transient operation of the actuator, assuming that:

- The magnetic fields are quasi-static, i.e. the wavelength of the magnetic field is much larger than the actuator size,
- The force caused by eddy currents, for example eddy currents induced in the stator due to the movement of the permanent-magnet array, is negligible,

- The wire diameter of the coil is smaller than the skin-depth.

Under these circumstances, the magnetostatic analysis can be coupled with a dynamic model of the actuator. This dynamic model can be used to test controllers and to determine the amplifier specifications, of which the current and voltage specifications are the most fundamental.

The terminal voltage u of a coil in a linear synchronous machine is given by [22]

$$u = iR + \frac{\partial \Lambda}{\partial x}\frac{\mathrm{d}x}{\mathrm{d}t} + L\frac{\mathrm{d}i}{\mathrm{d}t}, \tag{3.83}$$

where $\frac{\partial \Lambda}{\partial x}$ is the change of the flux linkage of the permanent magnets with the coil and L is the inductance of the coil. The partial derivative of the flux linkage to the position, determines both the electromotive force (EMF) caused by movement in that direction

$$\text{EMF} = -\frac{\partial \Lambda}{\partial x}\frac{\mathrm{d}x}{\mathrm{d}t}, \tag{3.84}$$

and the force in that direction

$$F_x = \frac{\partial \Lambda}{\partial x}i. \tag{3.85}$$

Since the force calculation through the flux linkage and the Lorentz force are equivalent for a current loop in an external magnetic field [17], the voltage equation can be solved with the force and torque calculated with the magnetostatic models. The voltage equation for a coil which includes all the EMF terms caused by movement in all degrees-of-freedom is given by:

$$u = iR + L\frac{\mathrm{d}i}{\mathrm{d}t} + \frac{{}^c\vec{F}^\mathsf{T}}{i}\,{}^c\vec{v} + \frac{{}^c\vec{T}^\mathsf{T}}{i}\vec{\omega}, \tag{3.86}$$

where

$$^c\vec{v} = \left[\begin{array}{ccc} \dfrac{\mathrm{d}\,{}^cp_x}{\mathrm{d}t} & \dfrac{\mathrm{d}\,{}^cp_y}{\mathrm{d}t} & \dfrac{\mathrm{d}\,{}^cp_z}{\mathrm{d}t} \end{array}\right]^\mathsf{T}, \tag{3.87}$$

and

$$\vec{\omega} = \left[\begin{array}{ccc} \dfrac{\mathrm{d}\psi}{\mathrm{d}t} & \dfrac{\mathrm{d}\theta}{\mathrm{d}t} & \dfrac{\mathrm{d}\phi}{\mathrm{d}t} \end{array}\right]^\mathsf{T}. \tag{3.88}$$

In a full planar actuator, the differential equation (3.86) for every coil is coupled through the mutual inductances between that coil and the other coils of the planar actuator. The simulation of a full planar actuator is further discussed in section 6.5.

(a)   (b)
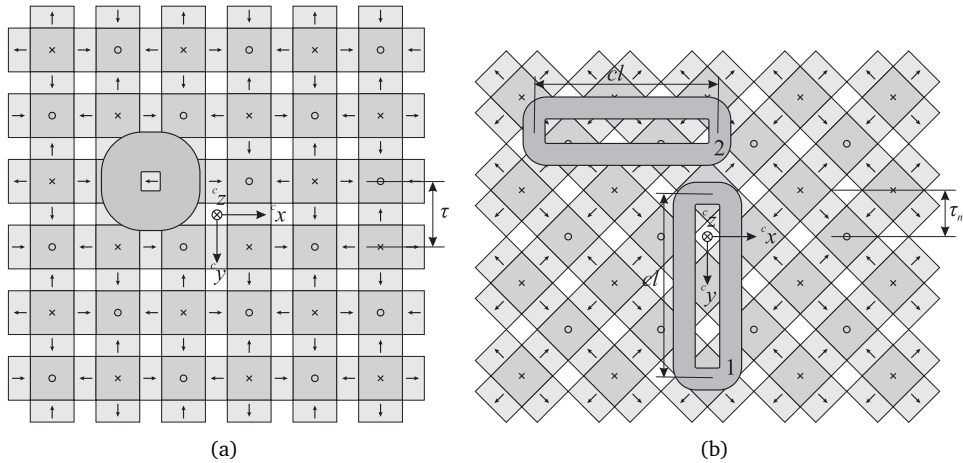
Figure 3.7. *Two types of magnet arrays and coils (bottom views): a) Magnets and square or round coil, b) magnets rotated 45 mechanical degrees with respect to the rectangular coils.*

3.8 Magnetic flux density distribution of a Halbach magnet array in a planar actuator

Because the force and torque in the planar actuator can be predicted by the Lorentz force law, the behavior of different types of planar actuators can be explained by analyzing the magnetic flux density distribution of the magnet array. The long-stroke actuators discussed in the literature overview have two types of magnet arrays and coil shapes: a magnet array which is aligned with round or square coils (section 2.4.1) and a magnet array which is rotated 45 mechanical degrees with respect to rectangular coils (sections 2.2.2 and 2.4.2). Figures 3.7a and b show two of these respective magnet arrays and the coils. Both arrays have a Halbach magnetization. The magnetic flux density distribution at 4 mm below both magnet arrays is shown in Figures 3.8 and 3.9. The magnet dimensions and properties of both magnet arrays are similar. The magnetic flux density distribution is predicted with the surface charge model and expressed in the global coordinate system. In this way the components of the magnetic flux density are shown, which are perpendicular to the currents in the coils.

Figure 3.8 shows the three components of the magnetic flux density distribu-
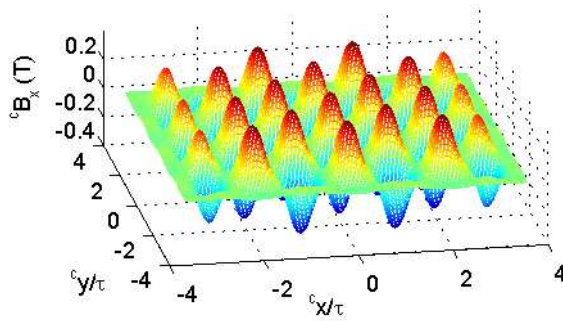
(a) Magnetic flux density in the $^c x$-direction
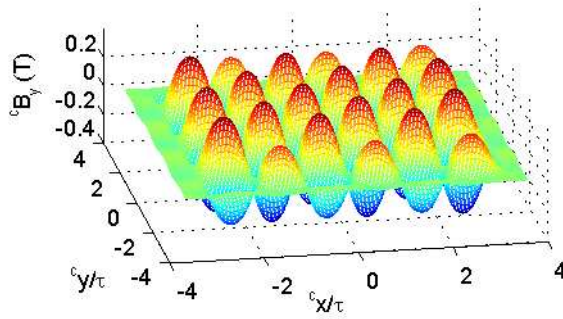
(b) Magnetic flux density in the $^c y$-direction
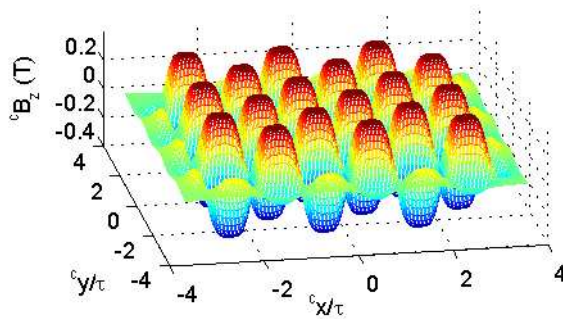
(c) Magnetic flux density in the $^c z$-direction

Figure 3.8. *Magnetic flux density distribution 4 mm below the magnet array shown in Figure 3.7a predicted with the surface charge model ($\tau = 25$ mm, $\frac{\tau_m}{\tau} = 0.68$, $B_r = 1.24$ T).*
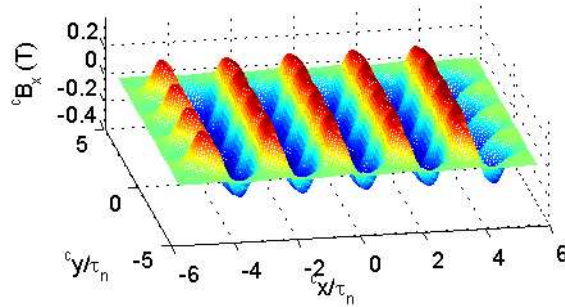
(a) Magnetic flux density in the $^c x$-direction
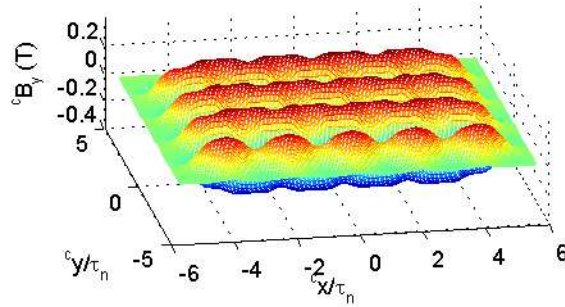
(b) Magnetic flux density in the $^c y$-direction
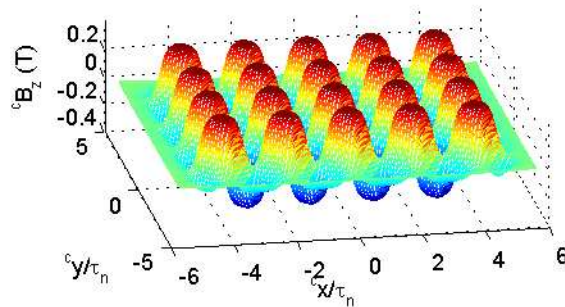
(c) Magnetic flux density in the $^c z$-direction

Figure 3.9. *Magnetic flux density distribution 4 mm below the magnet array shown in Figure 3.7b predicted with the surface charge model ($\tau = 25$ mm, $\tau_n = \frac{\tau}{\sqrt{2}} = 17.7$ mm, $\frac{\tau_m}{\tau} = 0.68$, $B_r = 1.24$ T).*
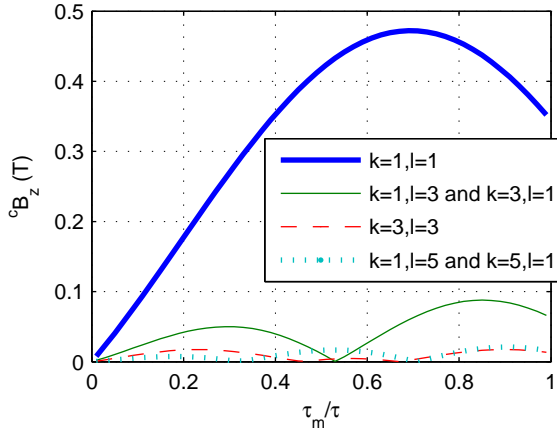
Figure 3.10. *Amplitudes of several harmonics of magnetic flux density of the magnet array shown in Figure 3.7a predicted with the harmonic model ($\tau = 25$ mm, $B_r = 1.24$ T).*

tion of the magnet array with the square coils (Figure 3.7a). The components of the magnetic flux density distribution are sine waves in both the ^cx- and ^cy-directions. The waves of the ^cB_x-, ^cB_y- and ^cB_z- components of the magnetic flux density distribution are shifted 90 electrical degrees with respect to each other, as predicted by (3.55). Due to this alternating field distribution, the size of the square coil is limited by the pole pitch τ of the magnet array.

The magnetic flux distribution of the 45 mechanical degrees (about the ^cz-axis) rotated magnet array (Figure 3.7b) is shown in Figure 3.9. Due to the rotation with respect to the reference frame, the ^cB_x component of the magnetic flux density distribution is a sine wave in the ^cx-direction and the ^cB_y component of the magnetic flux density distribution is a sine wave in the ^cy-direction. Also the ^cB_z component of the magnetic flux density distribution allows for the use of rectangular coils, which can be oriented in the two directions, as shown in Figure 3.7b. If the coil length

$$cl = 2n\tau_n, \tag{3.89}$$

where n is an integer and the coil is not near the edge of the magnet array, the field in the short sides of the rectangular coils is equal, and no force, but only a torque

is acting on the short side. Consequently, the force production in the $^c x$- and $^c y$-directions can be physically decoupled for planar actuators with rectangular coils. Coil 1 in Figure 3.7b can be displaced in the $^c y$-direction without change of the exerted force vector (3.77)-(3.79). The same holds for coil 2 when displaced in the $^c x$-direction.

Figure 3.10 shows the amplitudes of the largest harmonics of the z-component of the magnetic flux density distribution, which are also predicted 4 mm below the magnet array. These harmonics are predicted with the harmonic model for different ratios of the sizes of the magnets in the Halbach array τ_m/τ. The $k = 1, l = 3$ and the $k = 3, l = 1$ have the largest amplitude. The airgap magnetic flux density has the lowest harmonic content when $\tau_m/\tau = 0.53$, whereas the largest amplitude of the first harmonic is obtained $\tau_m/\tau = 0.70$. The influence of the ratio τ_m/τ on the force ripples in the planar actuator is further discussed in section 5.4.

3.9   Calculation time

The magnetically levitated planar actuators, which are investigated in this thesis, have a four degree-of-freedom magnetic bearing and can move over a long-stroke in the xy-plane. To analyze the behavior of such a planar actuator, at least the force and torque should be investigated for multiple positions in the xy-plane. Prediction of the force and torque on a grid of 30x30 positions in the xy-plane already involves 900 evaluations of the model. In Table 3.3 the calculation time of the different models is listed for the calculation of the force and torque in the geometry of Figure 3.1 ($\tau = 25$ mm) for one position of the magnet array. The calculation time for all models is proportional to the number of coils. The slowest model is the surface charge model, but it is fast compared to the FEM as simulations in the three-dimensional finite element package FLUX3D take 30-40 minutes. The surface charge model is mainly used to investigate the end-effects of the magnet array. The harmonic model is significantly faster than the surface charge model, because only a fractional part of the Lorentz force integral is solved numerically and the number of degrees-of-freedom is reduced. Because of the short calculation time, this model is used for the evaluations of different planar actuator designs in section 5.4. The calculation time of the analytical model is determined on the DSP system controlling the realized planar actuator and is very short. Therefore, this model can be used for the linearization and decoupling algorithm discussed in section 4.3. The required number of degrees-of-freedom of the analytical model in the commutation algorithm of the planar actuator is discussed in [73].

Table 3.3. *Computation time of the magnetostatic models for a single coil and a magnet array (Figure 3.1) on one position*

Model	DOF	Mesh size	Calculation time (s)
Surface charge model	6	1 mm^3	40
Harmonic model (25 harmonics)	3	1 mm^2	0.1
Analytical model (surface currents)	5	-	$< 2 \cdot 10^{-6}$

3.10   Conclusions

Three methods to predict the force and torque in an ironless 6-DOF moving-magnet planar actuator are presented. The methods are based on analytical solutions of the magnetic flux density distribution and analytical and numerical solutions of the force and torque using the Lorentz force law. The magnetic surface charge model is the most computational expensive because it models all permanent magnets on the translator separately. By neglecting the end-effects of the permanent-magnet array and reducing the degrees-of-freedom in the model, the force and torque can be calculated for a significant part analytically with the harmonic model. Because only four surfaces in the corners of the coil are meshed, the computation time is low. Finally, a fully analytical model is presented which can be evaluated in real-time by the controller of a planar actuator. The models have been extended to a quasi-static model to predict the terminal voltage of a coil. The force and torque calculation results of the different models will be compared with the measurements of the realized planar actuator in section 7.2.

Chapter 4

Decoupling and linearization of the force and the torque

The planar actuator can be classified as an AC synchronous permanent-magnet machine because of the sinusoidal EMF waveforms. The speed of a synchronous motor is synchronized with the frequency of the currents. To simplify the control of these machines, mathematical transformations are applied to remove the position dependency from the non-linear motor models, and to describe the motor with linear equations. The same approach is applied to the planar actuator. However, the coils in the planar actuator are simultaneously used for the active magnetic bearing and propulsion of the translator in the xy-plane. Therefore, standard decoupling and linearization schemes for synchronous motors cannot be applied and a new direct wrench-current decoupling has been developed.

Research into decoupling and linearization algorithm is on the boundary of electromechanics and control engineering because it affects both the actuator design and the controller design. The commutation algorithms presented in this chapter are the result of common research work. The decoupling and linearization algorithm is described in more detail in [73]. The theoretical and experimental results of the commutation algorithm have been published in [74, 75, 76].

It is assumed that all quantities are expressed in the global coordinate frame which is located on the stator of the planar actuator and is indicated in the drawings. The vector $\vec{q}$

$$\vec{q} = \begin{bmatrix} p_x & p_y & p_z & \psi & \theta & \phi \end{bmatrix}^\mathsf{T}, \tag{4.1}$$

is the position and orientation of the translator in this global reference frame. The superscripts indicating the different coordinate systems are not used anymore.

4.1 $dq0$-decomposition

In three-phase synchronous machine analysis and control, Park's transformation [56] (the $dq0$-transformation) is commonly used for the decoupling of machine variables, such as the currents, flux linkages and inductances. The stator quantities are transformed onto a reference frame which is fixed to the rotor. Position dependent quantities are eliminated with the power invariant transformation. Figure 4.1 shows an idealized synchronous machine and the dq-frame. The d-axis or direct axis is aligned with the rotor permanent-magnet flux and the q-axis or quadrature axis is leading the positive d-axis with 90 electrical degrees. The machine quantities in the stationary three-phase coordinate frame (a, b, c) can be expressed in a direct-axis component and a quadrature-axis component using the transformation matrix [55]

$$\begin{bmatrix} d \\ q \\ 0 \end{bmatrix} = \frac{2}{3} \begin{bmatrix} \cos(\eta) & \cos(\eta - \frac{2\pi}{3}) & \cos(\eta + \frac{2\pi}{3}) \\ -\sin(\eta) & -\sin(\eta - \frac{2\pi}{3}) & -\sin(\eta + \frac{2\pi}{3}) \\ \frac{1}{2} & \frac{1}{2} & \frac{1}{2} \end{bmatrix} \begin{bmatrix} a \\ b \\ c \end{bmatrix}, \qquad (4.2)$$

where η is the electrical angle between the rotor and the stator phase a-axis. In non-salient machines with surface mounted permanent magnets ($L_d \approx L_q$), such as the planar actuator, the q-axis current is proportional to the propulsion force (or the torque in rotating machines). The flux caused by the d-axis current can counteract the permanent-magnet flux. In planar actuators, the d-axis current will cause the levitation force.

   The force components in planar actuators can be decoupled using Park's transformation, when the rotations angles are neglected. Figure 4.2 shows two three-phase coil groups, which are arranged in a herringbone pattern, and a 45 (mechanical) degrees rotated magnet array. The coils in the light gray group can only produce force in the x- and z-directions and the coils in the dark gray group only in the y- and z-directions because the coil length $cl = 4\tau_n$ (see also sections 3.6 and 3.8). An analytical model (see also section 3.6) is derived to predict the force exerted on the magnet array. The force $\vec{F}$ produced by the light gray coil group coil can be expressed as

$$\vec{F} = \begin{bmatrix} F_x \\ F_z \end{bmatrix} = \mathbf{\Gamma_F}(\vec{p})\vec{i} =$$

$$\begin{bmatrix} -K_x(p_z) \sin\left(\frac{\pi p_x}{\tau_n} \right) & -K_x(p_z) \sin\left(\frac{\pi p_x}{\tau_n} + \frac{4\pi}{3} \right) & -K_x(p_z) \sin\left(\frac{\pi p_x}{\tau_n} - \frac{4\pi}{3} \right) \\ -K_z(p_z) \cos\left(\frac{\pi p_x}{\tau_n} \right) & -K_z(p_z) \cos\left(\frac{\pi p_x}{\tau_n} + \frac{4\pi}{3} \right) & -K_z(p_z) \cos\left(\frac{\pi p_x}{\tau_n} - \frac{4\pi}{3} \right) \end{bmatrix} \vec{i},$$

$$(4.3)$$
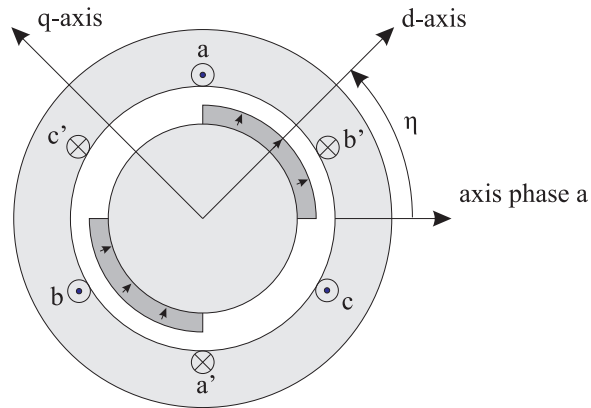
Figure 4.1. *Synchronous machine with the dq-frame.*
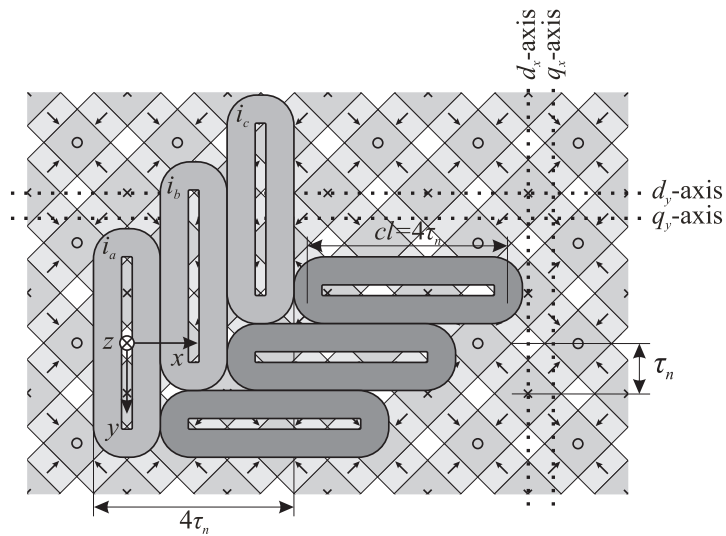
Figure 4.2. *Two 3-phase coil groups and a 45 mechanical degrees rotated magnet array.*

where

$$\vec{i} = \begin{bmatrix} i_a & i_b & i_c \end{bmatrix}^{\mathsf{T}}, \tag{4.4}$$

and where $\vec{p}$ is the position of the magnet array in the global coordinate system, τ_n is the pole pitch of the (45 mechanical degrees rotated) magnet array, and $K_x(p_z)$ and $K_z(p_z)$ are the propulsion and levitation force functions, respectively. The matrix $\mathbf{\Gamma_F}(\vec{p})$, which contains the force functions, is independent of the y-position of the coils. Therefore, the obtained results also apply to the three-phase coil groups in the actuator discussed in section 2.2.2.

If the following $qd0$-transformation matrix $\mathbf{T}_{qd0}$ is applied (with swapped d- and q-axes)

$$\mathbf{T}_{qd0} = \frac{2}{3} \begin{bmatrix} -\sin(\eta) & -\sin(\eta - \frac{4\pi}{3}) & -\sin(\eta + \frac{4\pi}{3}) \\ \cos(\eta) & \cos(\eta - \frac{4\pi}{3}) & \cos(\eta + \frac{4\pi}{3}) \\ \frac{1}{2} & \frac{1}{2} & \frac{1}{2} \end{bmatrix}, \tag{4.5}$$

where

$$\eta = \frac{\pi p_x}{\tau_n}, \tag{4.6}$$

the force produced by the light gray coil group is given by

$$\vec{F} = \begin{bmatrix} F_x \\ F_z \end{bmatrix} = \mathbf{\Gamma_F}(\vec{p})\mathbf{T}_{qd0}^{-1} \begin{bmatrix} i_q \\ i_d \\ i_0 \end{bmatrix} = \frac{3}{2} \begin{bmatrix} K_x(p_z)i_q \\ -K_z(p_z)i_d \end{bmatrix}. \tag{4.7}$$

Hence, a negative d-axis current (i.e. the magnetic flux density of the magnets is counteracted by the magnetic flux density of the coils) causes the levitation force. The q-axis current is proportional to the propulsion force. The 0-axis current (a DC-current) does not influence these force components. The same result can be obtained for the dark gray coil group. Two sets of d- and q-axes are indicated in Fig. 4.2. The d_x- and q_x-axes belong to the vertically aligned light gray coils and the d_y- and q_y-axes to the horizontally aligned dark gray coils.

The same approach can be applied to the group of four square coils which are shown in Figure 4.3. The coils are displaced 270 electrical degrees in two directions, similar to the actuator discussed in section 2.4.1. Also for these coils, an analytical model has been derived with the same method as described in section 3.6. The
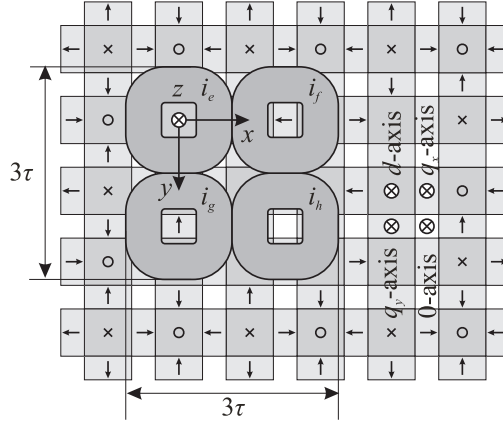
Figure 4.3. *Two-dimensional semi-four-phase coil group and a magnet array.*

force $\vec{F}$ is given by

$$
\vec{F} = \begin{bmatrix} F_x \\ F_y \\ F_z \end{bmatrix} = \mathbf{\Gamma_F}(\vec{p})\vec{i} =
$$

$$
\begin{bmatrix}
-K_x s(\eta_x)c(\eta_y) & -K_x c(\eta_x)c(\eta_y) & K_x s(\eta_x)s(\eta_y) & K_x c(\eta_x)s(\eta_y) \\
-K_y c(\eta_x)s(\eta_y) & K_y s(\eta_x)s(\eta_y) & -K_y c(\eta_x)c(\eta_y) & K_y s(\eta_x)c(\eta_y) \\
-K_z c(\eta_x)c(\eta_y) & K_z s(\eta_x)c(\eta_y) & K_z c(\eta_x)s(\eta_y) & -K_z s(\eta_x)s(\eta_y)
\end{bmatrix} \vec{i}, \quad (4.8)
$$

where

$$
s(\eta_x) = \sin\left(\frac{\pi p_x}{\tau}\right), \tag{4.9}
$$

$$
c(\eta_x) = \cos\left(\frac{\pi p_x}{\tau}\right), \tag{4.10}
$$

$$
s(\eta_y) = \sin\left(\frac{\pi p_y}{\tau}\right), \tag{4.11}
$$

$$
c(\eta_y) = \cos\left(\frac{\pi p_y}{\tau}\right), \tag{4.12}
$$

$$
\vec{i} = \begin{bmatrix} i_e & i_f & i_g & i_h \end{bmatrix}^{\mathsf{T}}. \tag{4.13}
$$
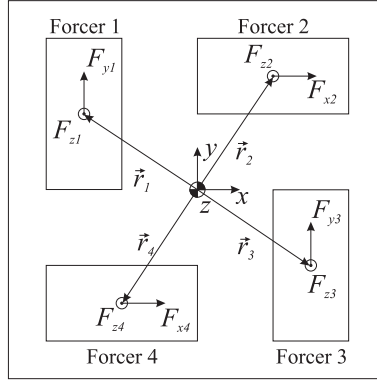
Figure 4.4. *Body diagram of the translator of a planar actuator with four forcers.*

For notional reasons, the p_z-dependency of the force constants K_x, K_y and K_z is omitted. In this actuator, a d-axis, a q_x-axis, a q_y-axis and even a 0-axis can be defined. These axes are shown in Figure 4.3. Contrary to the standard $dq0$-transformation, the 0-axis is not a DC-term. The transformation matrix for this coil group is equal to

$$
\mathbf{T}_{q_x q_y d0} =
\begin{bmatrix}
-s(\eta_x)c(\eta_y) & -c(\eta_x)c(\eta_y) & s(\eta_x)s(\eta_y) & c(\eta_x)s(\eta_y) \\
-c(\eta_x)s(\eta_y) & s(\eta_x)s(\eta_y) & -c(\eta_x)c(\eta_y) & s(\eta_x)c(\eta_y) \\
c(\eta_x)c(\eta_y) & -s(\eta_x)c(\eta_y) & -c(\eta_x)s(\eta_y) & s(\eta_x)s(\eta_y) \\
s(\eta_x)s(\eta_y) & c(\eta_x)s(\eta_y) & s(\eta_x)c(\eta_y) & c(\eta_x)c(\eta_y)
\end{bmatrix} .
\tag{4.14}
$$

The force produced by the coils can be expressed as

$$
\vec{F} =
\begin{bmatrix}
F_x \\
F_y \\
F_z
\end{bmatrix}
= \mathbf{\Gamma_F}(\vec{p})\mathbf{T}_{q_x q_y d0}^{-1}
\begin{bmatrix}
i_{q_x} \\
i_{q_y} \\
i_d \\
i_0
\end{bmatrix}
=
\begin{bmatrix}
K_x(p_z)i_{q_x} \\
K_y(p_z)i_{q_y} \\
-K_z(p_z)i_d
\end{bmatrix} .
\tag{4.15}
$$

The $dq0$-decomposition has been successfully applied in the control of both a short-stroke 6-DOF moving-magnet planar actuator (section 2.2.1) and a 6-DOF moving-coil planar actuator (section 2.2.2). In both cases the translator is actuated by four three-phase coil groups. The force in each coil group or forcer is decoupled by the $dq0$-transformation. Each forcer produces a levitation force (proportional to

the d-axis current) and a propulsion force (proportional to the q-axis-current) in either the x- or y-direction, as illustrated in Figure 4.4. It is assumed that the force produced by these groups acts in the center of a forcer and on the translator itself. The torque exerted on the translator is calculated using the four force arms ($\vec{r}_1$-$\vec{r}_4$). Two extra constraints are added to the underdetermined system of six force and torque equations, e.g. [13]

$$F_{x2} = F_{x4}, \tag{4.16}$$
$$F_{z1} + F_{z2} = \frac{mg}{2}, \tag{4.17}$$

where m is the mass of the translator and g is the acceleration due to gravity. As a result, an unique transformation is obtained from the force and the torque to the d- and q-axis current components of each forcer. In [48] not all torque components have been taken into account in this transformation. The ignorance of these components did not make the actuator unstable. In [13, 16], it is shown that this method of decoupling leads to uncontrolled pitch torque effects, which can be reduced by optimizing the topology and the geometry of the actuator.

Contrary to short-stroke moving-magnet planar actuators, the application of the $dq0$-decomposition in long-stroke moving-magnet planar actuator is not straightforward. Due to switching between different sets of coils, forcers cannot be defined. Moreover, the torque in a moving-magnet planar actuator does not only depend on the relative position of the magnet array with respect to the coils, but also on the absolute position [16]. Therefore, design symmetries, which are used in the design of moving-coil planar actuators to reduce uncontrolled torque effects, do not exist.

An indirect method for the decoupling of the moving-magnet planar actuator discussed in section 2.4.1 is proposed in [5]. The active coils are subdivided in four groups of four coils. Such coil groups are shown in Figures 2.8b and 4.3. Firstly, the method applies Park's transformation, similar to (4.14), for the decoupling of the force in the groups of four coils. Secondly, the resulting disturbance torque in each group of four coils is calculated. Lastly, this disturbance torque is reduced with correction terms. However, no details are given about the calculation of these correction terms, and it is assumed in this analysis that the force distribution over the coil is position independent.

A new direct wrench-current decoupling scheme has been developed in this project which calculates the coil currents in one step. The method can be applied to both moving-magnet and moving-coil planar actuators. The method does not hold on to the principle of poly-phase coil groups. Consequently, coils should be excited with single-phase current amplifiers. With this method the set of active coils can be switched during the movements of the translator.
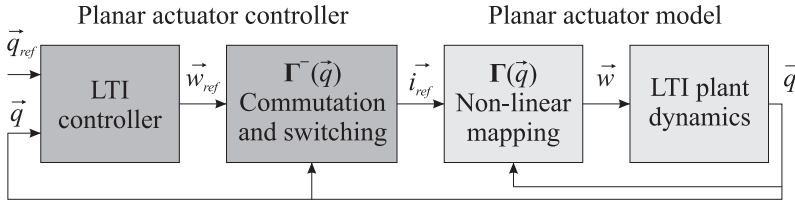
Figure 4.5. *Model of a planar actuator and controller.*

4.2   Direct wrench-current decoupling

A model of the planar actuator and the controller is shown in Figure 4.5. The model has strong similarities with standard control models for linear and rotary synchronous machines [23], because position dependent variables are eliminated in the controller and the plant dynamics by non-linear transformations. The planar actuator is modeled by two blocks. The non-linear mapping $\mathbf{\Gamma}(\vec{q})$ maps the coil currents to the wrench $\vec{w}$ as function of the position and orientation of the translator. The wrench $\vec{w}$ is the vector which contains the force and the torque

$$
\vec{w} = \begin{bmatrix} \vec{F} \\ \vec{T} \end{bmatrix} = \begin{bmatrix} F_x \\ F_y \\ F_z \\ T_x \\ T_y \\ T_z \end{bmatrix}. \tag{4.18}
$$

The linear time-invariant (LTI) plant dynamics is a model of the actuator with the mass, inertia and damping. The controller also consists of two blocks. The LTI controller determines the wrench set-point $\vec{w}_{ref}$ from the position reference and the measured position. The commutation and switching algorithm calculates the currents in the coils as function of the position of the translator. This block contains the inverse $\mathbf{\Gamma}^-(\vec{q})$ of the non-linear mapping in the model of the actuator. The power amplifiers are assumed to be ideal current sources ($\vec{i}_{ref} \equiv \vec{i}$). In synchronous rotary and linear machines, Park's transformation and its inverse are usually applied for the non-linear mapping and the commutation algorithm, respectively.

The non-linear mapping $\mathbf{\Gamma}(\vec{q})$ is a model of the planar actuator. In chapter 3 planar-actuator models have been derived. The models are linear with respect to the current and, assuming rigid body dynamics, the total force and the total torque

is the summation of the contribution of the individual coils. Therefore, with this type of models, the wrench of a planar actuator with n coils can be expressed as

$$\vec{w} = \left. \begin{bmatrix} F_{1,x}(\vec{q}) & F_{2,x}(\vec{q}) & \cdots & F_{n,x}(\vec{q}) \\ F_{1,y}(\vec{q}) & F_{2,y}(\vec{q}) & \cdots & F_{n,y}(\vec{q}) \\ F_{1,z}(\vec{q}) & F_{2,z}(\vec{q}) & \cdots & F_{n,z}(\vec{q}) \\ T_{1,x}(\vec{q}) & T_{2,x}(\vec{q}) & \cdots & T_{n,x}(\vec{q}) \\ T_{1,y}(\vec{q}) & T_{2,y}(\vec{q}) & \cdots & T_{n,y}(\vec{q}) \\ T_{1,z}(\vec{q}) & T_{2,z}(\vec{q}) & \cdots & T_{n,z}(\vec{q}) \end{bmatrix} \right|_{\vec{i}=\begin{bmatrix} 1 & \cdots & 1 \end{bmatrix}^{\mathsf{T}}} \begin{bmatrix} i_1 \\ i_2 \\ \vdots \\ i_n \end{bmatrix} = \mathbf{\Gamma}(\vec{q})\vec{i},$$

(4.19)

where the force and the torque elements in $\mathbf{\Gamma}(\vec{q})$ are expressed on a per Ampere basis. As the planar actuator is usually over-actuated, the system of equations is underdetermined and there is an infinitely large set of solutions for the inverse. A convenient solution to search for is the inverse with minimal ohmic losses in the actuator or the 2-norm minimization of the current. Moreover, this solution results in continuous coil currents. The 2-norm minimization is obtained by the Moore-Penrose inverse or pseudo-inverse of $\mathbf{\Gamma}(\vec{q})$[61]

$$\min_{\mathbf{\Gamma}(\vec{q})\vec{i}=\vec{w}} \left\| \vec{i} \right\|_2 = \left\| \mathbf{\Gamma}^-(\vec{q})\vec{w} \right\|_2,$$

(4.20)

where

$$\mathbf{\Gamma}^-(\vec{q}) = \mathbf{\Gamma}(\vec{q})^{\mathsf{T}} \left(\mathbf{\Gamma}(\vec{q})\mathbf{\Gamma}(\vec{q})^{\mathsf{T}} \right)^{-1},$$

(4.21)

when the resistances of all coils are equal. In [60], an identical direct approach is applied.

The pseudo-inverse solution has similarities with the $dq0$-decomposition [76]. The force and the torque in both the wrench vector $\vec{w}$ and the model $\mathbf{\Gamma}(\vec{q})$ can be split

$$\vec{w} = \begin{bmatrix} \vec{F} \\ \vec{T} \end{bmatrix} = \mathbf{\Gamma}(\vec{q})\vec{i} = \begin{bmatrix} \mathbf{\Gamma_F} \\ \mathbf{\Gamma_T} \end{bmatrix} \vec{i}.$$

(4.22)

Using [32], the current can be expressed as

$$\vec{i} = \mathbf{\Gamma_T^-}\vec{T} + (\mathbf{I} - \mathbf{\Gamma_T^-}\mathbf{\Gamma_T})\mathbf{\Gamma_F^-}\vec{F},$$

(4.23)

where

$$\mathbf{\Gamma_F^-} = \mathbf{\Gamma_F}^{\mathsf{T}}(\mathbf{\Gamma_F}\mathbf{\Gamma_F}^{\mathsf{T}})^{-1},$$

(4.24)

$$\mathbf{\Gamma_T^-} = \mathbf{\Phi_T}\mathbf{\Gamma_T}^{\mathsf{T}}(\mathbf{\Gamma_T}\mathbf{\Phi_T}\mathbf{\Gamma_T}^{\mathsf{T}})^{-1},$$

(4.25)

$$\mathbf{\Phi_T} = (\mathbf{I} - \mathbf{\Gamma_F^-}\mathbf{\Gamma_F}),$$

(4.26)

and where $\mathbf{I}$ is the identity matrix. The current in the coils consists of three terms:

- $\mathbf{\Gamma_T^-}\vec{T}$ causes the torque $\vec{T}$ on the translator but no resulting force.
- $\mathbf{\Gamma_F^-}\vec{F}$ causes the force $\vec{F}$ on the translator. $\mathbf{\Gamma_F^-}$ is the inverse $dq0$-transformation when the coils are distributed according to a poly-phase system and the end-effects can be neglected.
- $-\mathbf{\Gamma_T^-}\mathbf{\Gamma_T}\mathbf{\Gamma_F^-}\vec{F}$ changes the distribution of the force caused by the previous term in order to eliminate its torque. This term can significantly contribute to the power dissipation in the planar actuator when the translator is accelerated in the xy-plane. To reduce this contribution, the mass center point of the translator should be located as close as possible to the stator coils.

The term $(\mathbf{I}-\mathbf{\Gamma_T^-}\mathbf{\Gamma_T})$ multiplied by an arbitrary vector is the null space of the torque. Therefore, multiplication of an arbitrary vector with this term does not change the torque acting on the translator.

4.3   Direct wrench-current decoupling with switching between coil-sets

As the Moore-Penrose inverse minimizes the ohmic losses in the coils, there are only significant currents in the coils below the magnet array, since only these coils can efficiently produce force and torque. Consequently, the currents are automatically reduced in the coils near the edges of the magnet array. This commutation algorithm requires a model of the actuator in $\mathbf{\Gamma}(\vec{q})$ which is valid over the full stroke of the actuator, such as the magnetic surface charge model presented in section 3.4. However, this model is computationally expensive because of the numerical integration. When this model is stored in a multi-dimensional look-up table, it requires a large amount of memory and interpolation between data points.

In this project an alternative method is chosen. A computational inexpensive model of the actuator, the analytical model presented in section 3.6, is used in the commutation algorithm of the planar actuator. This model can be evaluated and inverted at sample rates of several kHz by the DSP system controlling the planar actuator. Because the edge effects of the magnet array are not included in this model, additional constraints should be added to the minimization criterion to use only the set of coils for which the model is valid. With these extra constraints the currents in the coils near the edges of the magnet array can be reduced and smooth switching between different sets of active coils is possible.

A smooth diagonal weighting matrix $\mathbf{\Delta}$ contains the extra constraints. As a
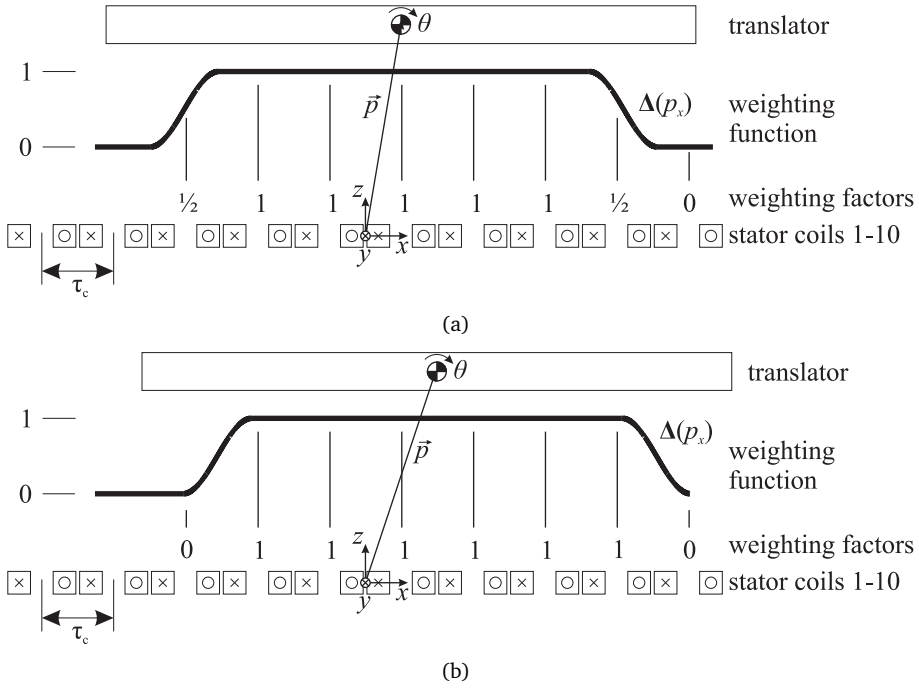
Figure 4.6. *Example of the application of a one-dimensional weighting function in a 3-DOF actuator: a) Seven active coils, b) six active coils at the transition between two coil-sets.*

result, the weighted 2-norm minimization becomes

$$\min_{\mathbf{\Gamma}(\vec{q})\vec{i}=\vec{w}} \left|\left|\vec{i}\right|\right|_{2,\,\mathbf{\Delta}^{-1}(\vec{q})} = \left|\left|\mathbf{\Gamma}^{-}(\vec{q})\vec{w}\right|\right|_{2}, \tag{4.27}$$

where

$$\mathbf{\Gamma}^{-}(\vec{q}) = \mathbf{\Delta}(\vec{q})\mathbf{\Gamma}(\vec{q})^{\mathsf{T}}\left(\mathbf{\Gamma}(\vec{q})\mathbf{\Delta}(\vec{q})\mathbf{\Gamma}(\vec{q})^{\mathsf{T}}\right)^{-1}. \tag{4.28}$$

A one dimensional weighting matrix $\mathbf{\Delta}(p_x)$ illustrated in Figure 4.6. It shows a schematic overview of a 3-DOF moving-magnet actuator with ten coils with concentrated windings. The three degrees-of-freedom are translational movement in the x- and z-directions and rotational movement θ about the y-axis. The coils of

the actuator are distributed according to a semi-four-phase system, i.e. $\tau_c = \frac{3}{2}\tau_n$, where τ_c is the coil pitch. In this actuator at least five adjacent coils need to be energized to control the three degrees-of-freedom. More details about this actuator can be found in [36] and in Appendix B.

   Although the degrees-of-freedom of the actuator can be controlled with five coils, seven active coils are used in this example. When the translator moves over τ_c in the x-direction, the set of active coils changes. With ten coils, there are four different sets of seven adjacent coils. Figures 4.6a and b show two different positions of the magnet array. The weighting function moves with the translator of the actuator. The weighting factors of the individual coils are indicated in Figure 4.6. If the weighting function is equal to 1, a coil is not penalized. If the weighting function is equal to 0, a coil is maximally penalized in the 2-norm minimization and there will be no currents through this coil. To assure a smooth switching between different coil sets, the weighting function should be continuous (no current steps) and differentiable (no voltage steps). For that reason, a raised cosine function is selected as weighting function. The weighting matrix $\mathbf{\Delta}(\vec{p}_x)$ of the set of seven active coils in Figures 4.6a and b is equal to

$$\mathbf{\Delta}(p_x) = \begin{bmatrix} \frac{1}{2} + \frac{1}{2}\cos\left(\frac{\pi p_x}{\tau_c}\right) & 0 & 0 & 0 & 0 & 0 & 0 \\ 0 & 1 & 0 & 0 & 0 & 0 & 0 \\ 0 & 0 & 1 & 0 & 0 & 0 & 0 \\ 0 & 0 & 0 & 1 & 0 & 0 & 0 \\ 0 & 0 & 0 & 0 & 1 & 0 & 0 \\ 0 & 0 & 0 & 0 & 0 & 1 & 0 \\ 0 & 0 & 0 & 0 & 0 & 0 & \frac{1}{2} - \frac{1}{2}\cos\left(\frac{\pi p_x}{\tau_c}\right) \end{bmatrix}. \tag{4.29}$$

With this weighting matrix, the positions of the translator at which the set of active coils is switched, are exactly determined. Figure 4.6b shows the point at which such a transition takes place. At that position only six coils are energized.

   The 2-norm minimization with the weighting matrix can also be split into the force and the torque components

$$\vec{i} = \mathbf{\Gamma_T^-}\vec{T} + (\mathbf{I} - \mathbf{\Gamma_T^-}\mathbf{\Gamma_T})\mathbf{\Gamma_F^-}\vec{F}, \tag{4.30}$$

where

$$\mathbf{\Gamma_F^-} = \mathbf{\Delta}\mathbf{\Gamma_F}^{\mathsf{T}}(\mathbf{\Gamma_F}\mathbf{\Delta}\mathbf{\Gamma_F}^{\mathsf{T}})^{-1}, \tag{4.31}$$

$$\mathbf{\Gamma_T^-} = \mathbf{\Phi_T}\mathbf{\Gamma_T}^{\mathsf{T}}(\mathbf{\Gamma_T}\mathbf{\Phi_T}\mathbf{\Gamma_T}^{\mathsf{T}})^{-1}, \tag{4.32}$$

$$\mathbf{\Phi_T} = (\mathbf{I} - \mathbf{\Gamma_F^-}\mathbf{\Gamma_F})\mathbf{\Delta}. \tag{4.33}$$
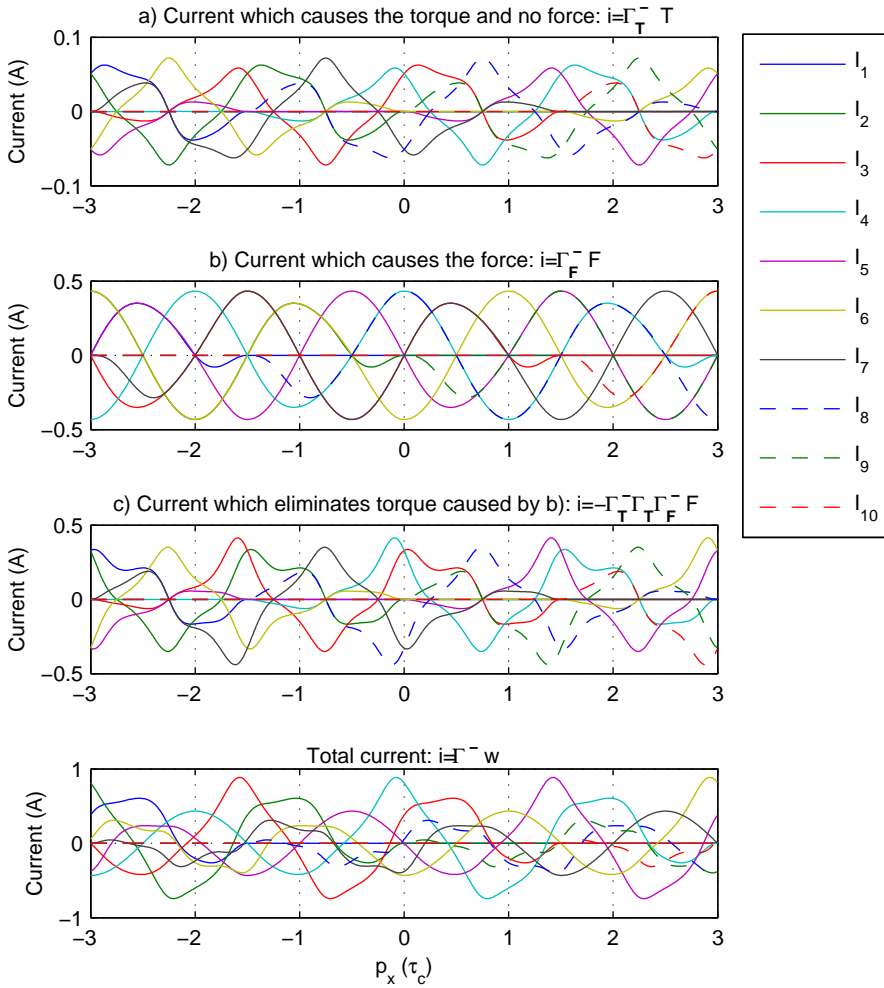
Figure 4.7. *Decomposition of the currents in the 3-DOF actuator into three components* $\vec{w} = [10 \quad 10 \quad 0.1]^{\mathsf{T}}$.

Figure 4.7 shows the decomposition of the currents to obtain a position independent force and torque vector $\vec{w} = \begin{bmatrix} F_x & F_z & T_y \end{bmatrix}^\mathsf{T} = \begin{bmatrix} 10 & 10 & 0.1 \end{bmatrix}^\mathsf{T}$ on the translator of the 3-DOF actuator (mechanical clearance: 2 mm). Because the topology of the actuator repeats over $\tau_c = \frac{3}{2}\tau_n$, the current waveforms repeat in successive coils. Figure 4.7 shows that a significant current is required to alter the force distribution obtained with the currents $i = \mathbf{\Gamma_F^-}\vec{F}$ and to compensate the torque caused by these currents. Due to the weighting function the currents $i = \mathbf{\Gamma_F^-}\vec{F}$ are not fully sinusoidal.

The 3-DOF actuator only has to switch coils while moving in the x-direction. A planar actuator has to switch between coil sets while moving both in the x- and the y-direction. Hence, the commutation algorithm of the 6-DOF planar actuator uses a two-dimensional weighting matrix $\mathbf{\Delta}(p_x, p_y) = \mathbf{\Delta_x}(p_x)\mathbf{\Delta_y}(p_y)$. The matrix is composed of one-dimensional weighting functions $\mathbf{\Delta_x}(p_x)$ and $\mathbf{\Delta_y}(p_y)$. The switching principle is the same. Figure 4.8 shows a planar actuator design (based on the actuator discussed in section 2.4.1). The actuator has 64 coils of which only 25 can be simultaneously active. The coils are distributed according to a semi-four-phase system, similar to the coils in Figure 4.3. The two weighting functions $\mathbf{\Delta_x}(p_x)$ and $\mathbf{\Delta_y}(p_y)$, which move with the magnet array, are indicated in the drawing. The active coil set is colored green, the inactive coils are colored light gray and the coils which are penalized are colored yellow.

The admissible position range of the magnet array is within the intervals $-3\tau \leq p_x \leq 3\tau$ and $-3\tau \leq p_y \leq 3\tau$. This range is subdivided into 16 numbered states with different sets of active coils (Figure 4.9). Figure 4.10 shows the active coils at the boundaries of state 7. The positions of the mass center point of the translator at these boundaries are indicated in Figure 4.11. In Figure 4.10c, all 25 coils are active and none of them is penalized by the weighting function. When the magnet array moves in the positive x-direction the left column of the active coils is switched off. At the transition between states 7 and 8 (Figure 4.10d) only 20 coils are active. When the actuator moves further in the positive x-direction, five coils in the outer right column are switched on (not shown). When the magnet array moves in the positive y-direction the bottom row of active coils is switched off. Figure 4.10a shows the active coils at the boundary of states 3 and 7. In the worst case situation at the crossing of four states, nine coils are penalized by the weighting functions and are switched off (Figure 4.10b).
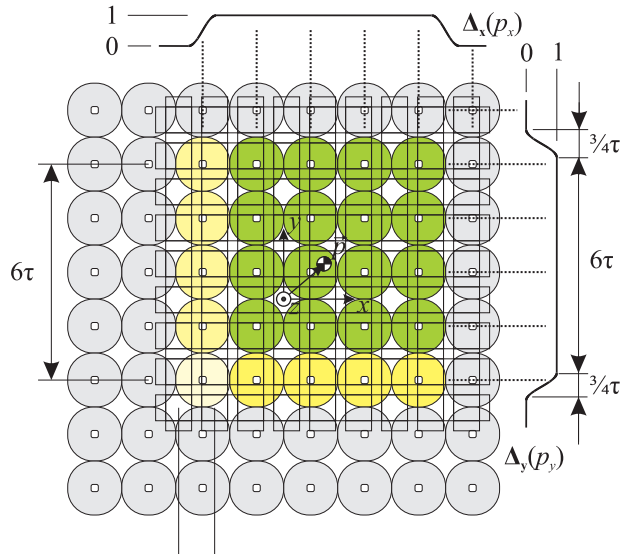
Figure 4.8. *Weighting functions for a moving-magnet planar actuator.*
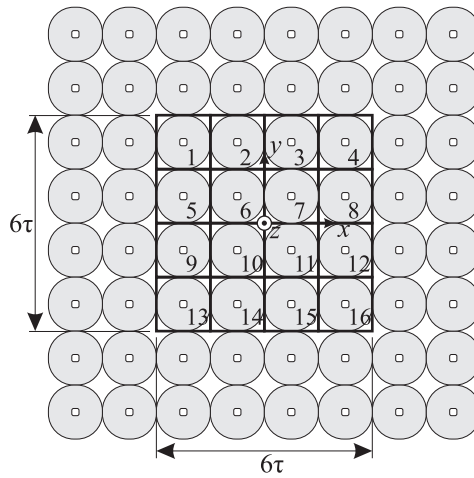
Figure 4.9. *Allowed positions of the mass center point of the translator. The admissible range is subdivided into 16 states.*

(a)

(b)

(c)

(d)
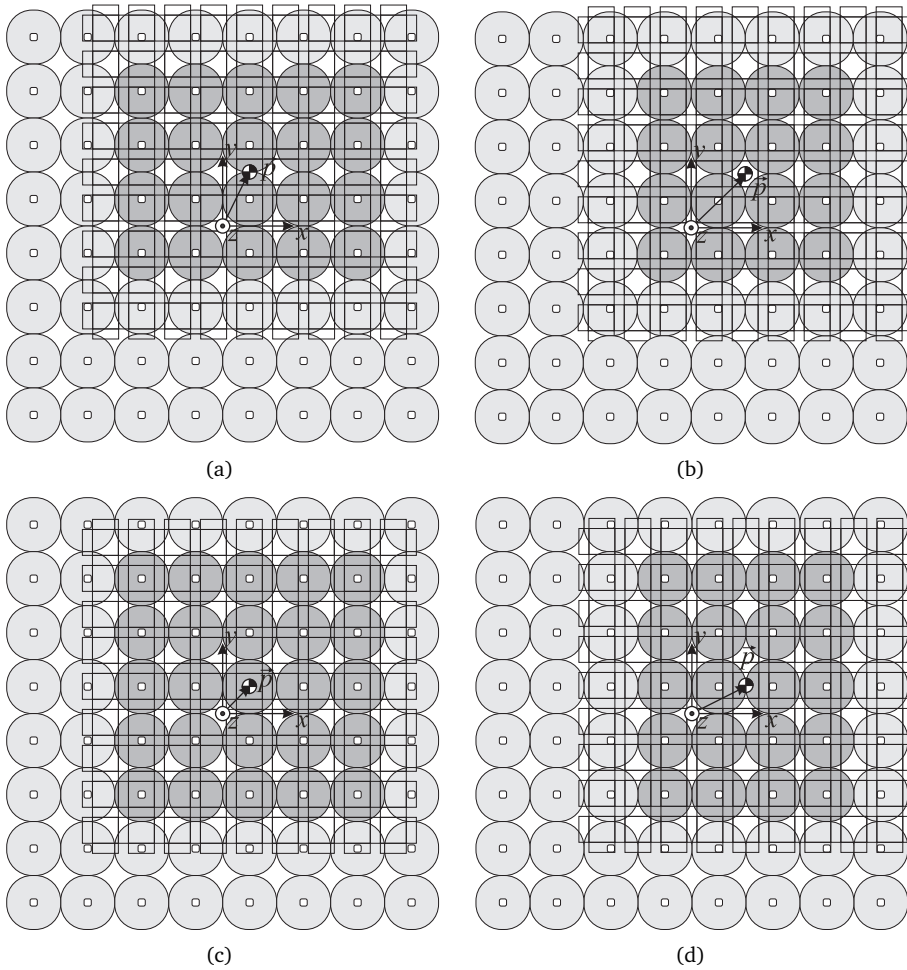
Figure 4.10. *Active coils at the transitions between different sets of coils. The position of the mass center point of the magnet array with respect to the boundaries of state 7 are indicated in Figure 4.11.*

4.4   Condition number

The topology of the 6-DOF planar actuator, i.e. the placements of the coils and permanent magnets, should be chosen in a way that all degrees-of-freedom can be
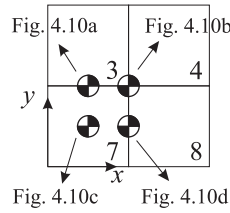
Figure 4.11. *Positions of the mass center point of the magnet array at the transitions between different coil sets for which the set of active coils are shown in Figure 4.10.*

accessed. To determine this, it should be verified that the inverse actuator model $\mathbf{\Gamma}^-(\vec{p})$ is not singular. The rank of the matrix should be equal to six for all positions and orientations of the translator. The disadvantage of determining the rank is that the rank only counts the number of independent rows and columns.

A more advanced method is to calculate the condition number of $\mathbf{\Gamma}^-(\vec{q})$. This condition number is the ratio of the largest to the smallest singular value in the singular value decomposition of the matrix [32]. The condition number is a measure of the sensitivity of the matrix inversion to perturbations in the model. Model perturbations in the planar actuator are for example caused by variation of the permanent-magnet properties, mechanical tolerances and offsets in the power amplifiers. If the condition number is infinite, the matrix is singular. If the condition number is sufficiently low, all force and torque combinations can be accurately achieved. The advantage of the use of the condition number over the rank is that also positions at which the planar actuator is ill-conditioned, can be detected. In [73], the condition number is discussed in detail.

4.5 Conclusions

A new direct current-wrench decoupling and linearization algorithm for moving-magnet planar actuators has been developed. This commutation algorithm is fully model-based. The algorithm inverts a mapping of the coil currents and the force and torque produced by these coils and minimizes the ohmic losses in the coils. A smooth weighting function is applied to switch the coils near the edge of the magnet array because the end-effect of the magnet array are not included in the analytical model used by the commutation algorithm. The mapping can also be used to evaluate the accessibility of the wrench by calculation of the condition number.

The commutation algorithm can be further improved by including the edge-effects of the magnet array in the analytical model.

Chapter 5

Synthesis of the planar actuator

Nowadays, electrical machine designers rely on experience, sizing equations and advanced computer models. The design procedure is an iterative process and often several machine topologies are investigated and compared with the requirements. For many types of permanent-magnet motors, the design procedure is described in the literature [23, 29, 26]. For novel types of electrical machines, such as the planar actuator, these procedures and sizing equations do not exist.

In this chapter, a design method for the long-stroke, magnetically levitated, moving-magnet, planar actuator is discussed. Like any design procedure, the design of the planar actuator starts with specifying the actuator. Instead of synthesizing and optimizing full planar actuator topologies, a different approach is chosen. The planar actuator is considered as a system of n voice-coil or Lorentz actuators with a common magnet array. A single Lorentz actuator and the magnet array are optimized. With these geometrically optimized coils and magnets, four planar actuators are synthesized, evaluated and compared. To determine and to compare the characteristics of these planar actuators the model presented in section 3.5 is coupled with the commutation algorithm derived in section 4.3. The design and comparison of the moving-magnet planar actuators have been published in [38, 40, 43, 35, 39].

5.1 Specification of the planar actuator

The designed planar actuator is intended for servo applications. Important characteristics of servo drives are a low power dissipation and low force and torque ripples. The four synthesized planar actuators will be compared on these criteria.

Table 5.1. *Performance specifications of the designed moving-magnet planar actuator*

Size translator	300x300 mm
Levitated mass without magnets	4.0 kg
Mechanical clearance	1 - 2 mm
Stroke xy-plane	200x200 mm
Speed xy-plane	1.0 m/s
Acceleration xy-plane	10 m/s^2

In the design, the minimization of the power dissipation is emphasized.

The first step in the design of any actuator is specifying its performance requirements and the design constraints. The performance requirements of the long-stroke, magnetically levitated, planar actuator with moving magnets are listed in Table 5.1. The translator consists of a levitated object of 300 by 300 mm and a mass of 4 kg. The magnets are glued to this carrier. There is no additional load specified. Because of the selected translator size, a square magnet array is required, and as a result, the number of possible topologies is limited. Also other multi-physical constraints should be taken into account in the design process.

Thermal design

The dynamics (motion, energy, force) of a servo drive are limited by the temperature rise of the different materials in the actuator. Because the planar actuator has a single-sided active magnetic bearing based on the Lorentz force, power is also dissipated when the translator is only levitated. The power dissipation strongly depends on the motion profile (number of movements, traveled distance, acceleration and deceleration levels, etc.). Moreover, because of the switching between different sets of coils, the power dissipation is also a function of the chosen path. During the optimization and evaluation of the different designs, thermal constraints are not taken into account. It is assumed that the obtained design can be sufficiently cooled without changing its dimensions. The thermal aspects of the planar actuator are further discussed in section 6.4.

Commutation algorithm

The accuracy of the model in the commutation algorithm influences the force and torque ripples of the planar actuator. The planar actuator is commutated using the direct current-wrench decoupling, which is presented in section 4.3. The commutation algorithm predicts the force and torque acting on the translator with the analytical model which is based on the replacement of the coils by current sheets (section 3.6). The coils are actively switched off by a weighting matrix before they are influenced by the edge-effects of the magnet array. This allows the use of the harmonic model (section 3.5) for the analysis of the force and torque ripples in the commutated planar actuator.

Power electronics

In the design process, it is assumed that each coil is connected to an ideal current source (i.e. high-bandwidth, no offset and no drift). No current and voltage constraints are taken into account. The matching of the power amplifier to the planar actuator is carried out after the selection of the actuator and will be discussed in section 6.5. Furthermore, it is assumed that the packing factor of the orthocyclically wound coils [50] is independent of the number of turns of the coil and equal to 0.67.

Mechanics

Rigid body dynamics are assumed and, consequently, the superposition principle can be applied to the force and torque calculation.

5.2 Optimization of a single coil and the magnet array

The planar actuator can be classified as an unrolled AC synchronous permanent-magnet machine with changed boundary conditions due to the end-effects of the magnet array, and with a special commutation algorithm because of the integration of motion in the xy-plane and an active magnetic bearing. The planar actuator can also be looked at from a different perspective. It can be classified as a system of n separate voice-coil or Lorentz actuators with a common mover. The Lorentz actuators are independent because the super-position principle can be applied to the calculation of the force and torque on the mover, the Lorentz actuators are connected to high-bandwidth current amplifiers and, as will be shown in section 6.5, the mutual coupling between the coils is low.

Because the Lorentz actuators can be considered to be independent, an actuator consisting of only a single coil and a translator with the magnet array is optimized. It is assumed that the translator is levitated by that single coil. The dimensions of the coil and magnet array are optimized with the objective to minimize the power dissipation. In this thesis, two coil configurations are studied. A configuration with rectangular coils which are rotated 45 mechanical degrees with respect to the magnet array and actuators with square coils which are aligned with the magnet array. Figure 5.1 shows both coil types and a magnet array with a quasi-Halbach magnetization. In the figure, the optimization variables and parameters are indicated. The optimization variables are the dimensions of the coil and the magnets. These variables are listed in Table 5.2. The parameters, which are fixed during the optimization, are listed in Table 5.3. Three different types of parameters can be distinguished:

- The topology related parameters. The topology of the planar actuator, i.e. the distribution of coils and magnets, is, amongst others, defined by the sizes of the coil, cl and cw, and the pole pitch of the magnet array, τ or τ_n. To physically decouple the force production by the rectangular coils (Figure 5.1a) in the xy-plane, the coil length is equal to

$$cl = 2n\tau_n, \tag{5.1}$$

  where n is an integer (see also section 3.6). The outer length of the rectangular coil is equal to $2n\tau_n + cb$.
- Knowledge of the magnetic flux density distribution of the permanent magnets in the airgap of the planar actuator is insufficient to predict the required electrical loading or the power dissipation, since the required force for levitation is depending the mass of the translator itself. The mass of the permanent magnets is a considerable part of the total mass of the translator. Therefore, the mass of the translator without the magnets, m_c, (the mass of the carrier to which the magnets are glued) and the mass densities of the permanent magnets, ρ_m, and the material used to fill the empty spaces in the magnet array, ρ_f, (usually an epoxy resin) are parameters in the optimization.
- The permanent magnet specifications, i.e. the remanence of the permanent magnets, B_r, and the relative permeability, μ_r.

The objective of the optimization is the minimization of the power dissipation due to levitation of the translator of the planar actuator by a single coil. This coil is aligned with the d-axis of the magnet array (see section 4.1). The objective function
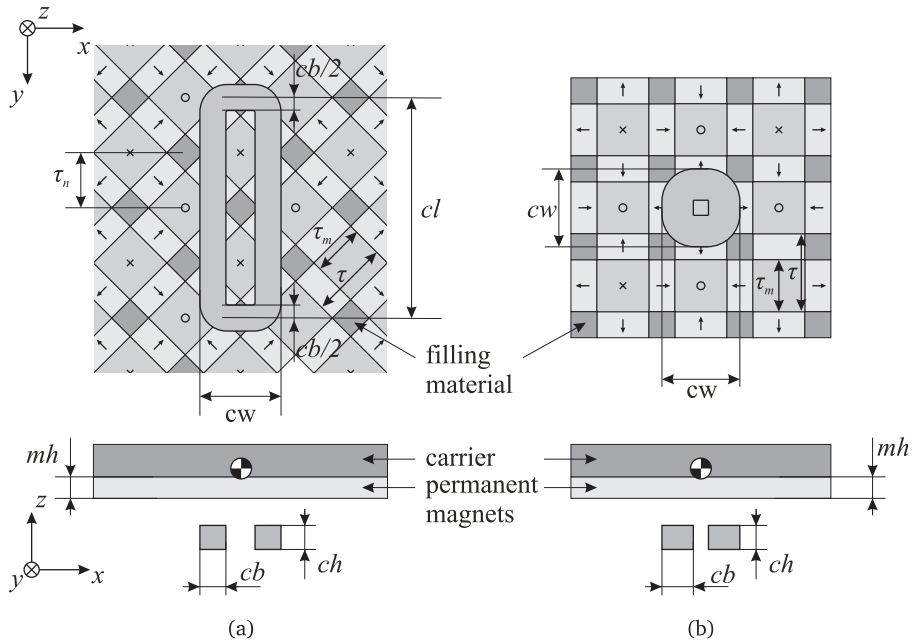
Figure 5.1. *Optimization variables and parameters: a) Rectangular coil, b) square coil.*

Table 5.2. *Optimization variables*

Variable	Symbol	Unit
Coil height	ch	m
Conductor bundle width	cb	m
Ratio of the magnet pitch and the pole pitch	τ_m/τ	-
Magnet height	mh	m

Table 5.3. *Optimization parameters*

Parameter	Symbol	Unit
Pole pitch	τ	m
Coil length	cl	m
Maximum coil width	cw	m
Mass carrier	m_c	kg
Mass density of permanent magnets	ρ_m	kg/m^3
Mass density of filling material	ρ_f	kg/m^3
Remanence of permanent magnets	B_r	T
Relative permeability of permanent magnets	μ_r	-

$f\left(ch, cb, \frac{\tau_m}{\tau}, mh\right)$ is equal to

$$f\left(ch, cb, \frac{\tau_m}{\tau}, mh\right) = \left(\frac{m\,g\,i}{F_z}\right)^2 R, \tag{5.2}$$

where m is the translator mass (including the magnets) and g is the acceleration due to gravity. The optimization variables are subject to the following inequality constraints

$$ch > 0, \tag{5.3}$$

$$0 < cb < \frac{cw}{2}, \tag{5.4}$$

$$0 < \frac{\tau_m}{\tau} < 1, \tag{5.5}$$

$$mh > 0. \tag{5.6}$$

The optimization of (5.2) has been carried out with a multi-variable optimization function in Matlab, which uses a sequential quadratic programming (SQP) routine [3]. The levitation force is calculated using the harmonic model (section 3.5). Only the first harmonic of the magnetic flux density distribution is considered in the optimization. Consequently, the results of the optimization will not change

if, for example, the length of the force vector, $|F|$, would have been taken into account in the objective function instead of the levitation force F_z. Because the force produced by the coil is proportional to the amplitude of the magnetic flux density of the magnet array, the magnet and coil dimensions can be optimized in separate optimizations, i.e. by maximization of the magnetic flux density per unit of translator mass

$$f_m \left(\frac{\tau_m}{\tau}, mh \right) = \frac{\hat{B}}{m},$$ (5.7)

and the maximization of

$$f_c \left(ch, cb \right) = \frac{|\vec{F}|^2}{i^2 R},$$ (5.8)

which is also referred to as the steepness of a motor [12].

   In the derivation of the harmonic model, the method of separation of variables is used. Under the following conditions, the optimization variables are not correlated in the objective function when the force is calculated with the harmonic model:

   • The ratio of the sizes of the magnets in the Halbach array τ_m/τ does not influence the mass of translator, i.e. $\rho_f = \rho_m$,
   • The influence of the thickness of the conductor bundle on the length of the turns is negligible, i.e. $cl \gg cb$,
   • The relative permeability of the permanent magnets $\mu_r = 1$.

In that case the objective function can be simplified to a multiplication of four independent functions

$$f \left(ch, cb, \frac{\tau_m}{\tau}, mh \right) = f_1 \left(ch \right) f_2 \left(cb \right) f_3 \left(\frac{\tau_m}{\tau} \right) f_4 \left(mh \right),$$ (5.9)

which are all positive, continuous and differentiable in the domain defined in (5.3)-(5.6). According to lemma 5.1, the multi-variable optimization problem can be obtained by solving four single-variable optimizations. The results of the single-variable optimization procedure can serve as design rules for the planar actuator and are listed in Table 5.4. The coil height ch is only a function of the pole pitch τ. The conductor bundle width cb is a function of $\frac{cw}{\tau_n}$. No rule can be given for the magnet height mh because it cannot be optimized without the knowledge of the materials and the dimensions of the translator.

Lemma 5.1. *Let a continuous and differentiable function*

$$f(x_i, x_2, \ldots, x_n) = \prod_{i=1}^{n} f_i \left(x_i \right),$$ (5.10)

Table 5.4. *Result of the single-variable optimization.*

Optimization variable	Assumptions	Optimal value
ch	none	0.283τ
$cb\left(cw = \frac{4}{3}\tau_n\right)$	$cl \gg cb$	$0.527\tau_n$
$cb\left(cw = \frac{3}{2}\tau_n\right)$	$cl \gg cb$	$0.612\tau_n$
τ_m/τ	$\rho_f = \rho_m$ and $\mu_r = 1$	0.696

and suppose the following conditions hold

$$0 < \min_{a_i \leq x_i \leq b_i} f_i\left(x_i\right) \leq f_i(x_i), \tag{5.11}$$

then

$$f(x_i, x_2, \ldots, x_n) \geq \prod_{i=1}^{n} \min f_i\left(x_i\right). \tag{5.12}$$

The deviations between the results obtained by the single-variable optimization and the multi-variable optimization are related to the extra constraints of the single-variable optimization. This is illustrated in Figures 5.2a and b. Figure 5.2a shows the optimal relative conductor bundle width as function of the relative coil width for a coil with a coil length of $cl = 4\tau_n$ and for a coil with $cl \gg cb$. The relative conductor bundle saturates for coils with a full-pitch winding $cw > 1.8\tau_n$. In Figure 5.2b, the optimal height mh of a magnet array (121 poles, $\tau = 25$ mm, $\rho_m = 7700$ kg/m^3, $B_r = 1.24$ T, $\mu_r = 1.03$) as function of the mass of the carrier m_c, to which the magnets are glued, is shown. The magnetic flux density levels near the coils and, consequently, the force produced by the coils is a function of the magnet height (3.56). Because the power dissipation to levitate the translator is minimized, the optimal magnet height mh and, hence, the magnet mass is a function of the mass of the carrier m_c. As expected, the optimal magnet height increases for a larger carrier mass m_c.

Figure 5.3 compares the power dissipation in a coil ($cw = \frac{3}{2}\tau_n$, $cl = 4\tau_n$) due to levitation of a carrier with $m_c = 4$ kg and three different magnet arrays, i.e. a Halbach array with $\rho_f = 0$ kg/m^3, a Halbach array with $\rho_f = 7700$ kg/m^3 and a NS

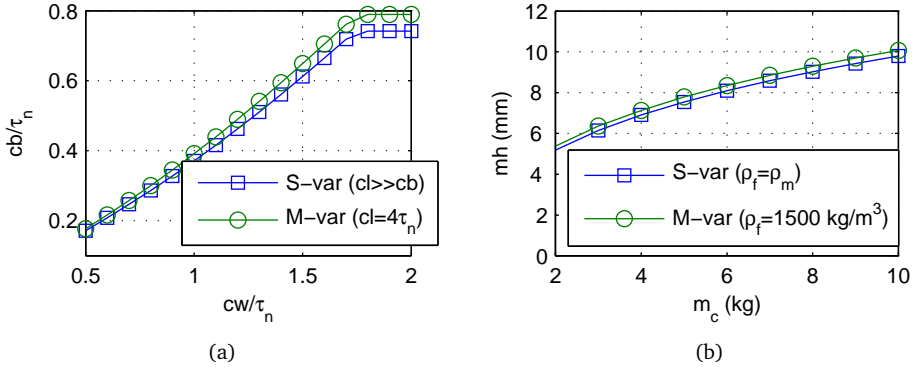(a)   (b)

Figure 5.2. *Single-variable (S-var) and multi-variable (M-var) optimization of a) a rectangular coil with $cl = 4\tau_n$ and b) a Halbach permanent-magnet array with 11x11 poles, $\tau = 25$ mm, $\rho_m = 7700$ kg/m³, $B_r = 1.24$ T, $\mu_r = 1.03$.*

array (with only in the z-direction magnetized magnets, see also Figure 2.2) with $\rho_f = 0$ kg/m³. Because the magnet array is levitated by only one coil the power dissipation is large. In reality, the levitation force is produced by more coils and the power dissipation decreases in proportion to the number of coils. Figure 5.3 shows that the optimal ratio of the sizes of the magnets in the magnet array $\frac{\tau_m}{\tau}$ depends on the mass density of the filling material. The figure demonstrates also that the actuator with a NS-array (a magnet array with only in the z-direction magnetized magnets, see also Figure 2.2) has a significantly larger power dissipation.

Figure 5.4 shows an analysis of the magnetic flux density per unit of translator mass (5.7) for different values of the carrier mass m_c (i.e. the mass of the translator without the magnets or back-iron) and three different magnet arrays with a pole pitch of $\tau = 25$ mm. The figure shows that except for a planar actuator with an extremely low carrier mass, in this case $m_c < 0.3$ kg, a planar actuator with a NS-array will have a higher power dissipation than a planar actuator with a Halbach array. This figure also illustrates that the increased magnetic flux density of a NS-magnet array with back-iron does not necessarily compensate for the additional iron mass.

In rotary machines, different combinations of slots-per-pole-per-phase are usually compared. For planar actuators without slots and without multi-phase excitation, it makes more sense to compare the power dissipation for different combina-
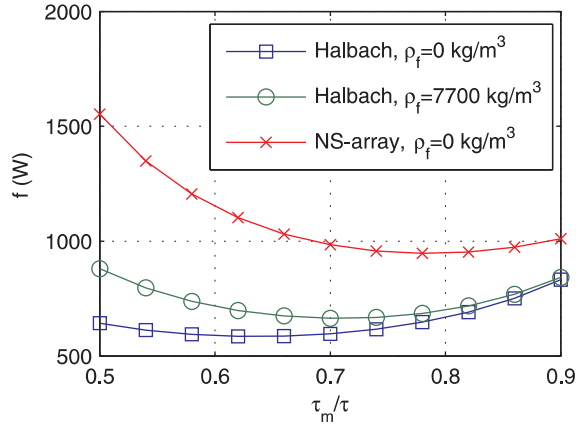
Figure 5.3. *Power dissipated for levitation of the translator with a single coil ($\tau = 25$ mm, $cl = 4\tau_n$, $cw = \frac{3}{2}\tau_n$, $m_c = 4$ kg, $\rho_m = 7700$ kg/m³, $B_r = 1.24$ T, $\mu_r = 1.03$ and 121 (11x11) poles in the magnet array). For the NS-array: $\rho_f = 0$ kg/m³.*

Figure 5.4. *Comparison of $\hat{B}/m$ for different values of the carrier mass m_c and three different magnet arrays ($\tau =25$ mm, $\rho_m = 7700$ kg/m³, $B_r = 1.24$ T, $\mu_r = 1.03$ and 121 (11x11) poles in the magnet array, $\rho_f = 1500$ kg/m³ for the Halbach array only).*

Figure 5.5. *Normalized performance of different combinations of coils per pole.*

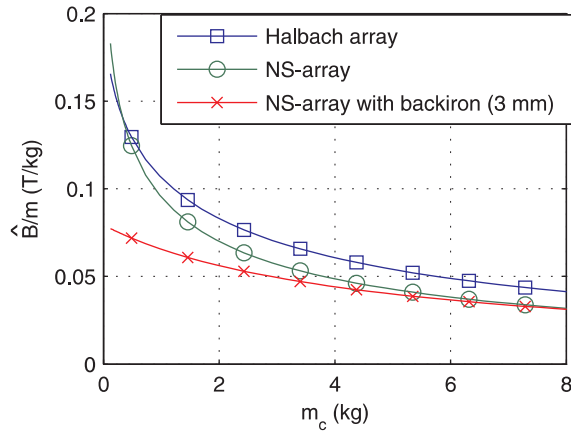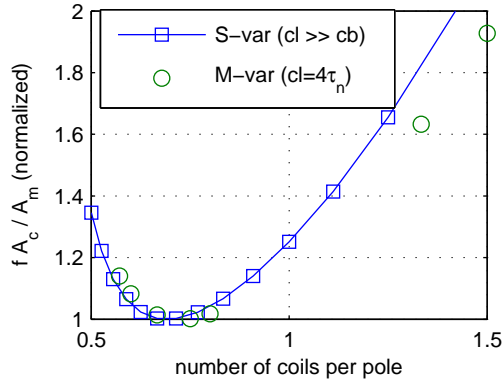tions of coils-per-pole. The power dissipation of different coils cannot be compared without considering the sizes of the coil itself, because only a limited number of coils can be located below the magnet array and contribute to the force and torque production. To investigate the different coil-per-pole combinations, the effectiveness of a coil is calculated by

$$\frac{f\left(ch, cb, \frac{\tau_m}{\tau}, mh\right) A_c}{A_m},\tag{5.13}$$

where is the horizontal area of the coil ($A_c = (cl + cb) \cdot cw$ for a rectangular coil and $A_c = cw^2$ for a square coil) and A_m is the horizontal area of the magnet array. In this way, an estimation of the total power dissipation of a full planar actuator design for levitation of the magnet array is given. This estimation does not take into account the force distribution or the switching between coil sets. Figure 5.5 shows the normalized results obtained for a rectangular coil with $cl = 4\tau_n$ and the results obtained from the single variable optimization of cb ($cl \gg cb$). The lowest power dissipation in the planar actuator is obtained for coil-per-pole combinations in between 0.62 and 0.78. For that reason, only coils distributed according to a three-phase system with 3 coils per 4 poles ($cw = \frac{4}{3}\tau_n$) and coils distributed according to a semi-four-phase system with 3 coils per two poles ($cw = \frac{3}{2}\tau_n$) are considered in section 5.4.

5.3   Synthesis considerations

Although the analysis of a single coil and a magnet array gives insight in the properties of planar actuators, their final characteristics can only be determined by analyzing full planar actuator topologies. These topologies are defined by the magnet and coil distributions and the commutation and switching algorithm. The synthesis involves a number of considerations.

5.3.1   Controllability

The most important requirement of a synthesized planar actuator design is that it is controllable. At least six individually controlled coils are required to control the six degrees-of-freedom of the planar actuator. An example of such a minimum planar actuator design is shown in Figure 5.6a. The actuator consists of three groups of two coils (A, B and C). It can be shown that, applying $dq0$-decomposition (see also section 4.1), each group can produce a levitation force, and a force in the xy-plane, independent of the position of the magnet array, when the coils in each group are displaced $\frac{3}{2}\tau_n$. The direction of the force in the xy-plane depends on the orientation of the coils. The force vectors produced by each coil group are drawn in the coil groups in Figure 5.6a. Because the coil groups are positioned in a triangle, all six degrees-of-freedom can be accessed, which can be verified by the calculation of the condition number (see section 4.4).

The performance in terms of the power dissipation of this actuator can be improved by adding another six coils, which are rotated 180 mechanical degrees. This 12-coil actuator is shown in Figure 5.6b. The coils of this planar actuator are arranged in a herringbone pattern. Although the currents in the coils are individually controlled, each column of coils forms a four-phase system.

The controllability of magnetically levitated planar actuators is extensively discussed in [73].

5.3.2   Switching between different coil sets

The commutation algorithm of the planar actuator (see section 4.3) actively switches coils on and off. The number of active coils is position dependent. Hence, the power dissipation varies, since the same wrench should be produced by a different number of coils. The variation of the power dissipation can be kept small when only a small percentage of the active coils is switched. Consequently, this tends towards planar actuators with a large number of active coils when this commutation algorithm is applied.
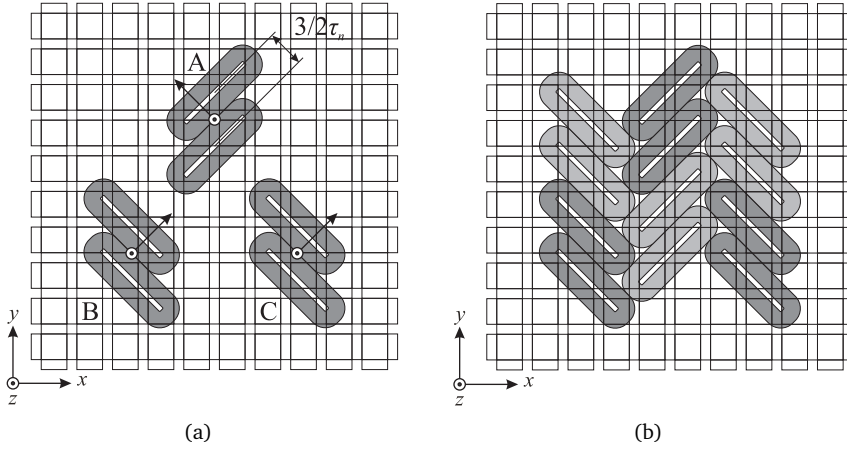
Figure 5.6. *Planar actuators designs with coils arranged in a herringbone pattern: a) Planar actuator with six coils, b) planar actuator with 12 coils. The indication of the magnetization of the magnets in the Halbach magnet array is omitted for simplification.*

5.3.3 Arrangement of the coils

There are various possibilities to arrange the coils in planar actuators. The coils in the topology with square coils (Figure 2.8 and Figure 4.10) and the coils arranged in a herringbone pattern (Figure 5.6b) occupy the full stator. In the inverted planar actuator (Figure 2.9), there is a spacing between the three-phase coil groups and, consequently, the stator area is not fully utilized for the power conversion.

The two planar actuators discussed in section 2.4 all have one layer of coils in the z-direction. In [4] also embodiments of planar actuators can be found with multiple layers of short coils in the z-direction. The disadvantage of multiple coil layers is that the magnetic flux density distribution (3.55) and, as a result, the force in the planar actuator, and is proportional to an exponential function

$$\vec{F} \propto e^{-\frac{\pi p_z}{\tau_n}}. \tag{5.14}$$

Hence, the ohmic losses in the coils located further from the magnet array are higher for the production of the same force and cooling is complicated due to required insulating materials between the coils. Therefore, these multi-layer arrangements are not considered in this thesis.

5.3.4   End-effects of the magnet array

Long-stroke motion of the planar actuator is realized by switching among different coil sets. As the end-effects of the magnet array are not included in the model of the direct current-wrench decoupling, coils are actively switched on and off near the edges of the magnet array to prevent force and torque ripples. To determine the area in which the coils are affected by the end-effects of the magnet array, the magnetic flux density distribution $|B|$ of a magnet array has been predicted by both the surface charge model (which includes the edge-effects) and the harmonic model (which assumes an infinitely long magnet array). In Figure 5.7 the difference between the two models for a Halbach magnet array is shown. The figure indicates that the force and torque, produced by coils of which a part is located below the outer rectangular magnets, are influenced by the edge-effects of the magnet array.

When a coil is switched off, the part of the magnet array above that coil is not used anymore for the power conversion. Consequently, it is favorable to apply short coils, i.e. square coils or rectangular coils with a limited coil length, cl, to planar actuators in combination with this commutation algorithm.

5.4   Comparison of four planar actuators

Based on the results of the analysis of a single coil and a magnet array (see section 5.2) and the considerations discussed in section 5.3, four planar actuators are synthesized. All actuators have a square translator of 300 by 300 mm and a square magnet array. Contrary to, for example, the inverted planar actuator (Figure 2.9), the planar actuators compared in this thesis are not constructed of separated multi-phase coil groups. Because the coils are switched during the movements of the translator in the xy-plane, these separated groups fall apart. Therefore, the coils in the compared actuators are laid in unbroken multi-phase rows of which the outer coils are switched. This can be realized by arranging rectangular coils in the in thesis proposed herringbone pattern or by using square coils.

The sizes of the coils and the magnets in the four compared planar actuators are calculated with a multi-variable optimization as described in section 5.2. The parameters used in the optimization are listed in Table 5.5. If the coils and magnet sizes would have been obtained from the design rules listed in Table 5.4 and a separate optimization of (5.7) to calculate the magnet height mh, the power dissipation of the four actuator would have been less than 2% higher.

The pole pitch of the magnet array is chosen as large as possible for a given coil distribution. Because of (5.14), actuators with a larger pole pitch have less variation in the force when the clearance between magnets and coils is changed.
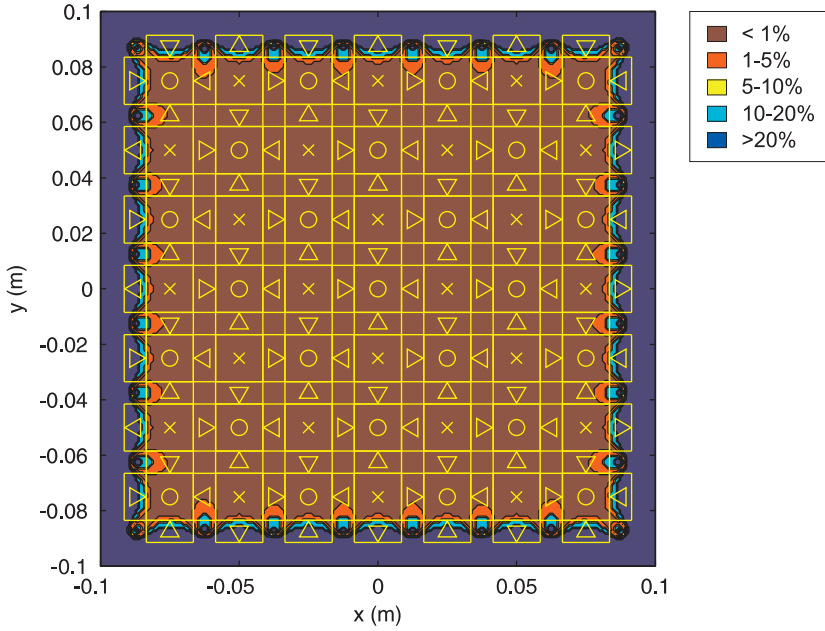
Figure 5.7. *Difference between the predictions of $|B|$ by the harmonic model (15 harmonics included in the analysis) and the surface charge model 4 mm below the magnet array ($\tau = 25$ mm, $\frac{\tau_m}{\tau} = 0.68$, $mh = 7$ mm). The figure shows the bottom view of the magnet array.*

Because of the analysis results in section 5.2, all actuators have a Halbach magnet array and a coil width of either $cw = \frac{4}{3}\tau_n$ or $cw = \frac{3}{2}\tau_n$. In case of the square coils, the coil width is equal to $cw = \frac{3}{2}\tau$. Conservatism is exercised in the design as it is assured that the coil is either completely switched off or at least severely penalized before a part of the coil is near the edges of the magnet array.

Topology 1 is shown in Figure 5.8. The coils ($cl = 4\tau_n$ and $cw = \frac{4}{3}\tau_n$) are arranged in a herringbone pattern. The coils in each of the seven columns are distributed according to a three-phase system. The rectangular coils in each column are displaced over the distance

$$\tau_{cy} = \sqrt{2}cw. \tag{5.15}$$

Table 5.5. *Optimization parameters*

Parameter	Value	Unit
Mass of carrier (without magnets), m_c	4.0	kg
Mass density of permanent magnets, ρ_m	7700	kg/m^3
Mass density of filling material, ρ_f	1500	kg/m^3
Remanence of permanent magnets, B_r	1.24	T
Relative permeability of permanent magnets, μ_r	1.03	-

The columns are displaced over a distance

$$\tau_{cx} = \frac{cl + cb}{\sqrt{2}}. \tag{5.16}$$

The actuator has in between 15 and 24 active coils. The weighting functions $\mathbf{\Delta_x}(p_x)$ and $\mathbf{\Delta_y}(p_y)$ are indicated and defined in Figure 5.8. The coils are switched with raised cosine functions which have a width of $\frac{1}{2}\tau_{cx}$ and $\frac{1}{2}\tau_{cy}$, respectively. Figure 5.8 shows the active coils for the drawn position of the magnet array. The not penalized coils are colored green, and the penalized coils are colored yellow. This actuator has 28 different sets of active coils. The switching boundaries of these sets are indicated in Figure 5.9.

Figure 5.10 shows the set of active coils (in dark gray) at the boundaries of state 17. The positions of the mass center point at these boundaries are indicated in Figure 5.11. In Figure 5.10c, all 24 coils are active and none of them is penalized. At the transition between states 17 and 24 (Figure 5.10d), the left column of coils is switched off and only 18 coils are active. Figure 5.10a shows the active coils at the transition between states 16 and 17. Despite the fact that the top row of active coils have a different distance to the edge of the magnet array, they have the same weighting factor and are simultaneously switched off. In the worst case situation (crossing of states 16, 17, 23 and 24), nine coils are penalized by the weighting functions and are switched off (Figure 5.10b).

The coils of topologies 2 and 3 are also arranged in a herringbone pattern. These topologies are shown in Figure 5.12 and Figure 5.13. The coil pitches τ_{cx} and τ_{cy} are defined according to (5.15) and (5.16), respectively, and are indicated
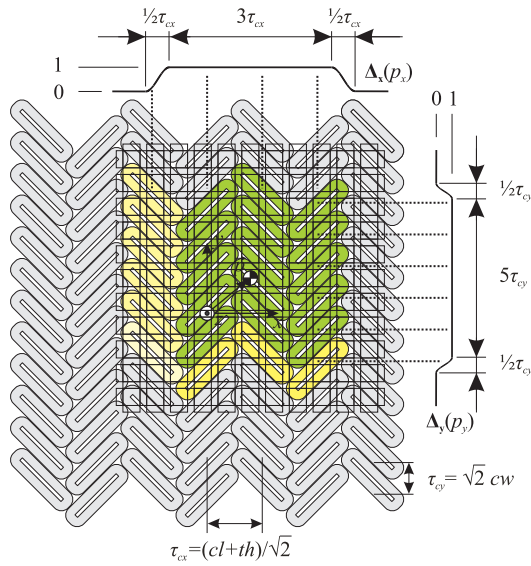
Figure 5.8. *Topology 1: 15-24 active coils, $cw = \frac{4}{3}\tau_n$, $cl = 4\tau_n + cb$.*
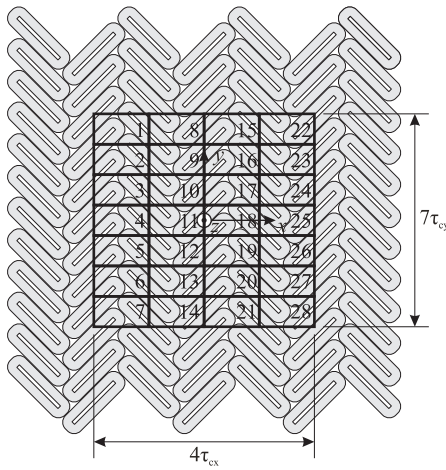
Figure 5.9. *Allowed positions of the mass center point of the translator of topology 1. The stroke is subdivided into 28 states.*

(a)   (b)

(c)   (d)
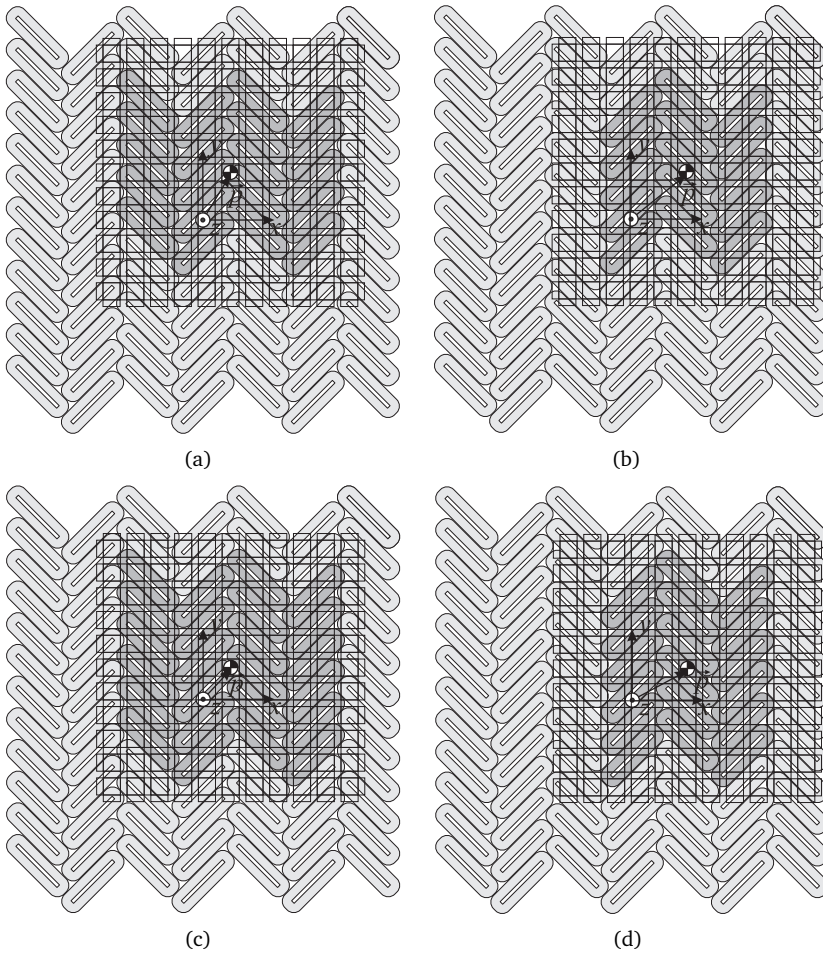
Figure 5.10. *Active coils of topology 1 at the transitions between different sets of coils.*

in the figures. The dark gray coils are active at the indicated position of the magnet array. The coils of topology 2 ($cl = 4\tau_n$) are distributed according to a semi-four-
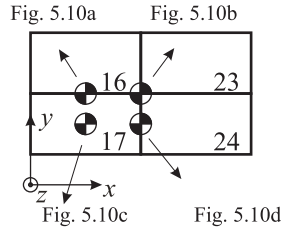
Figure 5.11. *Positions of the mass center point of the magnet array at the transitions between different coil sets for which the set of active coils are shown in Figure 5.10.*

phase system $cw = \frac{3}{2}\tau_n$. Topology 2 has the same coil arrangement as shown in Figure 5.6b. An extra row and column of active coils is added to allow for switching between different coil sets. The coils of topology 3, which are the shortest possible rectangular coils ($cl = 2\tau_n$), are distributed according to a three-phase system $cw = \frac{4}{3}\tau_n$. The disadvantage of using these small coils is that more coils on the stator are needed to obtain the same stroke. Topologies 1 and 2 have a magnet array with 11x11 poles. Topology 3 requires only 10x10 poles. Therefore, the pole pitch of topology 3 is 10% larger. Topologies 2 and 3 use a switching strategy similar to topology 1 (Figure 5.10).

The fourth topology (Figure 5.14) is a planar actuator with square coils. The coils are distributed according to a semi-four-phase system ($cw = \frac{3}{2}\tau$). The weighting functions are implemented as indicated in Figure 4.8. This topology has the least magnets in the magnet array and, as a result, the largest pole pitch ($\tau = 30.4$ mm).

Details of the four topologies are summarized in Table 5.6, that demonstrates that the optimal magnet height, mh, increases for larger values of the pole pitch. Therefore, the translator mass of topologies 3 and 4 is larger than that of topologies 1 and 2. To predict the performance of the different planar actuators in terms of the power dissipation and the force and torque ripples, the commutation algorithm is coupled with the harmonic model (section 3.5). Up to the $k = l = 9^{th}$ harmonic is included in the simulations. Because the weighting matrix $\mathbf{\Delta}(p_x, p_y)$ switches coils off before the force and torque are significantly influenced by the end-effects of the magnet array, the use of the harmonic model, which assumes an infinitely large magnet array, does not result in significant errors in the predictions.

The evaluation of the planar actuators in its full reachable volume over its full wrench is very computational demanding. Therefore, the power dissipation and the

Figure 5.12. *Topology 2: 12-20 active coils, $cw = \frac{3}{2}\tau_n$, $cl = 4\tau_n$.*

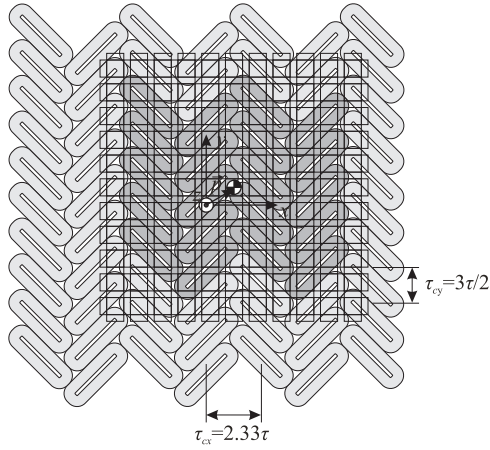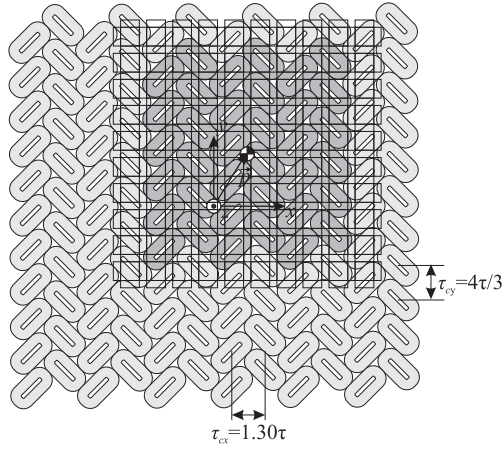**Figure 5.13.** *Topology 3: 25-36 active coils, $cw = \frac{4}{3}\tau_n$, $cl = 2\tau_n$.*
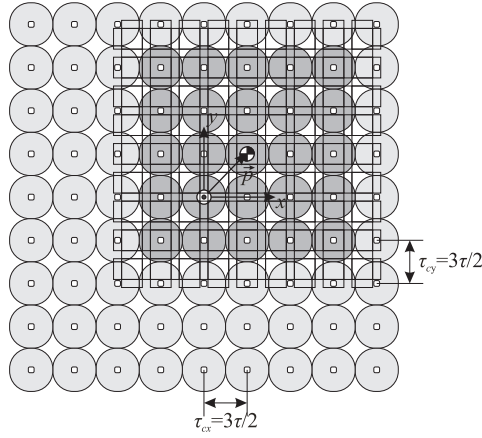
Figure 5.14. *Topology 4: 16-25 active coils, $cw = \frac{3}{2}\tau$.*

force and torque ripples have been predicted for two static loads. The first load is the levitation of the translator

$$\vec{w} = \begin{bmatrix} F_x & F_y & F_z & T_x & T_y & T_z \end{bmatrix}^{\mathsf{T}} = \begin{bmatrix} 0 & 0 & mg & 0 & 0 & 0 \end{bmatrix}^{\mathsf{T}}. \quad (5.17)$$

This load gives an indication of the minimal power dissipation. An indication of the maximum power dissipation is obtained by the second load, levitation and maximum acceleration (10 m/s^2) of the translator in the xy-plane, i.e.

$$\vec{w} = \begin{bmatrix} 10m & 10m & mg & 0 & 0 & 0 \end{bmatrix}^{\mathsf{T}}. \quad (5.18)$$

The mechanical clearance between stator and translator is equal to 1 mm. The results of these simulations are also listed in Table 5.6.

Although all designs are based on the same starting points, there are large differences between them. The mean power dissipation for levitation of the translator of topology 4 with the square coils is 39 % larger than that of topology 1 with the rectangular coils. The variation in power dissipation of each topology is caused by the switching between different sets of active coils. This is illustrated in Figure 5.15, which shows the power dissipation of topology 1 as function of the p_x- and p_y-positions of the translator. The difference between the minimum and maximum power dissipation is the smallest for the topology 3 with the most active

Table 5.6. *Comparison of four planar actuator topologies*

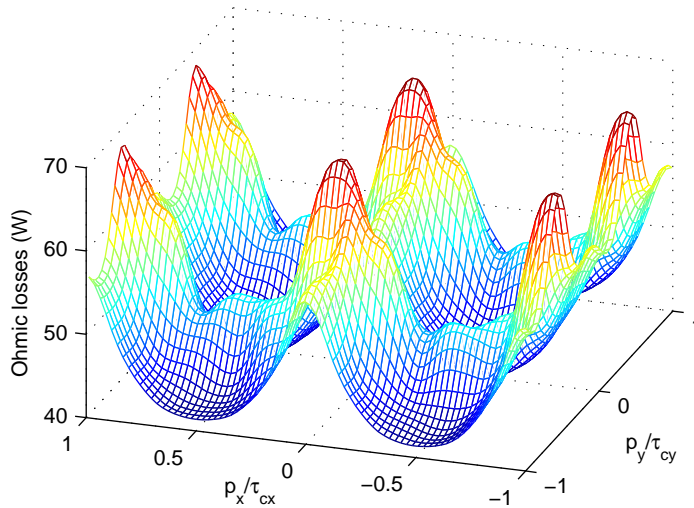| Topology	1	2	3	4
maximum number of active coils (xy)	4x6	4x5	6x6	5x5
magnetic poles (xy)	11x11	11x11	10x10	9x9
pole pitch magnet array, τ (mm)	25.0	25.0	27.4	30.4
coil width, cw	$\frac{4}{3}\tau_n$	$\frac{3}{2}\tau_n$	$\frac{4}{3}\tau_n$	$\frac{3}{2}\tau$
coil length, cl	$4\tau_n$	$4\tau_n$	$2\tau_n$	$\frac{3}{2}\tau$
Sizes obtained from optimization of single coil and magnet array				
coil height, ch	0.28τ	0.28τ	0.28τ	0.28τ
width of conductor bundle, cb	$0.56\tau_n$	$0.65\tau_n$	$0.59\tau_n$	0.65τ
magnet size ratio, $\frac{\tau_m}{\tau}$	0.66	0.66	0.66	0.66
magnet height, mh (mm)	7.1	7.1	7.6	8.0
mass translator, m (kg)	7.95	7.95	8.17	8.44
clearance or airgap (mm)	1.0	1.0	1.0	1.0
Levitation only: $\vec{F} = [0 \ \ 0 \ \ mg]^{\mathsf{T}}$ (N), $\vec{T} = \vec{0}$ (Nm)				
Ohmic losses mean (W)	50.0	54.0	56.8	69.3
Ohmic losses min (W)	41.4	40.1	49.3	36.1
Ohmic losses max (W)	69.0	80.1	73.4	100
F_x rms ripple (N)	0.049	0.057	0.116	0.757
F_y rms ripple (N)	0.076	0.096	0.120	0.757
F_z rms ripple (N)	0.080	0.079	0.182	1.143
T_x rms ripple (Nm)	0.015	0.009	0.013	0.024
T_y rms ripple (Nm)	0.014	0.015	0.010	0.024
T_z rms ripple (Nm)	0.011	0.011	0.013	0.001
Acceleration and levitation: $\vec{F} = [10m \ \ 10m \ \ mg]^{\mathsf{T}}$ (N), $\vec{T} = \vec{0}$ (Nm)				
Ohmic losses mean (W)	278	302	303	347
Ohmic losses min (W)	217	211	258	223
Ohmic losses max (W)	588	627	443	460
F_x rms ripple (N)	0.106	0.146	0.191	1.189
F_y rms ripple (N)	0.218	0.298	0.183	1.189
F_z rms ripple (N)	0.157	0.251	0.247	1.679
T_x rms ripple (Nm)	0.029	0.027	0.022	0.061
T_y rms ripple (Nm)	0.030	0.027	0.025	0.061
T_z rms ripple (Nm)	0.028	0.026	0.024	0.014

Figure 5.15. *Predicted ohmic losses of topology 1 as function of the p_x- and p_y-positions during levitation of the translator.*

coils. In this topology 11 of the 36 coils (31%) are switched off at the worst case transition between different coil sets. The thermal issues are further discussed in section 6.4.

The force and torque ripples in the planar actuators are small in the three topologies with rectangular coils (topologies 1, 2 and 3). Hence, the use of the simple analytical model (see section 3.6) in the commutation algorithm is satisfactory. The rms-force ripples in these topologies are less than 0.4% during levitation and acceleration. Topology 4 suffers from large force ripples up to 1.4%. Using the harmonic model, two causes of the ripples can be investigated: the influence of higher harmonics in the magnetic flux density distribution and the accuracy of the analytical model. The force and torque ripples have been predicted for every harmonic (up to $k = l = 5$) separately and for different values of the ratio of the sizes of the permanent magnets in the magnet array τ_m/τ. By varying this ratio, the spectrum of the magnetic flux density distribution is changed.

Typical results of this analysis for actuators with rectangular coils and with
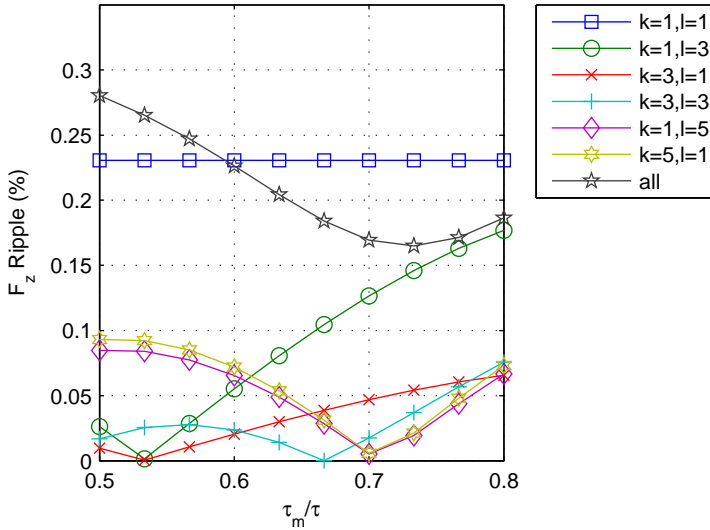
Figure 5.16. *Harmonic force ripple components in F_z of topology 1 versus $\frac{\tau_m}{\tau}$ ($\vec{F} = [10m \ 10m \ mg]^{\mathsf{T}}$ (N), $\vec{T} = \vec{0}$ (Nm)).*

square coils are shown in Figures 5.16 and 5.17. The ripples are predicted for the second load. The levitation force ripple of topology 1, which is shown in Figure 5.16, is dominated by the ripple produced by the first harmonic itself. The cause of this ripple is that the analytical model in the commutation algorithm assumes that the x- and y-directions are fully decoupled. In reality, there is a small unmodeled cross-coupling of the force components in the x- and y-directions of approximately 1% (see section 7.3). This cross-coupling is caused by the round shape of the corners of the coils. The force ripples of topology 4 (Figure 5.17) are only produced by the higher harmonics of the magnetic flux density distribution. The ripples are dominated by the $k = 1, l = 3$ and the $k = 3, l = 1$ harmonics. These ripples can either be reduced by including these harmonics in the analytical model in the commutation algorithm or by changing τ_m/τ to 0.53. If $\tau_m/\tau = 0.53$, these harmonics do not occur in the magnetic flux density spectrum. However, such a change in the magnet array increases the mean power dissipation for levitation of the translator from 69 W to 76 W.
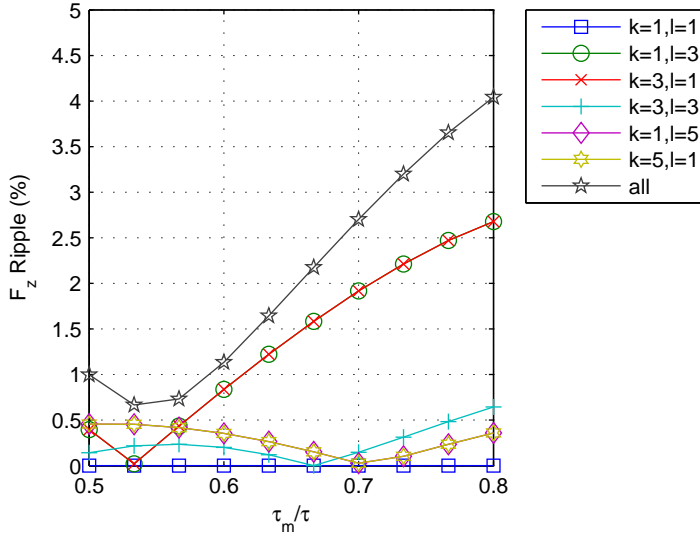
Figure 5.17. *Harmonic force ripple components in F_z of topology 4 versus $\frac{\tau_m}{\tau}$ ($\vec{F} = [10m \;\; 10m \;\; mg]^{\mathsf{T}}$ (N), $\vec{T} = \vec{0}$ (Nm)).*

Because of the low power dissipation and the low force and torque ripples topology 1 is selected and manufactured. This actuator will be further referred to as the herringbone pattern planar actuator (HPPA).

5.5 Conclusions

In this chapter a method for the synthesis and optimization of planar actuators is presented. The planar actuator is assumed to be constructed of independent Lorentz actuators in order to optimize the coil and magnet dimensions and minimize the power dissipation of the actuator. The results of this analysis are used to compare a limited number of planar actuators. The design of the planar actuator is influenced by both the chosen commutation algorithm and the demand of a square permanent-magnet array. Simulations of the topologies show that planar actuators with coils arranged in a herringbone pattern combine both a low power dissipation and low force and torque ripples. The ripples in these actuators are dominated

by unmodeled cross-coupling of the force production in the xy-plane. The topology with the square coils has both a larger power dissipation and higher force and torque ripples than the topologies with rectangular coils. The higher ripples are caused by higher harmonics in the magnetic flux density spectrum. Because of the low power dissipation and low force and torque ripples, topology 1 with 15-24 active coils in a herringbone arrangement with $cw = \frac{4}{3}\tau_n$ and $cl = 4\tau_n$ is selected for manufacturing.

The optimization and synthesis of the planar actuator topologies are for the greater part carried out manually. This process can be automated to analyze more different planar actuator configurations and can possibly be coupled with an optimization algorithm to find optimal topologies.

Chapter 6

Design aspects of the moving-magnet planar actuator

In the previous chapter, four planar actuator topologies have been designed and compared. Based on the prediction of the power dissipation and force and torque ripples, one of the planar actuators has been selected and has been manufactured. During the design process a number of issues, such as demagnetization of the permanent magnets, eddy-current damping, selection of the power amplifiers, the number of turns of the coils, temperature rise, etc. has been neglected. In this chapter, these issues are discussed.

6.1 Final design

The final design of the herringbone pattern planar actuator (HPPA) (topology 1 from section 5.4) is shown in Figure 6.1. The dimensions and properties are indicated in the drawing and listed in Table 6.1. The coil dimensions listed in Table 5.6 are adapted in order to create sufficient mechanical spacing between the coils. Figure 6.2 shows a photo of the HPPA. The planar actuator has 84 coils. The coils have a orthocyclic winding [50]. Although only 24 coils are used simultaneously, each coil is connected to a separate single-phase power amplifier to provide maximum freedom during the experiments. The coils are cast with an epoxy resin. They are mounted on top of a water/glycol cooled aluminum plate. The permanent magnets are glued to an aluminum carrier with an estimated lowest resonance frequency of 785 Hz. The carrier consists of two parts. The magnets has been glued first to a 5 mm thick aluminum plate while an iron plate was placed behind the aluminum. By this method, the magnets are attracted to the iron and pressed against the alu-
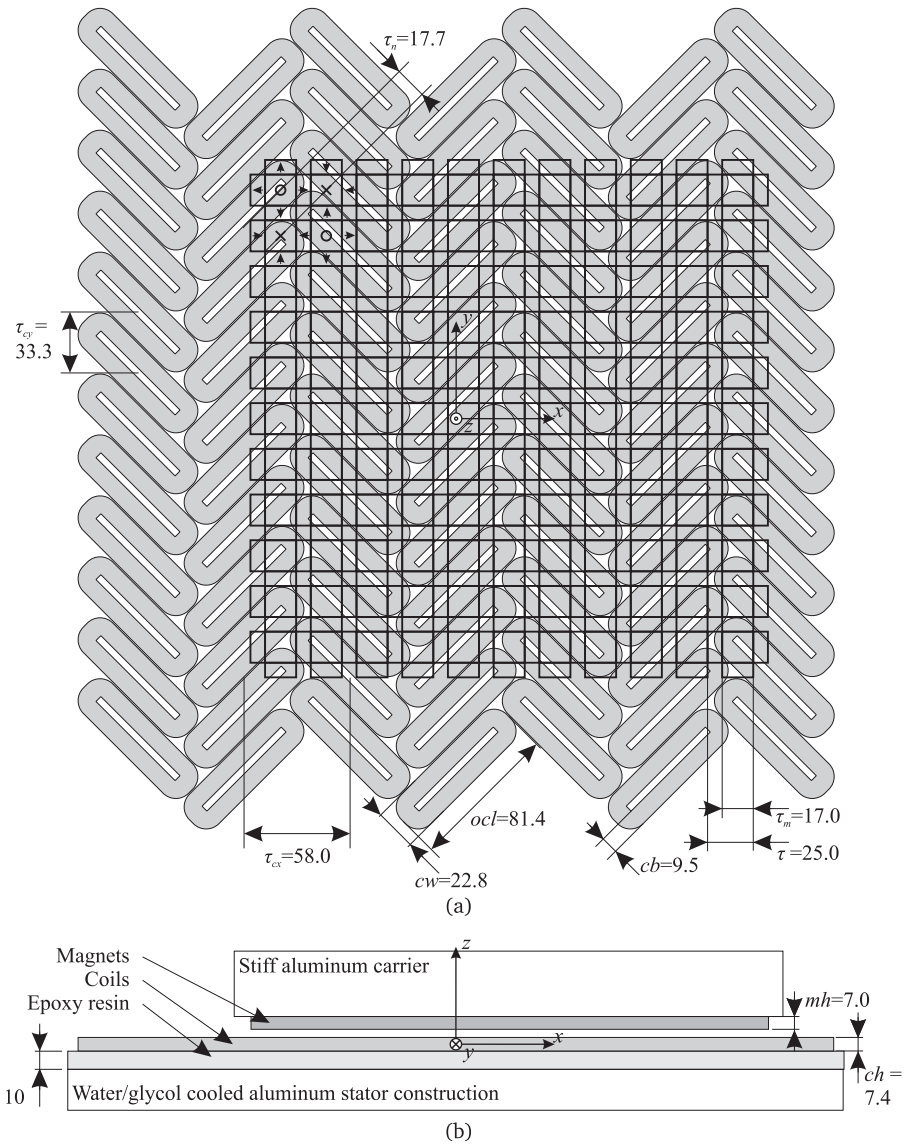
Figure 6.1. *Herringbone pattern planar actuator: a) Top view, b) side view (sizes in mm).*

Table 6.1. *Dimensions and properties of the HPPA*

Parameter	Value	Unit
maximum number of active coils (xy)	24 (4x6)	-
total number of coils (xy)	84 (7x12)	-
magnetic poles (xy)	121 (11x11)	-
translator size (xy)	300x300	mm
stroke (xy)	232x233	mm
clearance (z-direction)	1 - 2	mm
velocity (xy-plane)	1.0	m/s
acceleration (xy-plane)	10	m/s^2
jerk (xy-plane)	1000	m/s^3
pole pitch magnet array, τ	25.0	mm
pole pitch magnet array, τ_n	17.7	mm
magnet size ratio, τ_m/τ	0.68	-
magnet height, mh	7.0	mm
coil width, cw	22.8	mm
coil length, cl	$4\tau_n$	-
outer coil length, ocl	81.4	mm
coil pitch (x-direction), τ_{cx}	58	mm
coil pitch (y-direction), τ_{cy}	33.3	mm
coil height, ch	7.4	mm
conductor bundle width, cb	9.5	mm
number of turns	319	-
total mass translator, m	8.2	kg
mass carrier without magnets, m_c	4.28	kg
permanent-magnet material	VACODYM 655HR	
power amplifiers	PADC3AX52/6	
cooling medium	water/glycol	
epoxy resin	RenCast CW 5156-1	

X-leg H-drive
Measurement frame
Carrier
Permanent magnets
Coils
Epoxy resin
Water/glycol cooled aluminum stator construction
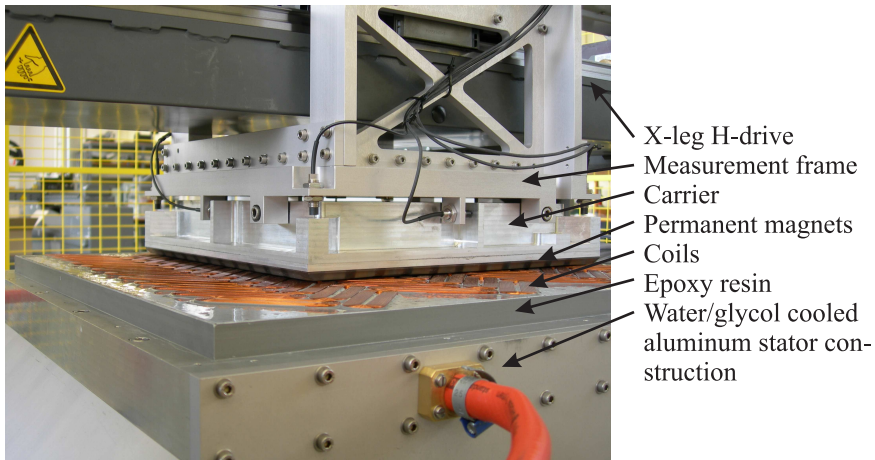
Figure 6.2. *Overview of the herringbone patern planar actuator.*

Stiff aluminum carrier

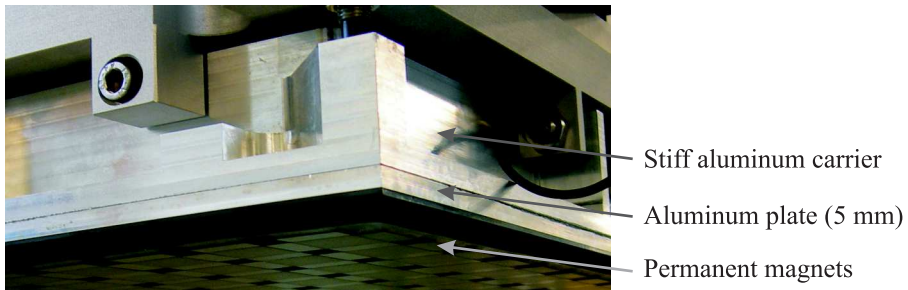Aluminum plate (5 mm)

Permanent magnets

Figure 6.3. *Construction of the translator consisting of three parts.*

minum. After the gluing of all the magnets, the iron has been removed and the plate with the magnets has been screwed and glued to the stiff part of the carrier. Figure 6.3, Figure 6.4 and Figure 6.5 show photos of the translator, the top side of the stiff aluminum carrier and the magnet array, respectively. The magnets are cast with an epoxy resin.

The design and manufacturing of the aluminum parts, and the assembling of

Figure 6.4. *Stiff aluminum carrier.*

Figure 6.5. *Magnet array.*
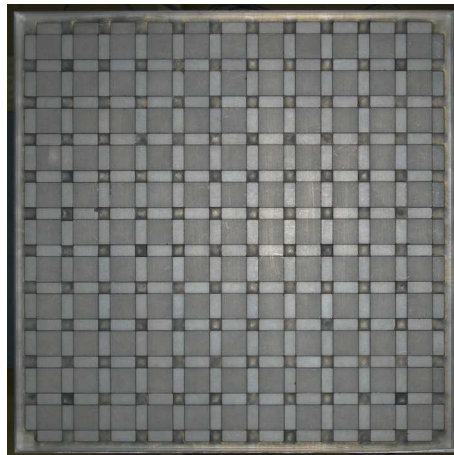
the planar actuator have been carried out by the workshop of the Eindhoven University of Technology, Gemeenschappelijke Technische Dienst (GTD). The coils have been manufactured by Tecnotion. The permanent magnets have been manufactured and glued by Vacuumschmelze. Prodrive has supplied the power amplifiers. More information on the materials and components can be found in Appendix C.

6.2   Working point of the permanent magnets

The force and torque produced in the planar actuator are proportional to the magnetic flux density of the permanent magnets in the coils. The magnetic flux density levels and, consequently, the force and torque per unit of current, can be increased by choosing a higher permanent-magnet grade. This can be done without the necessity to change the design, due to the absence of magnetic parts which could saturate.

In the analysis of the planar actuator with the harmonic model (see section 3.5), only the remanence, B_r, and the relative (recoil) permeability of the permanent magnets, μ_r, have been taken into account. It is assumed that each NdFeB permanent magnet operates above its knee-point, which is defined by the intrinsic coercivity value of the permanent magnet. If (a part of) a magnet operates below the knee-point, the permanent magnet is irreversibly demagnetized [23]. The operating point of the magnets in the Halbach magnet array is calculated using a finite element analysis in FLUX3D [8]. Figure 6.6 shows the operating points (the crosses) of the magnets in the Halbach array with a rectangular shape (which are magnetized in the x- or y-direction) and square shape (which are magnetized in the z-direction), when no external field is applied. The operating points are predicted on three-dimensional grids in the magnets. The idealized demagnetization curve of the magnets is also shown in Figure 6.6. The remanent magnetization of the simulated permanent magnets is $B_r = 1.23$ T and the relative permeability is $\mu_r = 1.05$. The figure shows that a single operating point for the magnet cannot be defined. The operating points are distributed over the full second quadrant and also partly in the first quadrant. Some parts of the magnets operate at low points in the BH-curve and are sensible to demagnetization. The magnet parts which operate at $B_x < 0.25$ T and at $B_z < 0.25$ T are identified in Figures 6.7a and b, respectively. These points are located near the edges of the permanent magnets.

The permanent magnets can be demagnetized both by external magnetic fields of the coils and by temperature rise. To analyze possible demagnetization by the magnetic fields of the coils, magneto-motive force (MMF) distributions in the planar actuator have been analyzed. For the position of the magnet array indicated in Figure 6.8, the magnetic flux density components caused by the MMF distributions are shown in Figure 6.9 for two loads: levitation only, and levitation and acceleration in the ^cy-direction with 14.1 m/s^2. The magnetic flux density distribution has been predicted 1 mm above the coils using FLUX3D. The clearance between coils and magnet is assumed to be 2 mm. The coordinate systems are indicated in Figure 6.8. The amplitude of the magnetic flux density distribution of the coils is small in comparison with the amplitude of the magnetic flux density distribution of the
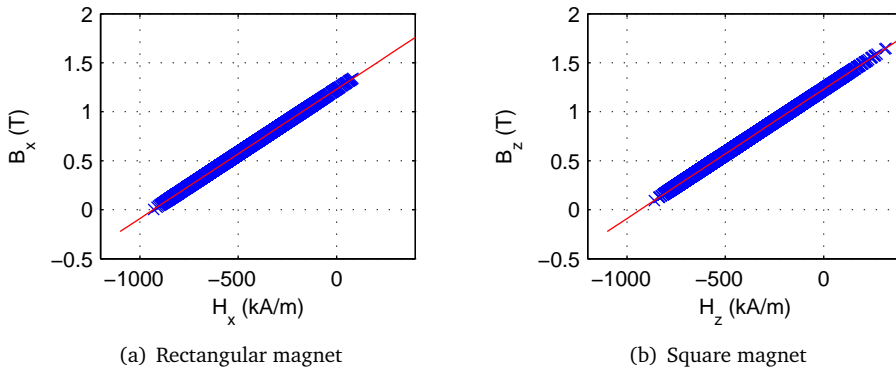
(a) Rectangular magnet   (b) Square magnet

Figure 6.6. *Operating points of the permanent magnets in the Halbach array of the planar actuator when no external magnetic field is applied.*

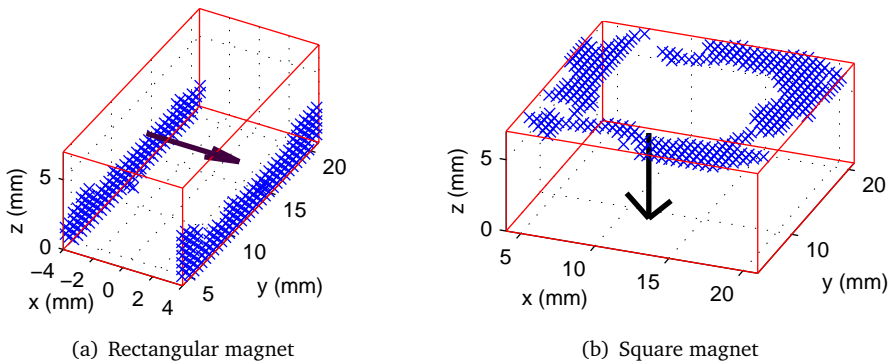(a) Rectangular magnet   (b) Square magnet

Figure 6.7. *Parts within the magnets with an operating point with $B < 0.25$ T when no external magnetic field is applied (the arrows indicate the magnetization direction).*

magnets, which is shown in Figure 6.10. This distribution has been predicted with the surface charge model (section 3.4).

Because of to the small magnetic flux density levels produced by the coils, demagnetization can only occur due to temperature rise or during assembly. To prevent any risk of demagnetization VACODYM 665HR is selected as magnet material, which has a high intrinsic coercivity of 1670 kA/m (20°C). Up to 100 °C,
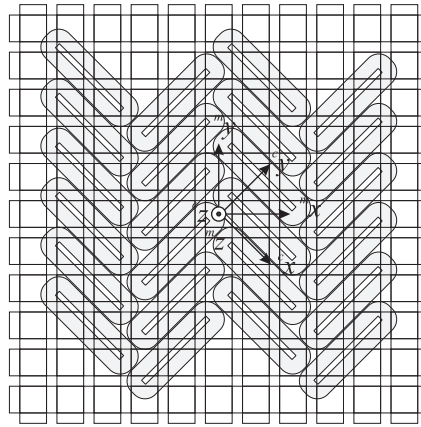
Figure 6.8. *Planar actuator position for which the mmf-distribution is shown in Figure 6.9.*

the knee-point of VACODYM 665HR is in the third quadrant of the BH-curve. The specifications of the magnet material can be found in Appendix C.

6.3   Eddy-current damping

Eddy currents are induced in conducting materials by varying magnetic fields. The eddy currents cause losses and damping. Electrical machines are usually constructed of laminated steel or soft magnetic composites to reduce the eddy-current losses. Most parts of the ironless planar actuator are made of aluminum plates, because it is cheap and can be easily machined. Aluminium is besides a good thermal conductor also a good electric conductor. Hence, induced eddy currents could cause unwanted damping. Alternatively, ceramic materials, such as aluminum oxide or aluminum nitrite, could be used for the construction of the stator. The advantage of these ceramic materials is that they are thermal conductors and electrical insulators. However, ceramic materials are expensive, hard and brittle. Hence, machining is difficult. The inverted planar actuator, discussed in section 2.2.2 has a ceramic stator construction.

In the designed planar actuator eddy currents can be induced in the following parts:

- the aluminum stator construction due to movements of the permanent-

(a) Levitation only

(b) Levitation and acceleration in $^c y$-direction

(c) Levitation only

(d) Levitation and acceleration in $^c y$-direction

(e) Levitation only
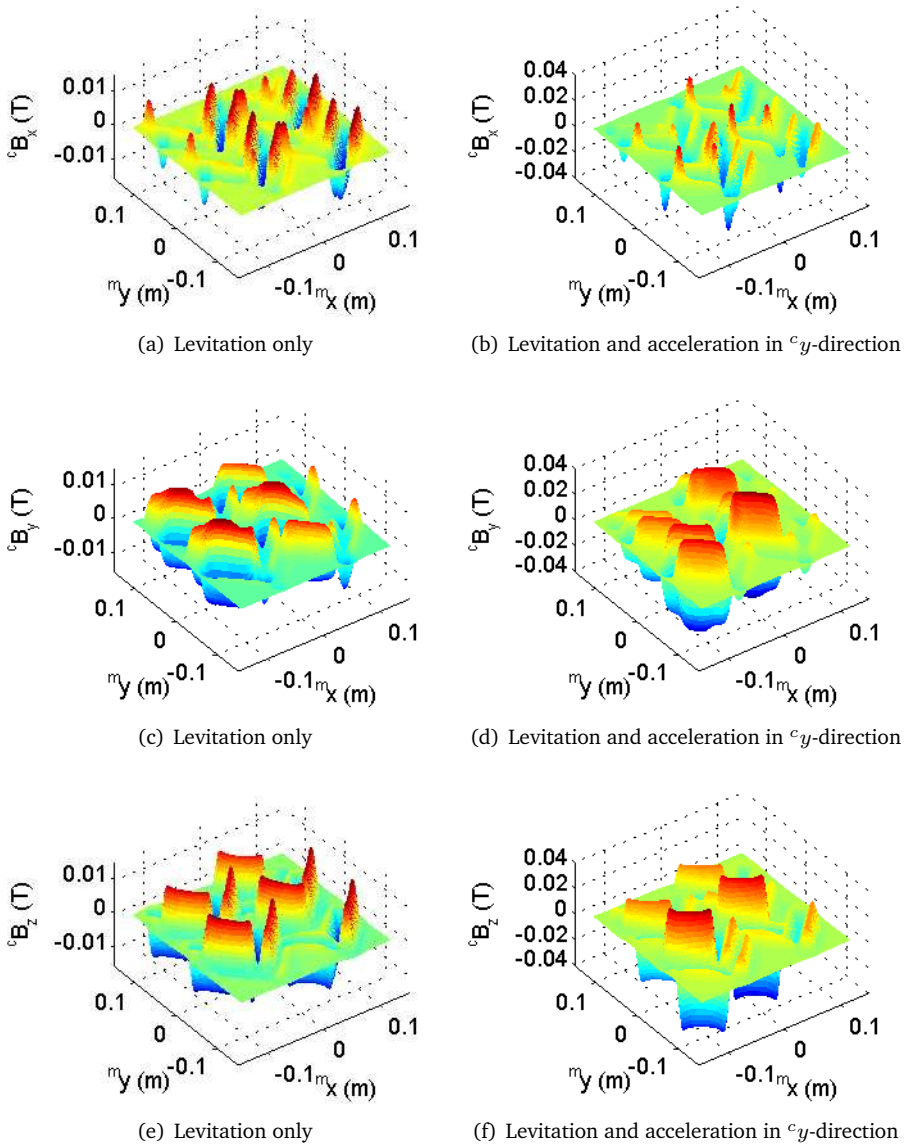
(f) Levitation and acceleration in $^c y$-direction

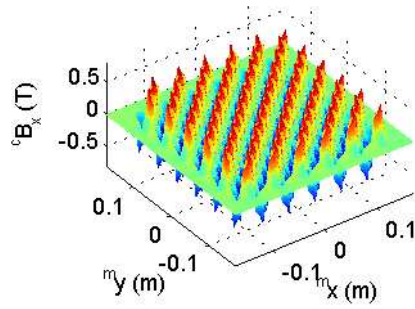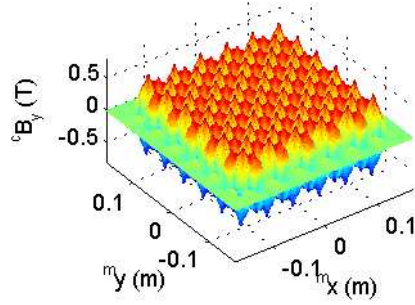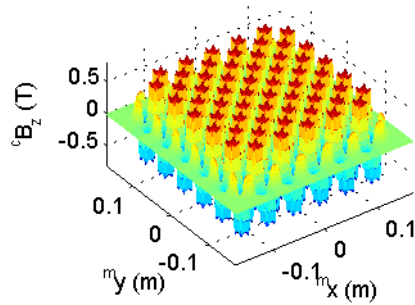**Figure 6.9.** *MMF-distribution of the coils in the HPPA for two loads: levitation, and levitation and acceleration in the $^c y$-direction, predicted 1 mm above the coils. Coordinate systems are defined in Figure 6.8.*

(a)

(b)

(c)

Figure 6.10. *Components of the magnetic flux density distribution of the permanent magnets in the HPPA, predicted 1 mm below the magnet array. Coordinate systems are defined in Figure 6.8.*
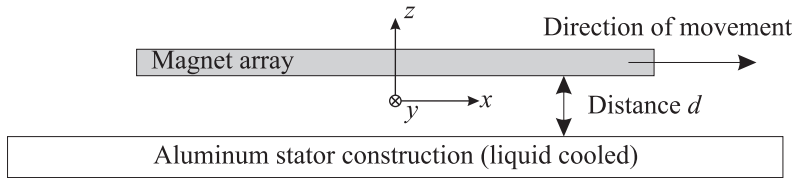
Figure 6.11. *Moving magnet array inducing eddy currents in the aluminum stator construction.*

       magnet array,
- the coils due to movements of the magnet array,
- the magnets due to the time varying field of the coils.

When the magnet array is moved above the stator, eddy currents are induced in the aluminum stator construction. Consequently, the system could behave as an eddy-current brake. To prevent this, the distance between the magnet array and the aluminum should be sufficiently large (Figure 6.11). The damping force due to eddy currents in the aluminum stator construction has been predicted by a transient finite element simulation in FLUX3D for different distances d between the aluminum plate and the magnet array (Figure 6.11). Only the first harmonic of the magnetic flux density distribution of the magnets is taken into account. The higher harmonics are neglected because they are small at larger distances from the magnet array. The total harmonic distortion of the magnetic flux density of the magnet array is less than 0.3% for $d = 10$ mm. Figure 6.12 shows the predicted eddy-current damping force. Corresponding to the analyses of eddy-current damping in [67, 57], a trend-line can be drawn through the predicted damping force points which is proportional to B^2, where B is the flux density on the surface of the aluminum. In the realized planar actuator, the coils are placed on aluminum oxide stands of 10 mm (Figure 6.13) to create a clearance of at least $d = 17.4$ mm between the magnets and the aluminum plate. The gap is filled with an epoxy resin.

      The amplitude of the magnetic flux density at the surface of the aluminum plate caused by the magnets is of the same order of magnitude as the flux density distribution of the coils on the magnet surface (Figure 6.9). As the resistivity of NdFeB is more than 40 times higher than that of the aluminum and the magnet array is segmented, induced eddy currents in the magnet array are neglected. The eddy currents in the coils are also neglected because the coils are wound of wire with a small diameter (0.45 mm) and not of foils.
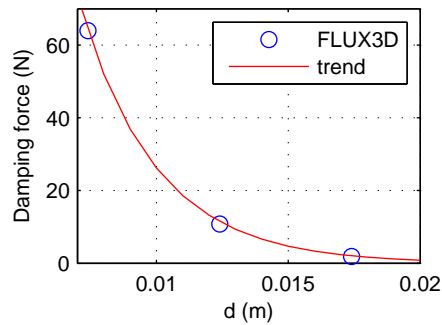
Figure 6.12. *Damping force due to induced eddy currents in the aluminum stator construction (velocity of the magnet array is equal to 1 m/s).*

Figure 6.13. *Coils in the planar actuator placed on aluminum oxide stands.*

6.4   Thermal design

The performance of an electrical machine is in general limited by the temperature distribution inside its configuration. For every material in an actuator, there is a maximum allowable temperature. Above this temperature, the materials are damaged or disintegrate. For example, at a certain temperature the wire insulation of a coil melts and a magnet demagnetizes. Therefore, the calculation of the temperature distribution is an important step in the design of an actuator.

Three different modes of heat transfer can be distinguished [53]:

- Conduction. Conduction is the heat flow through a substance and is governed by

$$\vec{q}_t = -k\nabla T, \tag{6.1}$$

where $\vec{q_t}$ is the heat flux, T is the temperature and k is thermal conductivity of the medium.

- Convection. Convection is the heat transfer from a surface to a moving fluid such as air or water. The heat flow is modeled by

$$q_t = h\Delta T, \tag{6.2}$$

where h is the convective heat transfer coefficient and $\Delta T = T_2 - T_1$ is the temperature difference between the surface and the fluid.

- Radiation. Energy between two surfaces is exchanged by the emission and absorption of electromagnetic waves and can also occur in vacuum. Radiation between one surface enclosed by another surface with equal emissivity ϵ_t can be described by

$$q_t = \sigma_{SB}\epsilon_t(T_1^4 - T_2^4), \tag{6.3}$$

where σ_{SB} is the Stefan-Boltzmann constant ($\sigma_{SB} = 5.67{\cdot}10^{-8}\ \mathrm{W\,m^{-2}K^{-4}}$), and T_1 and T_2 are the temperatures of the respective surfaces. In electrical machines the temperature difference is usually small, and, therefore, (6.3) can be linearized and expressed as

$$q_t = h_r(T_2 - T_1), \tag{6.4}$$

where h_r is the radiation heat transfer coefficient (at room temperature, $h_r \approx 6\epsilon_t$). Therefore, radiation heat transfer is usually not separately taken into account in the analysis of actuators [51]. Because the realized planar actuator will not be placed in vacuum, this approach is also applied in this case.

An engineering method to calculate the temperature distribution is to derive a thermal equivalent circuit (TEC). The thermal network is analog to an electrical network. The generated heat is represented by a current source and the temperature by a voltage. The materials are modeled by thermal resistors and heat capacitors. The thermal resistance R of a heat path in a material with thermal conductivity k is equal to

$$R = \frac{l}{kA}, \tag{6.5}$$

where l is the length of the heat path and A is the area of the surface through which the heat is transferred. Convection at a surface is modeled by a resistor with a resistance

$$R = \frac{1}{hA}. \tag{6.6}$$

In most electrical machines, all coils conduct the same rms-current. However, in the moving-magnet planar actuator the current in a coil is not only determined by the load but also by the path followed by the translator, as only the coils below the magnet array are energized. Moreover, for every millimeter the translator of the designed planar actuator is levitated higher above the stator, the coil currents increase with 19.4% and, consequently, the power dissipation increases with 42.7% (see (3.77)-(3.79)). Hence, without knowledge of the motion profile, the temperature cannot be accurately predicted.

To estimate the worst-case steady-state temperature distribution in the planar actuator, it is assumed that the rms-current in all coils is the same and, therefore, only heat is transferred in the z-direction. The thermal equivalent circuit of half a coil is shown in Figure 6.14. Only the heat path through the coil itself is modeled. Moreover, convection and radiation in the airgap are neglected. The thermal resistances are calculated with the material properties listed in Appendix C. The results of the analysis of the network are shown in Figure 6.15. Figure 6.15a shows the prediction of the coil (T_{coil}) and magnet (T_{magnet}) temperature with the thermal equivalent network and with a two-dimensional FEM in FLUX2D [8]. FLUX2D predicts a lower temperature because there is a also a heat path parallel to the coil in the epoxy resin surrounding the coil. The figure illustrates that the temperatures of the coil and magnet strongly depend on the thermal conductivity of the material (resistor $R_{spacing}$ in Figure 6.14) by which the space between the coils and the water-cooling system is filled (see also Figure 6.13). Most of the heat in the planar actuator is removed by the water-cooling system, as shown in Figure 6.15b.

Because of cost reasons, the space between the coils and the water-cooling system in the realized motor is filled with an epoxy resin containing 60% aluminum powder (RenCast CW 5156-1 / Ren HY 5158). This epoxy resin has a thermal conductivity of approximately 0.9 W/(mK), as estimated by the manufacturer. The thermal properties of the actuator could be significantly improved by using aluminum oxide plates ($k = 27 - 30$ W/(mK)) instead of this epoxy resin as demonstrated in Figure 6.15a. The temperature distribution predicted with FLUX2D for $k_{spacing} = 0.9$ W/(mK) is shown in Figure 6.16. To enforce the heat transfer in the z-direction only, adiabatic boundary conditions are applied on the sides of the problem. Except for the resin, the dominant thermal resistances are in the airgap and in the coil.

The thermal properties of the wire-wound coil are anisotropic. The thermal conductivity is high in the direction of the current but low in the directions perpendicular to the current because of the wire insulation layers (see also [77]). The thermal conductivity of the coil can be improved in an extra direction by the use of foil-wound coils; however, this will also result in damping caused by induced eddy
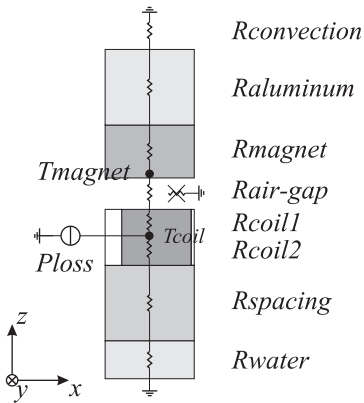
Figure 6.14. *Thermal equivalent network of half a coil.*
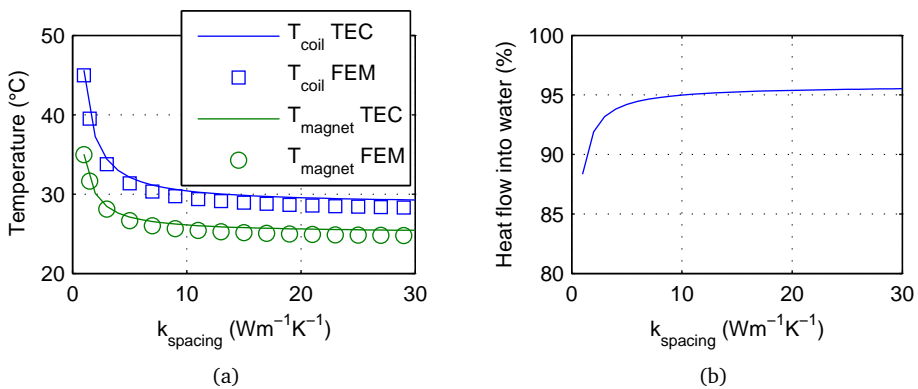
Figure 6.15. *Results of the analysis of the thermal equivalent network of half a coil for different values of the thermal conductivity of the resin $k_{spacing}$: a) Steady-state temperature, b) heat flow to the water-cooling system. Current density in the coil: $J = 3.5\,A/mm^2$ and ambient temperature: $20\,°C$.*

currents, as explained in section 6.3.

The temperature of the stator of the realized planar actuator can only be measured at the surface because no thermocouples have been embedded in the stator. Figure 6.17 shows a steady-state thermal image of the stator, measured with a FLIR

Figure 6.16. *Temperature distribution predicted by FLUX2D. Current density in the coil:* $J = 3.5 \, A/mm^2$, $k_{spacing} = 0.9 \, W/ \, (mK)$ *and ambient temperature: 20 °C.*

ThermaCAM S45 infrared camera. The current density in all coils is equal to 3.5 A/mm^2. As a result, the heat flow in the horizontal plane i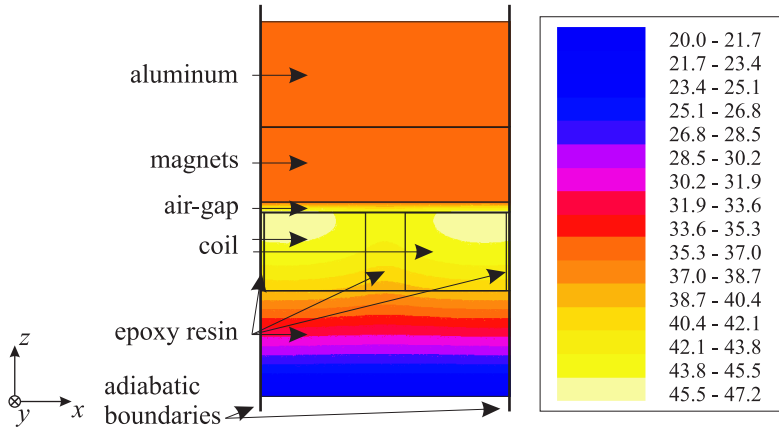s minimized, and the coils in the center of the stator have the same temperatures. The total power dissipation is 310 W. The measured thermal time constant of the stator is 4 minutes. The measurement is carried out without the translator present. In order to analytically verify this measurement, the translator is also omitted in the thermal model and a convective heat transfer is assumed on the stator surface with $h = 15$ W/(m^{2}K). The coil temperature predicted by the thermal model is equal to 48.2 °C. The maximum measured coil temperature is 43.2 °C. The difference is 25 %. The influence of aluminum oxide stands in the corners of the coils ($k = 30$ W/(mK)) can be recognized in the thermal image by the lower temperature in the corners of the coils.

Although the measurements results of Figure 6.17 are in reasonable good agreement with the predictions of the thermal equivalent network, the validity of the model is limited in situations, in which the current densities in the coils are not equal and, as a result, there is significant heat transfer in the horizontal plane. Figure 6.18 shows a thermal image of the stator in such situation. If the translator would have been present during the measurement, the currents in the 24 energized coils would have levitated the translator 2 mm above the stator coils for the position of the translator with respect to the coils as shown in Figure 6.8. The TEC model predicts a maximum coil temperature of 56.7 °C, whereas a maximum temperature
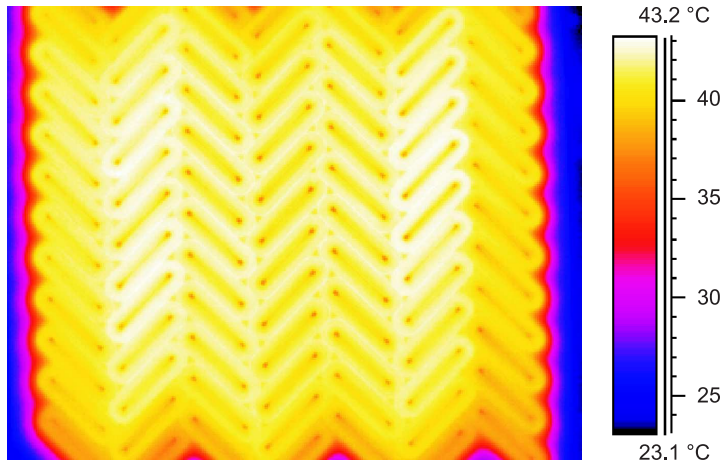
Figure 6.17. *Thermal image of the stator of the planar actuator, $J = 3.5\,A/mm^2$, ambient temperature: 22.8 °C.*
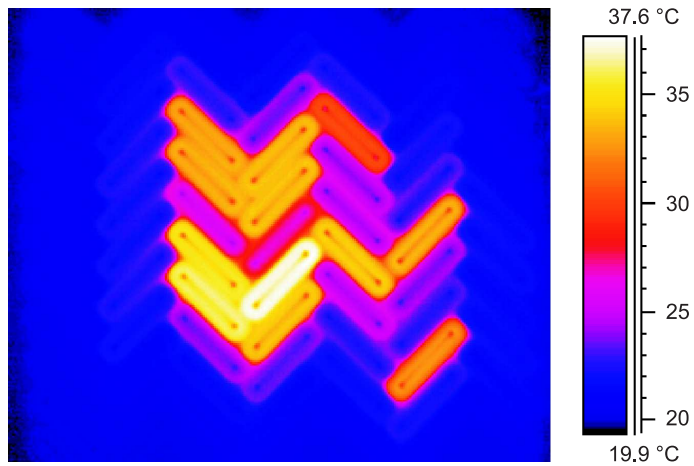

Figure 6.18. *Thermal image of the stator of the planar actuator. The currents would have levitated the translator 2 mm above the stator coils with 24 coils. Ambient temperature: 20.0 °C.*

of 37.6 °C is measured.

To investigate the thermal characteristics of the planar actuator more thoroughly, the TEC model should be expanded to multiple coils with heat paths in the horizontal plane.

6.5   Power amplifiers

In the analysis of the moving-magnet planar actuator it has been assumed that the power amplifiers are ideal current sources. To obtain the desired performance of the HPPA, which is specified in Table 6.1, the number of turns in the coil and the voltage and current specifications of the amplifiers should be matched. For synchronous permanent-magnet machines, these specifications can be derived using the phasor diagram of the decomposed system, obtained by Park's transformation. Due to the non-linear commutation algorithm of the planar actuator, which results in non-sinusoidal current waveforms with variable shape, amplitude and frequency, such an approach cannot be applied to the planar actuator.

With permission of ASML, the Prodrive PADC3AX52/6 power amplifiers are selected to supply the coils in the planar actuator. This amplifier is a low-noise PWM amplifier with a digital interface. The bandwidth of the current-loop is 4.0 kHz (defined as the frequency at which the open-loop transfer crosses the 0 dB axis). Because of the high bandwidth, its linearity and the low offset, the power amplifier can be considered to be ideal for this application. The voltage and current specifications are ± 52 V and ± 6 A, respectively.

The number of turns of the coils has been determined by analyzing the coil currents calculated by the commutation algorithm, which are necessary to exert the worst-case wrench on the translator. It has been verified that within the current limit of ± 6 A, a levitation force and a force vector in any direction in the xy-plane with a length of $|F_{xy}| = 10m$ can be produced simultaneously, when the coils of the HPPA have 319 turns and the clearance between stator and translator is equal to 2 mm [73]. In Figure 6.19, the minimum acceleration vector in the xy-plane, $|a_{xy}|$, is shown. Due to the switching between different coil sets and the variable clearance between the stator and the translator, the maximum acceleration and speed of the translator which can be reached within the specifications of the power amplifier is trajectory dependent. The trajectories used in section 7.5 are examples of trajectories with higher speed and acceleration levels.

The required voltage range of the power amplifier is dependent on the motion profile. The voltage of all coils in the planar actuator can be derived using the
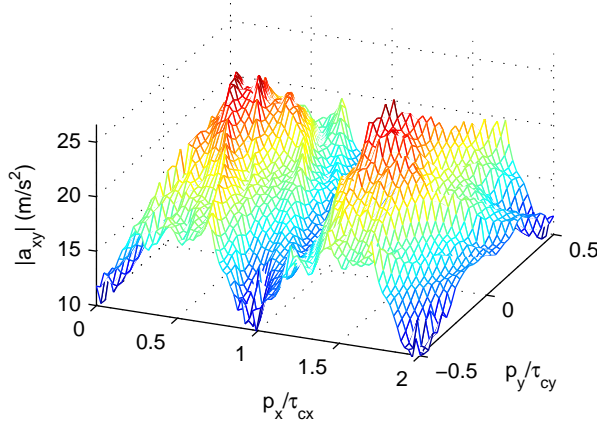
Figure 6.19. *Minimum acceleration in the xy-plane $|a_{xy}|$ of the HPPA (clearance: 2 mm, $F_z = mg$, $\vec{T} = \vec{0}$).*

voltage equation of a single coil (3.86)

$$\vec{u} = \mathbf{R}\vec{i} + \mathbf{L}\frac{d\vec{i}}{dt} + J_{\tilde{\mathbf{\Lambda}}}(\vec{q})\frac{d\vec{q}}{dt},\qquad(6.7)$$

where $J_{\tilde{\mathbf{\Lambda}}}(\vec{q})$ is the Jacobian of the flux of the permanent-magnet array linked by the respective coils, and $\mathbf{R}$ and $\mathbf{L}$ are the coil resistance and inductance matrices, respectively. Substituting (4.28), the voltage equation for the set of 24 active coils in the planar actuator is given by

$$\vec{u} = \mathbf{R}\mathbf{\Gamma}^{-}(\vec{q})\,\vec{w} + \mathbf{L}\frac{d\mathbf{\Gamma}^{-}(\vec{q})}{dt}\vec{w} + \mathbf{L}\mathbf{\Gamma}^{-}(\vec{q})\frac{d\vec{w}}{dt} + \mathbf{\Gamma}^{\mathsf{T}}(\vec{q})\frac{d\vec{q}}{dt}.\qquad(6.8)$$

As a result, the voltage is expressed as function of the position, the velocity, the wrench and the time derivative of the wrench and can be evaluated for different motion profiles.

The voltage equation (6.8) consists of resistive and inductive terms, and the back-EMF. The resistance and self-inductance of the coils of the planar actuator have been measured with a network analyzer: $R = 5.7\ \Omega$ and $L = 3.8$ mH ($T = 20°$C). The mutual inductances have been calculated from a 3-D FEM simulation.
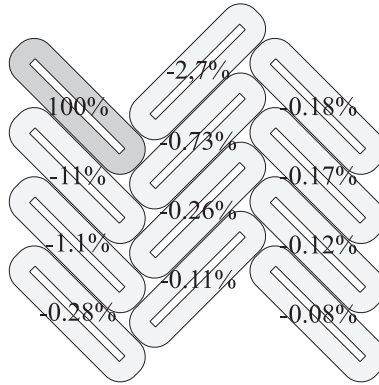
Figure 6.20. *Mutual coupling between the top-left coil and its neighboring coils expressed as a percentage of the self-inductance of the top-left coil.*

In Figure 6.20 the mutual coupling of the top-left coil with eleven neighboring coils is indicated. The mutual coupling between the coils is relatively small. Each coil in the planar actuator is mainly coupled with the two adjacent coils, located in the same column of coils. When the translator is traveling at the specified speed of 1.0 m/s in either the ^{c}x- or ^{c}y-direction, as defined in Figure 6.8, the fundamental frequency, f, of the current is equal to

$$f = \frac{v}{2\tau_n} = 28.3 \text{ H}z. \qquad (6.9)$$

and the back-EMF is limited to ± 8.2 V. Given the values of the maximum current, back-EMF, resistance and inductance, it can be seen that the voltage equation is dominantly resistive and that the voltage specification of the PADC3AX52/6 (± 52 V) is sufficient to reach the acceleration and speed specified in Table 6.1. This is also confirmed by simulations of (6.8).

6.6   Conclusions

Four design aspects of the planar actuator are discussed in the chapter. The working point of the permanent magnets in the magnet array has been analyzed to select the magnetic material. A single working point cannot be defined. The working points are spread over the second quadrant and some parts of the magnets operate

near the third quadrant. Therefore, there is a risk of demagnetization. Because the magnetic fields of the coils in the realized planar actuator are small, the main risk of demagnetization is temperature rise.

To prevent that eddy currents are induced due to movements of the magnet array in the stator construction, the distance between the magnet array and the conducting parts of the construction should be sufficiently large. In the realized planar actuator, this space is filled with an epoxy resin with a relatively low thermal conductivity.

The thermal behavior of the planar actuator is mainly determined by the low thermal conductivity of this resin. The thermal properties can be significantly improved by constructing the stator parts of ceramic materials.

The current and voltage specifications of the power amplifiers and the number of turns of the coils have been matched. Analysis of the voltage equation show that the coils of the planar actuator behave dominantly resistive.

Chapter 7

Experiments

In this chapter, the electromechanical models (chapter 3) and the commutation algorithm (chapter 4) are experimentally verified on the realized herringbone pattern planar actuator (HPPA). The force and torque exerted on the translator have been measured with a 6-DOF load cell. After verification of the open-loop commutation algorithm, the load cell has been removed and the HPPA has been made fully operational by feed-back control. Test results of the controlled planar actuator have bee published in [37, 42]

7.1 Measurement system

The measurements on the HPPA are carried out on a test-bench, which is constructed on top of the base frame of an Assembléon H-drive [59, 66]. This gantry consists of three linear motors. Two motors are positioned in parallel ($y1$ and $y2$). Between the translators of these motors a third linear motor is mounted which can move in the x-direction. By displacing the $y1$- and $y2$-motors with respect to each other, the x-beam can rotate about the z-axis (± 5 mrad). An overview of the test-bench is shown in Figure 7.1. The test-bench has three main functions.

Force and torque measurement

The translator of the HPPA can be mounted via a 6-DOF load cell (JR3 45E15A4-I63-S 100N10) to the translator of the x-motor of the H-drive. The H-drive can be used to position the translator with the magnet array above the stator coils and the
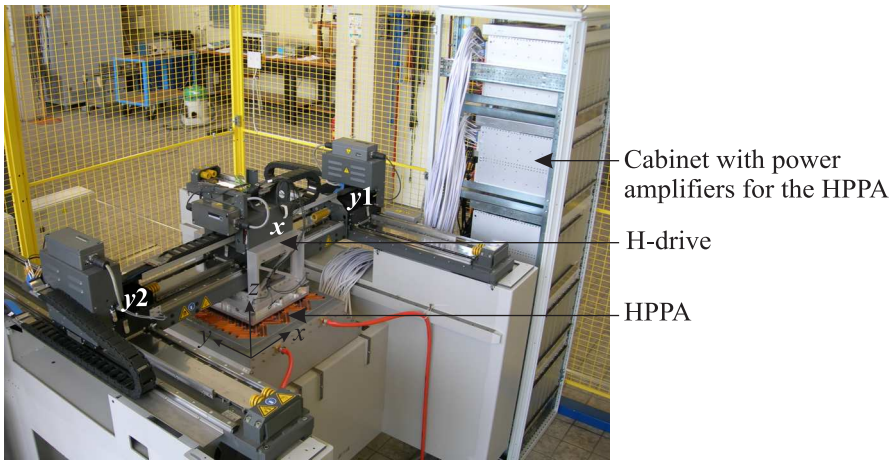
Figure 7.1. *Planar actuator test-bench.*

force and torque components can be measured with the load cell. With this configuration, the force and torque acting on the translator of the HPPA itself are measured. However, also disturbances from the H-drive are measured because the bandwidth of the load cell (150 Hz) is much larger than the bandwidth of the controllers of the H-drive (30 Hz). The force and torque are measured statically (stand-still) or quasi-statically at low speed (0.02 m/s). The quasi-statically measured data is filtered off-line with a fourth order anti-causal low-pass filter with a cut-off frequency of 25 Hz. This filter does not introduce a phase shift in the measurement data. Because of the low measurement speed, the frequency of the measured force and torque signals is low (first harmonic: 0.57 Hz at 0.02 m/s) and, therefore, the higher harmonics of the force and torque are not suppressed by the filter.

Position measurement

The position on the μm and sub-μm scale can be measured with several techniques, e.g. optical encoders, laser triangulators, laser interferometers, inductive sensors and capacitive sensors. These types of sensor differ mainly in accuracy, range and cost. For the measurement system of the HPPA cost was an important issue. Because the H-drive itself is equipped with 1 μm resolution optical encoders, it was decided to measure the position of the translator of the HHPA with respect to the

Figure 7.2. *Detail of the measurement frame of the HPPA.*

H-drive with inductive sensors (160 nm rms-resolution) and to use the encoders of the H-drive for the long-stroke position measurement. As the range of the inductive sensors is limited to 2 mm, the H-drive should move simultaneously with the translator of the HPPA.

Eight inductive sensors are mounted on the measurement frame of the H-drive. Four of them measure the distance between the measurement frame and the translator of the HPPA in the z-direction, two in the x-direction and two in the y-direction. The measurement targets are located at the corners (z-direction) and the centers of the edges of the translator (x- and y-directions). A detail of the measurement frame with the inductive sensors (indicated by the red arrows) is shown in Figure 7.2. The position and orientation of the translator with respect of the stator coils in six degrees-of-freedom are reconstructed from the data of the in total eleven position sensors.

Safety

Because of the position measurement system, the H-drive is always moving together with the translator of the planar actuator. To prevent damage caused by contact between the stator and the translator of the HPPA due to, for example, unstable controllers or power failure, the stroke of the translator of the HPPA with respect to the measurement frame is limited by four pins (diameter 4.9 mm) which are captured by over-sized holes (diameter 6 mm) in the translator of the HPPA. Two of these pins are indicated in Figure 7.2. The disadvantage of these pins is that the
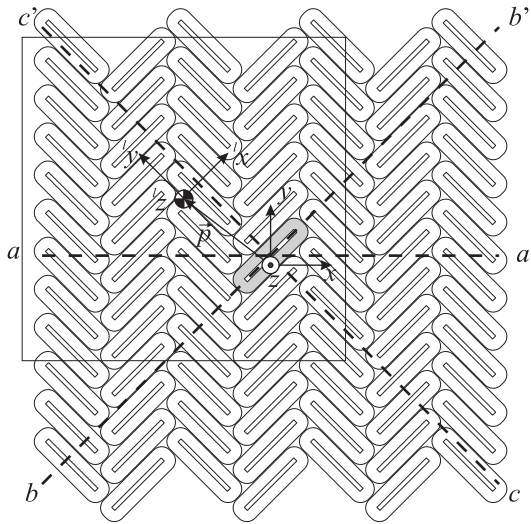
Figure 7.3. *Coordinate system definition for the measurement of the force and torque exerted by a single coil (excited coil indicated in gray). The magnet array is indicated by the square.*

rotation angles of the translator of the HPPA are limited to 6 mrad. Once the HPPA is in control, there is no contact between its translator and the measurement frame.

7.2   Force and torque exerted by a single coil

In sections 3.4, 3.5, 3.6, three different electromechanical models of the planar actuator are derived: the surface charge model, the harmonic model and the analytical model (based on the current sheets). To verify these models, the force and torque exerted on the translator of the HPPA by one coil have been measured. The current in the coil was equal to 1 A. The excited coil is indicated in Figure 7.3. The figure also shows the coordinate system (x, y, z) in which the position $\vec{p}$ of the translator is measured. To show the decoupling of the force produced in the x- and y-directions in the measurement results, the force and torque are measured and expressed in the coordinate system indicated by the subscript ^{l}. This coordinate system is located in the geometric center of the load cell. The torque is measured
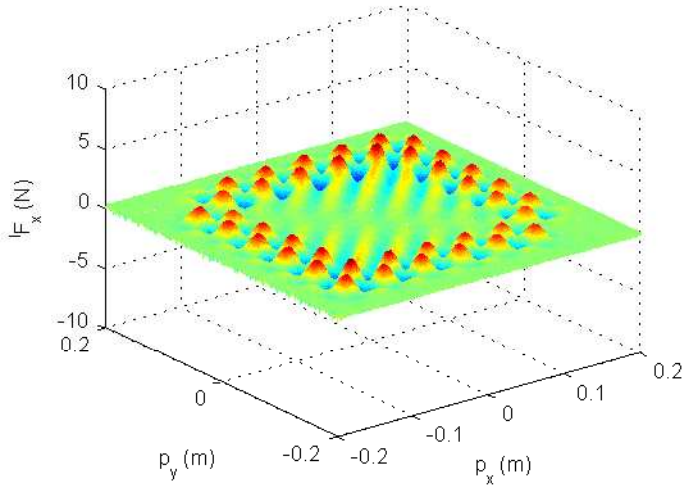
Figure 7.4. *Measured force $^l F_x$ exerted by a single coil (i=1A, clearance: 1.5 mm).*
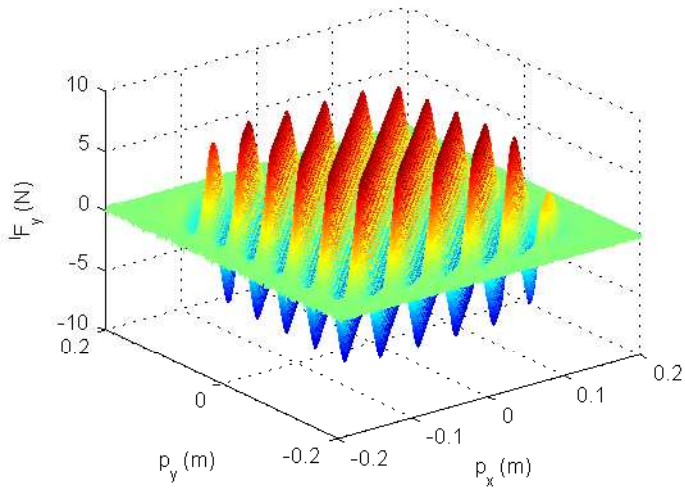
Figure 7.5. *Measured force $^l F_y$ exerted by a single coil (i=1A, clearance: 1.5 mm).*
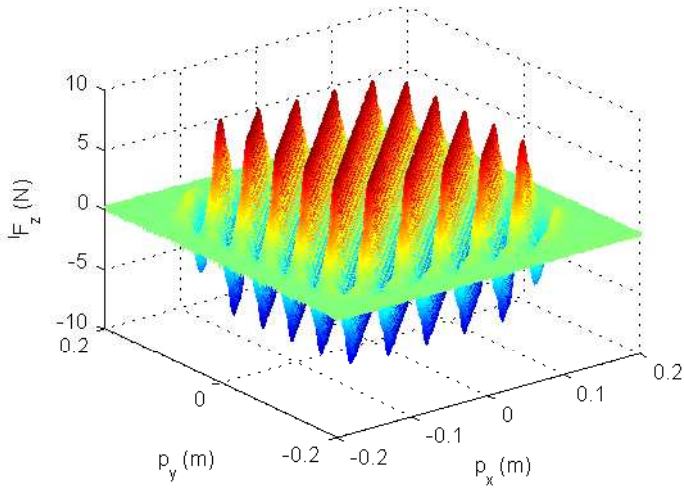
Figure 7.6. *Measured force $^l F_z$ exerted by a single coil (i=1A, clearance: 1.5 mm).*
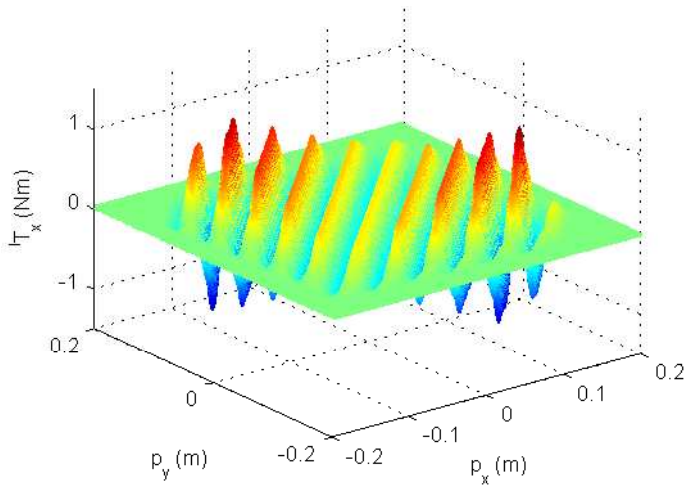
Figure 7.7. *Measured torque $^l T_x$ exerted by a single coil (i=1A, clearance: 1.5 mm).*
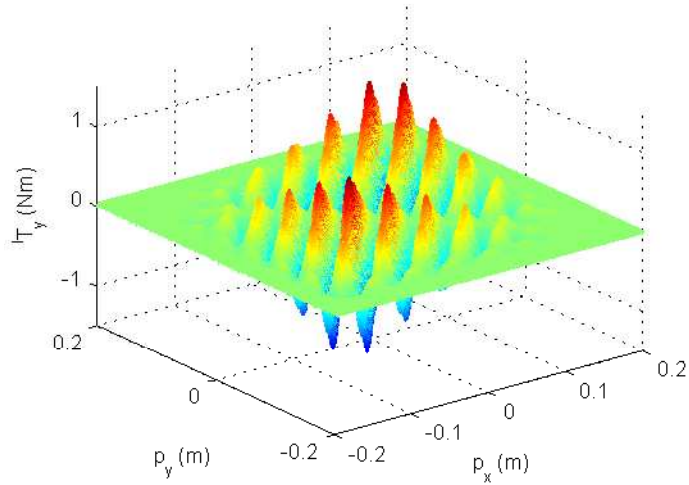
Figure 7.8. *Measured torque ^lT_y exerted by a single coil (i=1A, clearance: 1.5 mm).*
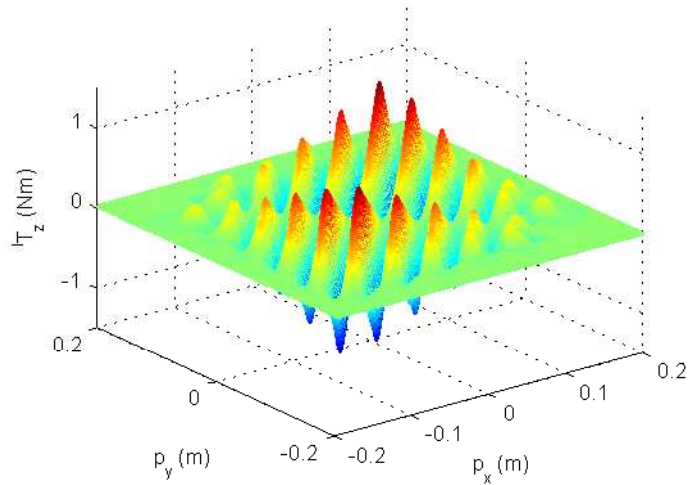
Figure 7.9. *Measured torque ^lT_z exerted by a single coil (i=1A, clearance: 1.5 mm).*

Figure 7.10. *Measured and predicted force $^l F_x$ exerted by a single coil (i=1A, clearance: 1.5 mm, $p_y = 8.3$ mm).*

Figure 7.11. *Measured and predicted force $^l F_y$ exerted by a single coil (i=1A, clearance: 1.5 mm, $p_y = 8.3$ mm).*

Figure 7.12. *Measured and predicted force $^l F_z$ exerted by a single coil (i=1A clearance: 1.5 mm, $p_y = 8.3$ mm,).*
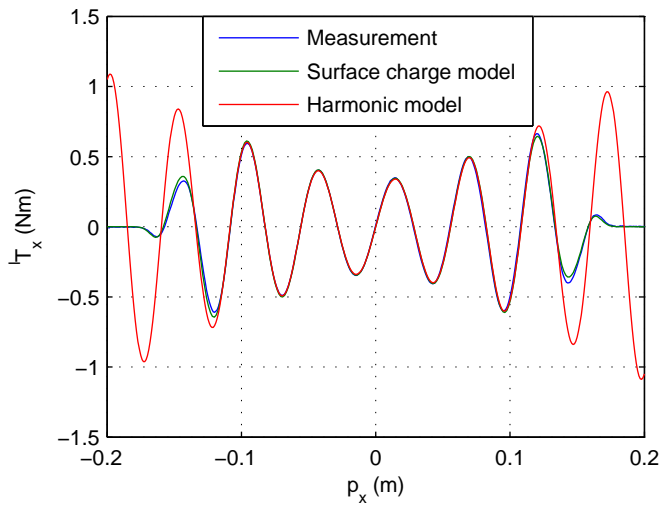
Figure 7.13. *Measured and predicted torque $^l T_x$ exerted by a single coil (i=1A, clearance: 1.5 mm, $p_y = 8.3$ mm).*
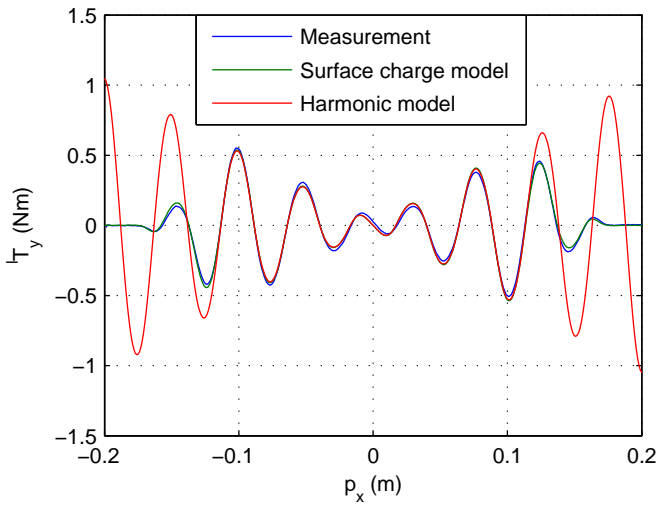
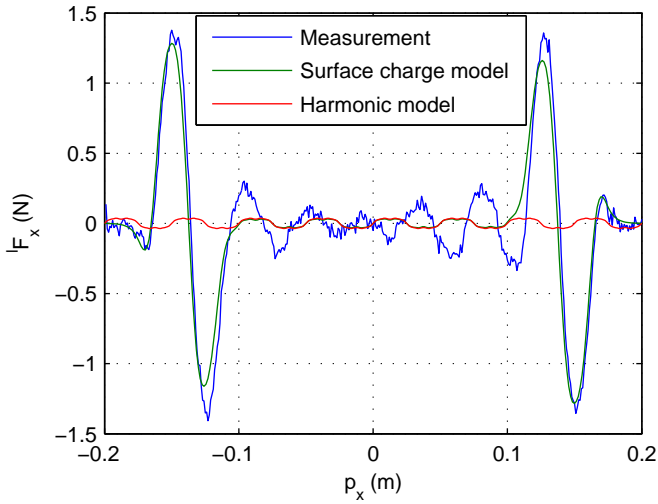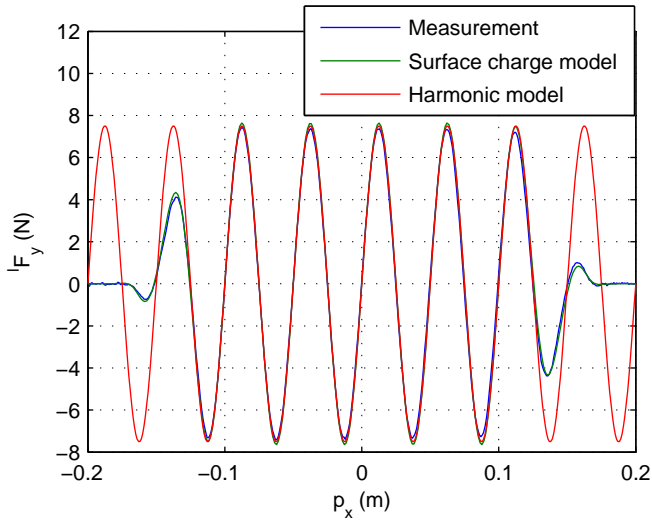**Figure 7.14.** *Measured and predicted torque ^lT_y exerted by a single coil (i=1A, clearance: 1.5 mm, $p_y = 8.3$ mm).*
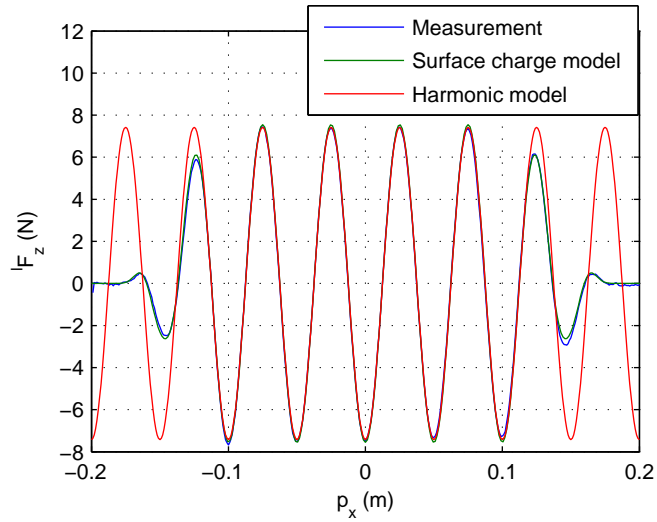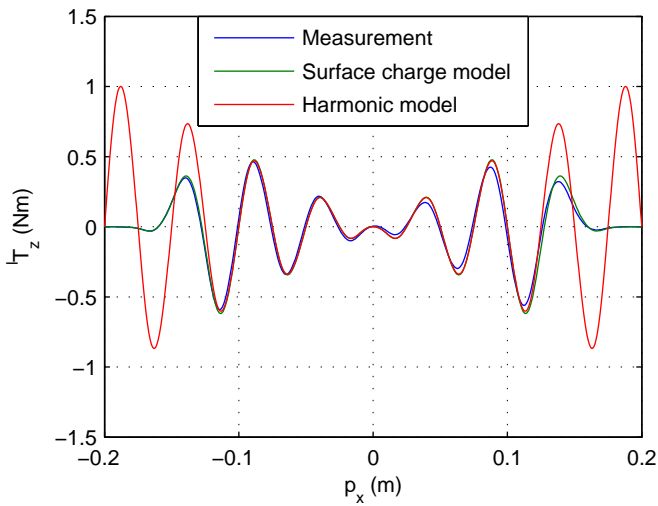

Figure 7.15. *Measured and predicted torque ^lT_z exerted by a single coil (i=1A, clearance: 1.5 mm, $p_y = 8.3$ mm).*

Table 7.1. *Differences between the predictions of the analytical model and harmonic model (-0.2 m $< p_x < 0.2$ m and -0.2 m $< p_y < 0.2$ m), clearance: 1.5 mm*

Component	rms difference
${}^l F_x$	0.031 N
${}^l F_y$	0.014 N
${}^l F_z$	0.034 N
${}^l T_x$	0.0046 Nm
${}^l T_y$	0.0056 Nm
${}^l T_z$	0.0047 Nm

and predicted about the origin of this coordinate system. The geometric center of the load cell is located 28.8 mm above the mass center point of the translator itself.

The measured force and torque components are shown in Figures 7.4-7.9. The decoupling of the force in the ${}^l x^l y$-plane is clearly visible in Figure 7.4 and Figure 7.5. The higher force levels near the edges of the magnet array in Figure 7.4 are caused due to the fact that the force produced on the short sides of the coil does not cancel because of the end-effects of the magnet array. As predicted in section 3.6.2, the amplitudes of the force components ${}^l F_y$ and ${}^l F_z$ are equal. In the torque waveforms (Figures 7.7-7.9), it is clearly visible that the torque is both a function of the relative position (the electrical angle) and the absolute position of coil with respect to the magnet array.

To validate the electromechanical models, the measurement results and the prediction of the three models are compared for the positions of the mass center point of the magnet array along the dashed line $a - a'$, which is located at $p_y = 8.3$ mm and is indicated in Figure 7.3. The results of the measurements and the predictions of the surface charge model and the harmonic model are shown in Figures 7.10-7.15. Except for the ${}^l F_x$-component, the measurements and the predictions are in good agreement. The large deviation for this component is probably caused by cross-talk in the load cell.

Contrary to the harmonic model and the analytical model, the surface charge model includes the end-effects of the magnet array. Figure 7.16 shows a detail of the measurement and prediction of the force component ${}^l F_z$. The surface charge model
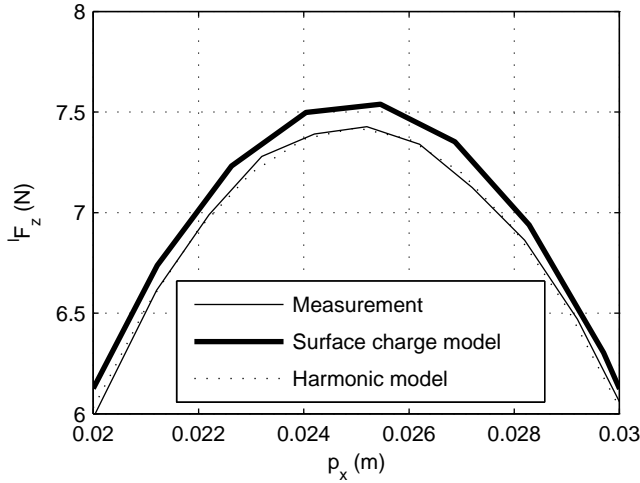
Figure 7.16. *Measured and predicted force ^lF_z exerted by a single coil (i=1A clearance: 1.5 mm, $p_y = 8.3$ mm,).*

predicts a 2% higher force value than the harmonic model because the relative permeability of the permanent magnets ($\mu_r = 1.03$ is assumed in the harmonic model) is not taken into account in the surface charge model.

The analytical model is not shown in Figures 7.10-7.15, because the difference between the prediction of the harmonic model (with 15 harmonics taken into account) and the analytical model (based on current sheets) is small. The rms force and torque differences between both models determined over the area (-0.2 m $< p_x < 0.2$ m and -0.2 m $< p_y < 0.2$ m) are listed in Table 7.1. Hence, for the prediction of the force and torque in the HPPA, the analytical model is a fast and accurate substitute for the harmonic model.

7.3   EMF

The decoupling of the force production in the xy-plane by the rectangular stator coils is also verified by the measurement of the EMF, as both the force

$$F = \frac{\partial \Lambda}{\partial x} i, \tag{7.1}$$
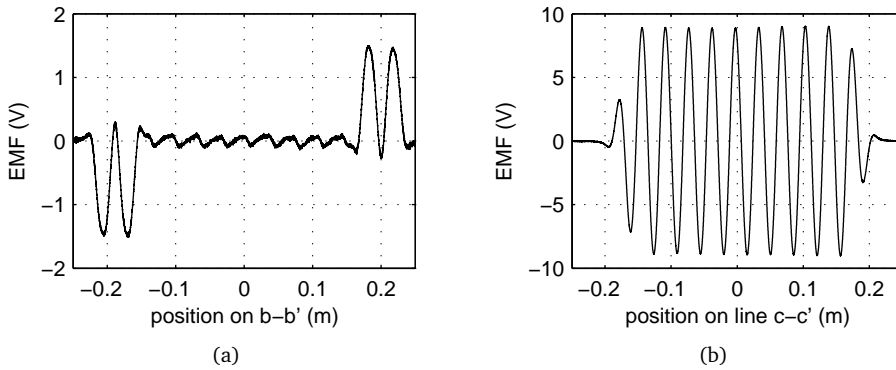
Figure 7.17. *EMF measurements over (a) line $b - b'$ and (b) line $c - c'$. The lines are defined in Figure 7.3, speed in the direction of the line: 1 m/s, clearance: 0.5 mm.*

and the EMF

$$\text{EMF} = -\frac{\partial \Lambda}{\partial x}\frac{\mathrm{d}x}{\mathrm{d}t}, \tag{7.2}$$

are proportional to the change of flux linkage, Λ, in the coil (see also section 3.7). The EMF in the gray coil in Figure 7.3 has been measured while moving the mass center point of the translator of the HPPA over both the lines $b - b'$ and $c - c'$ in Figure 7.3. The clearance between coils and magnet array was 0.5 mm. The two EMF waveforms are shown in Figure 7.17. The coil is designed to exert only force on the translator in the ^{l}y-direction and not in the ^{l}x-direction. Consequently, no voltage should be induced in the coil when moving the magnet array over the line $b - b'$. Neglecting the end-effects of the magnet array, the cross-coupling between the induced voltages, and, therefore, the force components in the xy-plane is 1%.

7.4   Open-loop commutated planar actuator

The commutation algorithm, which is presented in section 4.3, is verified by measuring the force and torque components statically for different xy-positions of the magnet array. The coil currents are determined by the commutation algorithm in order to obtain a constant wrench. Similar to Figure 5.9, the allowed positions of the mass center point of the translator and the switching boundaries of the 28 different sets of active coils are shown in Figure 7.18. The area in which the mea-
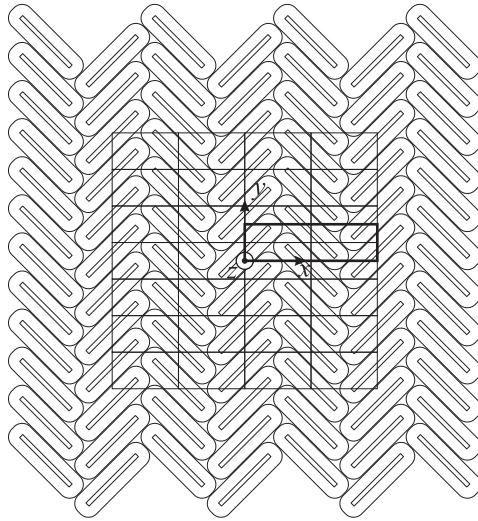
Figure 7.18. *Boundaries of the 28 sets of active coils in the HPPA (see also Figure 5.9). Black rectangle indicates the area in which the open-loop commutated HPPA measurement is carried out.*

surement is carried out, is indicated in black in Figure 7.18. In this area, there are four different sets of active coils. The measured force and torque components are expressed in the coordinate system indicated in Figure 7.18. It should be noted that the torque is measured about the geometrical center of the load cell and not about the mass center point of the translator. The commutation algorithm was corrected for this virtual mass center point.

The reference force and torque set-points during the measurements were $F_x = F_y = F_z = 15$ N and $T_x = T_y = T_z = 0$ Nm. The results of the measurements and the predictions with the harmonic model are shown in Figures 7.19 and 7.20. The decoupled force and torque components have significant higher ripples than predicted, as summarized in Table 7.2. Possible causes for these larger ripples are:

- Misalignment of the translator with respect to the stator coils. Simulations of the HPPA, which is misaligned in the xy-plane, confirm that the ripple of the z-component of the force increases significantly less than the force ripples in the x- and y-components.
- Tolerance of the permanent-magnet properties (i.e. remanent magnetiza-

(a) Measurement

(b) Prediction

(c) Measurement

(d) Prediction

(e) Measurement

(f) Prediction
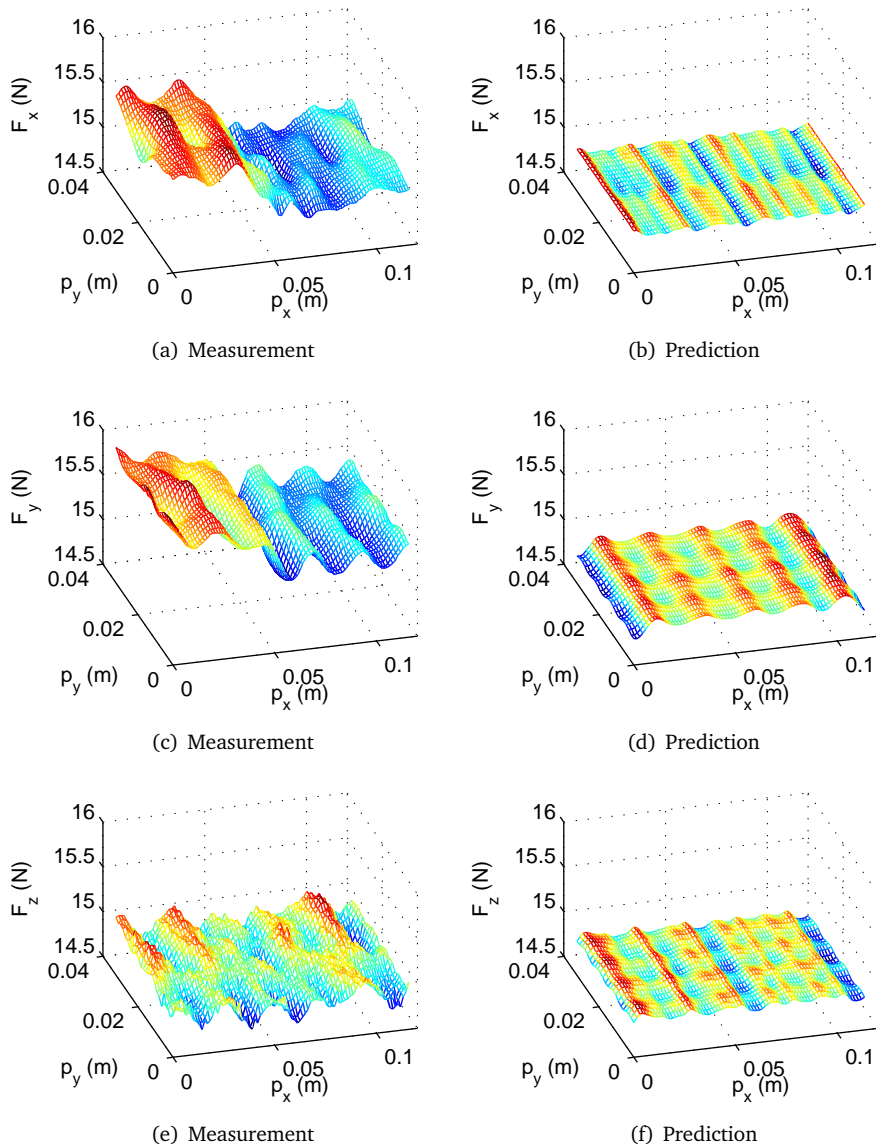
Figure 7.19. *Measured and with the harmonic model predicted force components F_x, F_y and F_z of the open-loop commutated HPPA, $\vec{w} = \begin{bmatrix} 15 & 15 & 15 & 0 & 0 & 0 \end{bmatrix}^{\top}$ and clearance: 1.5 mm.*

(a) Measurement

(b) Prediction

(c) Measurement

(d) Prediction

(e) Measurement

(f) Prediction
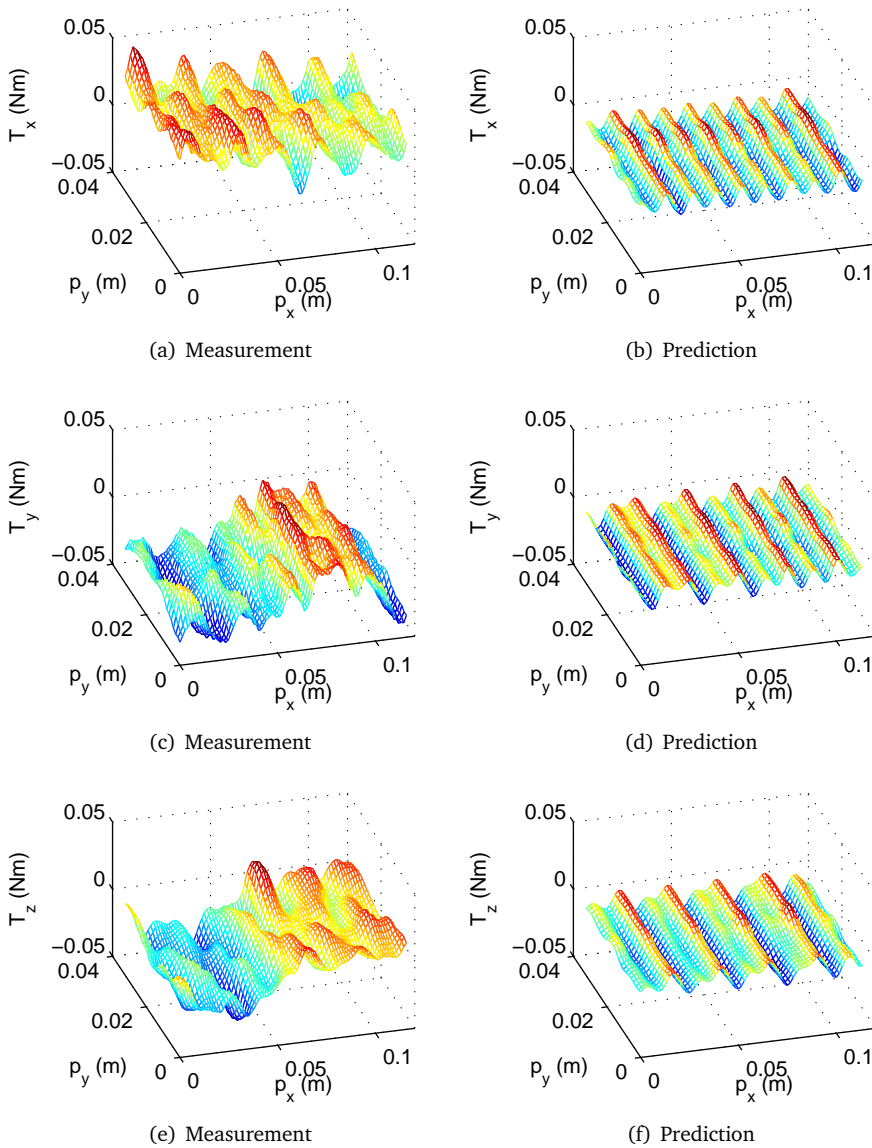
Figure 7.20. *Measured and with the harmonic model predicted torque components T_x, T_y and T_z of the open-loop commutated HPPA $\vec{w} = \begin{bmatrix} 15 & 15 & 15 & 0 & 0 & 0 \end{bmatrix}^\mathsf{T}$ and clearance: 1.5 mm.*

Table 7.2. *Measured and with the harmonic model predicted rms force and torque ripples of the open-loop commutated HPPA. Clearance: 1.5 mm, $\vec{w} = [15 \ 15 \ 15 \ 0 \ 0 \ 0]^{\mathsf{T}}$.*

Component	Prediction	Measurement
F_x	0.18 %	1.5%
F_y	0.37 %	1.3%
F_z	0.25 %	0.60%
T_x	0.0071 Nm	0.012 Nm
T_y	0.0064 Nm	0.014 Nm
T_z	0.0054 Nm	0.013 Nm

tion, magnetization angle and dimensions) and placement,
- Tolerances in the coil dimensions and placement.

Because the force and torque were considered to be sufficiently decoupled, the cause of the higher ripple values was not further investigated.

7.5 Controlled planar actuator

The measurements of the open-loop commutated HPPA show that the force and torque components in the planar actuator are statically decoupled and have low ripples. Also, frequency domain identification of the system with noise shows a low cross-coupling of the force components and the torque components of approximately 40 dB. For that reason, it was decided to implement six SISO-controllers to control the six degrees-of-freedom of the planar actuator. The SISO controllers are quasi-PID-controllers with a bandwidth of 35 Hz. In addition to feed-back control, mass and inertia feedforward control has been implemented. The movement of the translator of the HPPA are third-order motion profiles, which are continuous in position, velocity and acceleration. Both the identification and the controller structure are discussed in detail in [73].

The position and angle errors of the HPPA have been measured for static levitation and several trajectories. These trajectories and the switching boundaries of
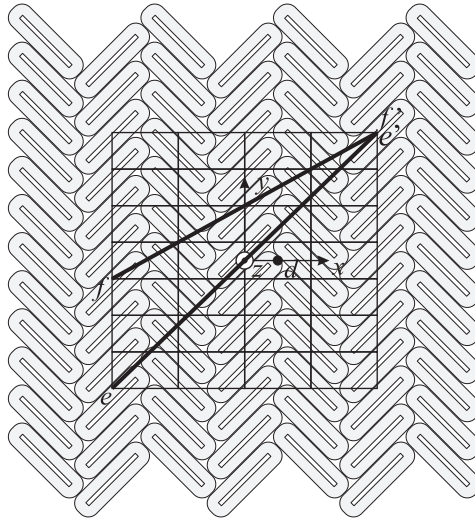
Figure 7.21. *Trajectories d, $e - e'$ and $f - f'$ on which the position and angle errors of the controlled HPPA have been measured.*

the 28 different active coil sets are shown in Figure 7.21. Trajectory d is a movement in the z-direction at a position at which none of the 24 active coils is penalized in the commutation, trajectory $e - e'$ is a trajectory in the xy-plane at high speed and acceleration, and trajectory $f - f'$ is a trajectory in the xy-plane through points at which only 15 coils are active. The clearance between stator and translator, maximum velocity v, acceleration a and jerk j are specified in Table 7.3 for the different trajectories. During these movements, the rotation angles are kept stable.

A trajectory in the z-direction and levitation at standstill have been measured at point d, which is indicated in Figure 7.21. During this measurement the H-drive, to which the measurement frame is mounted, was switched off to reduce the noise of the position measurement. The translator was moved in the z-direction from 1.0 mm clearance to 1.5 mm clearance, while the other degrees-of-freedom were kept stable around a constant position. Figure 7.22 shows the acceleration profile, the estimated power dissipation in the coils and the position and angle errors. The motion in the z-direction causes mainly errors in the z-direction and the rotation angles. Figure 7.23 shows the error of the 6-DOF steady-state position 0.5 second after the motion in the z-direction started. The rms-errors are 0.1 μm and 1 μrad,

Table 7.3. *Specification of the motion profiles at different trajectories*

Trajectory	d	$e - e'$	$f - f'$	
clearance	1.0-1.5	1.0	1.0	mm
v_x	0	1.0	1.0	m/s
v_y	0	1.0	0.575	m/s
v_z	0.015	0	0	m/s
a_x	0	10	10	m/s^2
a_y	0	10	5.75	m/s^2
a_z	1	0	0	m/s^2
j_x	0	1000	1000	m/s^3
j_y	0	1000	575	m/s^3
j_z	1000	0	0	m/s^3

respectively, which is corresponding to the rms-resolutions of the inductive sensors after calibration (0.09-0.13 μm).

The position and angle errors at full speed and acceleration are measured on the trajectory $e - e'$ (see also Figure 7.21 and Table 7.3). The acceleration profile, the estimated power dissipation in the coils and the position and angle errors are shown in Figure 7.24. Figure 7.24 shows clearly the position dependency of the power dissipation. The tracking error of the HPPA is less than 30 μm and 0.1 mrad. The motion profile cannot be recognized in the position and angle errors. The x- and y-position errors of the translator after the motion has stopped (time>0.35 s) are remarkable. As this effect is mainly found in these two degrees-of-freedom, it is likely that these errors are caused by vibrations of the H-drive and measurement frame, which move simultaneously with the translator of the HPPA in the xy-plane.

Trajectory $f - f'$ (Figure 7.21 and Table 7.3) is chosen in such way that the translator moves through both the points in which 24 coils are active and the point in which only 15 coils are active. The acceleration profile, the estimated power dissipation in the coils and the position and angle errors are shown in Figure 7.25. The switching between the maximum and minimum number of active coils cannot be distinguished in the position and angle errors.

Figure 7.22. *Acceleration profile, estimated power dissipation and the position and angle errors of the translator of the HPPA during movement in the z-direction from 1.0 to 1.5 mm clearance at point d, which is indicated in Figure 7.21.*
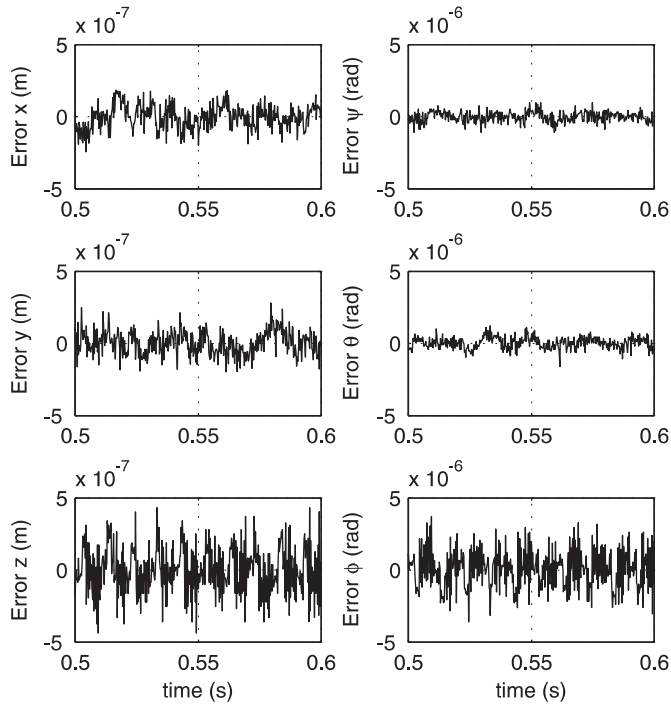
Figure 7.23. *Position and angle errors of the statically levitated HPPA at point d indicated in Figure 7.21, clearance: 1.5 mm.*

7.6 Conclusions

Force and torque measurements on the herringbone-pattern planar actuator (HPPA) show that, firstly, the force and torque can be accurately predicted with the models presented in chapter 3 and, secondly, the force and torque can be linearized and decoupled with the algorithm derived in chapter 4. When the HPPA is controlled with six SISO-controllers, the translator of the HPPA can be levitated at standstill with a position error which is corresponding to the sensor noise of the inductive measurement system. During fast movements in the xy-plane, position and angle errors of less than 30μm and 0.1 mrad were measured. A part of the position errors seems to originate from vibrations in the moving-measurement frame itself. Hence, the performance of the planar actuator is limited by the measurement system.
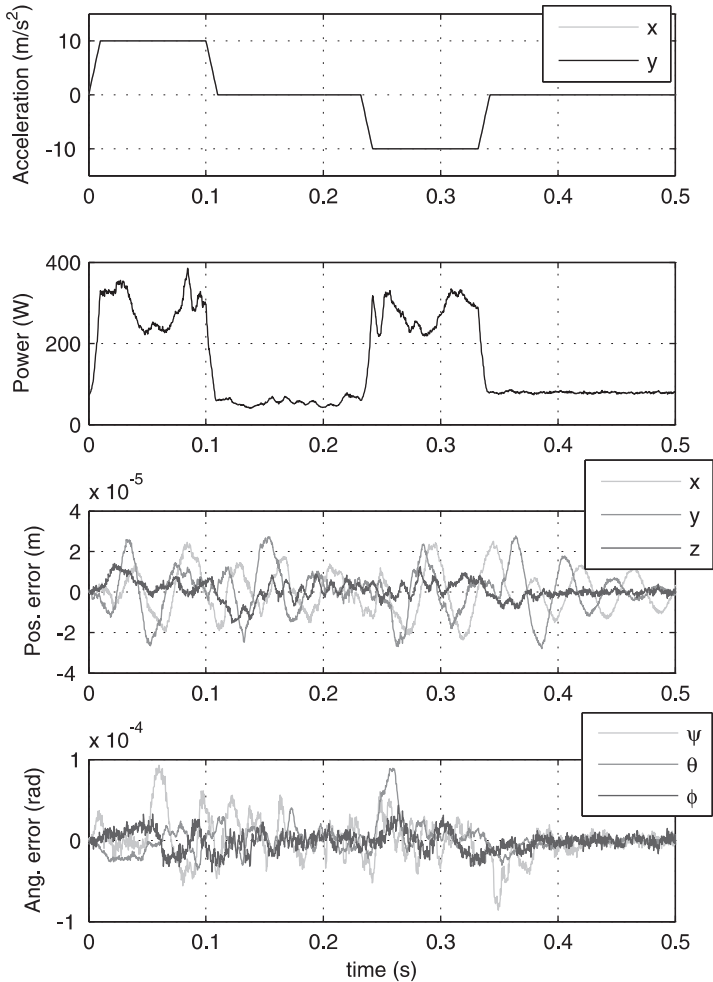
Figure 7.24. *Acceleration profile, estimated power dissipation and the position and angle errors of the translator of the HPPA during movement on trajectory $e - e'$ defined in Figure 7.21 and Table 7.3.*
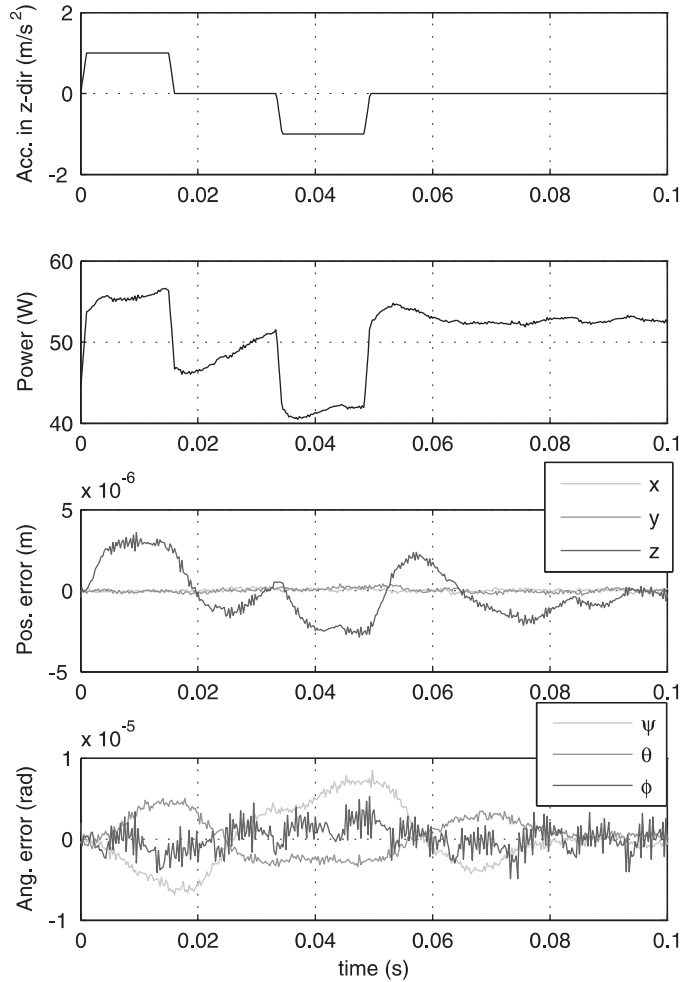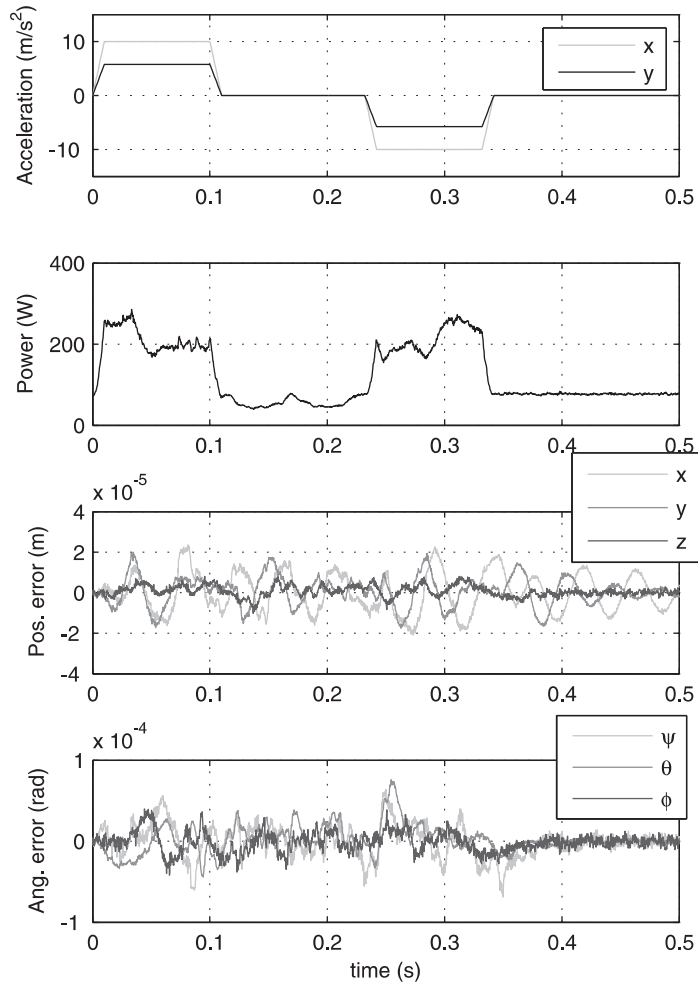
Figure 7.25. *Acceleration profile, estimated power dissipation and the position and angle errors of the translator of the HPPA during movement on trajectory $f - f'$ defined in Figure 7.21 and Table 7.3.*

Chapter 8

Conclusions and recommendations

In this thesis, long-stroke, magnetically levitated, planar actuators with moving magnets have been investigated. This research has resulted in a fully operational and successfully tested prototype. Both this thesis and [73] give a solid fundament to the electromagnetic analysis, commutation and design of this type of actuator.

The conclusions and the recommendations are grouped according to the sub-objectives, which are defined in section 1.2. Furthermore, an outlook is given towards future developments of the moving-magnet planar actuator.

8.1   Modeling of the force and torque

A framework consisting of three different magneto-static models for the prediction of the force and the torque in ironless moving-magnet planar actuators has been created. The three-dimensional models are based on the Lorentz force law and on two different analytical electromagnetical descriptions of the magnetic flux density distribution of the permanent magnets, i.e. magnetic surface charges and Fourier series. Using these models, the force and torque in large planar actuators with various magnet-array configurations and with concentrated windings can be predicted fast in comparison with e.g. FEM. The different models can be applied in all stages of the design process, and the analytical model can also be applied in the real-time controller of the planar actuator. Measurements on the realized planar actuator have shown that the force and the torque can be predicted accurately with all three models.

The end-effects of the magnet array have only been taken into account in

the model based on magnetic surface charges, as the two other models assume an infinitely large magnet array, which is modeled by Fourier series. This last assumption results in a significant reduction of the calculation time. An interesting addition to the modeling framework would be to create models which include the end-effects of the magnet array without a significant change of the calculation time compared with the Fourier series based models. The modeling framework can be easily adapted to other coreless linear and moving-coil planar actuators.

8.2   Commutation algorithm

The planar actuator has an active magnetic bearing and, consequently, all six degrees-of-freedom of the translator have to be controlled. The direct current-wrench decoupling algorithm has been derived to linearize and decouple the three force and the three torque components, and minimizes the ohmic losses in the planar actuator. This non-linear transformation is based on a simple analytical description of the planar actuator and not on large look-up tables. Because both the force and torque are decoupled, the coil currents are strongly non-sinusoidal, despite of the sinusoidal flux linkages of the coils. For that reason, all coils are connected to single-phase current amplifiers.

Only the coils near the edges and below the magnet array can exert force and torque on the translator of the planar actuator. During the movements of the translator in the xy-plane, the set of active coils is switched. As the analytical model in the mapping of the commutation algorithm assumes an infinitely long magnet array, a weighting function has been introduced to penalize the coils near the edges of the magnet array and to switch smoothly between different sets of active coils. Replacement of the analytical model by a model which includes the end-effects of the magnet array, could result in a reduction of the number of magnets required in the magnet array.

Simulations and measurements have demonstrated that the six degrees-of-freedom in the planar actuator can be decoupled with low force and torque ripples using the direct current-wrench decoupling algorithm.

8.3   Design methodology

Whereas classical machine designs are based on active length, stator bore, and the magnetic and electrical loading, planar actuator designs are dominated also by the levitated mass and the controllability. Design rules for the minimization of the power dissipation of planar actuators have been established by analyzing a single

coil and a magnet array. In this analysis, the planar actuator has been considered
as an assembly of independent Lorentz actuators. The results of this analysis are:

- Despite of the extra mass of the translator, moving-magnet planar actuators
  with a Halbach magnet array have generally a lower power dissipation than
  planar actuators with a NS array.
- Constructing planar actuators with four coils per three poles or three coils
  per two poles is a good choice to obtain a low power dissipation.

Based on the analysis of a single coil, four controllable planar actuator topolo-
gies have been synthesized: three topologies with rectangular coils arranged in a
herringbone pattern and 45 mechanical degrees rotated magnets and one topol-
ogy with square coils. The magnet array of all four actuators have a quasi-Halbach
magnetization. The power dissipation and the force and torque ripples of these
topologies have been compared. From this analysis it can be concluded that:

- In contrast to the topologies with rectangular coils, the force ripples of the
  planar actuator with square coils are dominated by force and torque compo-
  nents caused by the third harmonic component of the magnetic flux density
  distribution.
- The force ripples of the planar actuator with rectangular coils are domi-
  nated by the non-modeled cross-talk between the force production in the
  x- and y-directions.
- The difference between the power dissipation of the four topologies with
  the coil and magnet sizes obtained from the design rules and a multi-
  objective optimization is less than 2 %.

A planar actuator topology with rectangular coils and 45 degrees rotated magnets
has been selected for manufacturing. The actuator is named Herringbone Pattern
Planar Actuator (HPPA). Analysis of the magnetic fields in the HPPA has shown that
the working points of the permanent magnet in the quasi-Halbach magnet array
are scattered over the full second quadrant and partly the first quadrant of the BH-
curve. However, the risk of demagnetization due to external fields is small because
of the small armature reaction field.

The thermal design of the HPPA has received little attention in this thesis and
should be addressed in future research. Not only the materials (ceramics, wire-
wound coils, foil-wound coils, etc.), but also the interconnection among the tem-
perature, the motion profile and the path of the translator, and the possibilities to
reduce the thermal stress by taking into account the coil resistances in the commu-
tation algorithm, should be further investigated.

The design methodology does not optimize the topology of the planar actuator
itself. The optimization of the coil and magnet configuration of the planar actuator

and its scalability are also important subjects for future research.

8.4   Realization and test of the prototype

A prototype of the moving-magnet planar actuator has been successfully realized and tested. Six SISO controllers with a bandwidth of 35 Hz have been implemented for every degree-of-freedom. The translator can be levitated at standstill with a position error $< 0.5\mu$m and an angle error < 4 μrad. Measurements at high speeds (up to 1.4 m/s) also show low tracking errors (position error $< 30\mu$m, angle error < 0.1 mrad).

The performance of the HPPA is likely to be limited by the capabilities of measurement system. To investigate the actuator further it is advisable to remove the H-drive and install a measurement system which measures the position and orientation of the translator directly with respect to the stator coils, e.g. using laser interferometers.

8.5   Outlook towards future developments

8.5.1   Multiple translators above one stator

The realized planar actuator consists of one stator and one translator. With an appropriate measurement system, also multiple translators can be levitated above a single stator. Because cables to the translator are not required, there is also no risk of cables being tangled.

8.5.2   Full rotation about the z-axis

The stroke of the planar actuator in the z-direction and, as a result, also the rotations about the x- and y-axes, are fundamentally limited because the force capabilities of the planar actuator deteriorate when the clearance between the magnet array and the coils is increased. However, the functionality of the planar actuator can be extended with full rotation of the translator about the z-axis. This will increase the complexity of the design and the commutation algorithm severely as the force and torque are also a function of the ϕ-angle. As rectangular coils are only advantageous with a 45 degrees rotated magnet array, circular coils are probably more appropriate for such an actuator.

8.5.3 Planar actuator with function dependent coil configurations

Planar actuators will be designed to achieve a certain accuracy in a industrial process. However, this accuracy is only required for the process itself and not during, for example, transport in and out of the system. Consequently, the demands for the actuator will be depending on the location of the translator above the stator. It is a logical step to adapt the coil configuration of the stator to these different demands, for example, by applying less or larger coils in regions which require less accuracy. In this way costs for power amplifiers can be reduced.

8.5.4 Energy and data transfer

The advantage of a moving-magnet planar actuator over a moving-coil planar actuator is the absence of cables (although in some practical situations there might be a cable to remove charge). With a contactless energy supply and wireless communications, a manipulator on top of the translator of the planar actuator could be controlled while maintaining a contactless system. The energy to the manipulator can, for example, be transferred through an inductive link between the stator coils and pick-up coils on the translator of the planar actuator. Information of sensors can be communicated through radio, optical or inductive links. Because of the power dissipation on top of the translator, this system is especially suitable applications outside vacuum.

A project has already been started to investigate and demonstrate a planar actuator with a manipulator, which has a contactless energy supply and wireless data communications [37].

8.5.5 Long-stroke planar actuator with nanometer accuracy

Long-stroke nanometer positioning systems have usually a two-stroke concept. The system is subdivided in a long-stroke micrometer positioning system (stroke: 1 meter) and, onto that, a short-stroke nanometer positioning system is cascaded (stroke: several millimeters) [31]. Because of the magnetic bearing and the absence of cables, the translator of the moving-magnet planar actuator is mechanically isolated. Therefore, it would be of great interest to start a multi-disciplinary investigation of the accuracy limitations of long-stroke moving-magnet planar actuators in order to figure out if they can replace two-stroke nanometer positioning systems.

Appendix A

List of symbols

Symbol	Quantity	Unit
$\boldsymbol{\Gamma}$	planar actuator model	N/A, Nm/A
$\boldsymbol{\Delta}$	weighing matrix	-
ϵ_0	permittivity of vacuum	F/m
ϵ_t	emissivity	-
η	electrical angle	rad
θ	rotation angle	rad
Λ	flux linkage	Wb
λ	decay rate of the magnetic flux density	m^{-1}
μ	permeability	H/m
μ_0	permeability of vacuum	H/m
μ_r	relative permeability	-
ρ	mass density	kg/m^3
ρ_c	charge density	C/m^3
ρ_s	surface charge density	C/m^2
σ	conductivity	$1/(\Omega \cdot m)$
σ_{SB}	Stefan-Boltzmann constant	$W/(m^2 K^4)$
τ	magnet pole pitch	m
τ_c	coil pitch	m
τ_m	magnet pitch	m
τ_n	magnet pole pitch	m
ϕ	rotation angle	rad
Ψ	magnetic scalar potential	A

147

ψ	rotation angle	rad
ω	angular frequency	rad/s
A	area	m^2
$\vec{A}$	magnetic vector potential	Wb/m
a_k, a_l	Fourier coefficient	-
B_r	remanent magnetization	T
$\vec{B}$	magnetic flux density	V·s/m^2
b_k, b_l	Fourier coefficient	-
cb	conductor bundle width	m
ch	coil height	m
cl	coil length	m
cw	coil width	m
$\vec{D}$	electric flux density	A·s/m^2
d	distance	m
$\vec{E}$	electric field strength	V/m
$\vec{F}$	force	N
g	acceleration due to gravity	m/s^2
$\vec{H}$	magnetic field strength	A/m
h	convective heat transfer coefficient	W/(m^{2}K)
$\mathbf{I}$	identity matrix	-
i, $\vec{i}$	current	A
$\vec{J}$	current density	A/m^2
k	harmonic number	-
k	thermal conductivity	W/(m·K)
L, $\mathbf{L}$	inductance	H
l	harmonic number	-
l	length	m
M	mutual inductance	H
$\vec{M}$	magnetization	A/m
$\vec{M}_0$	residual magnetization	A/m
m	mass	kg
mh	magnet height	m
n	number	-
ocl	outer coil length	m
$\vec{P}$	polarization	C/m^2
p, $\vec{p}$	position	m
Q	electric charge	C

$\vec{q}$	position and orientation	m, rad
q_t	heat flux	W/m^2
R	resistance	Ω
R	thermal resistance	K/W
$\mathbf{R}$	orientation transformation matrix	-
$\vec{r}$	arm	m
S	surface	m^2
T	temperature	K
$\vec{T}$	torque	Nm
$\mathbf{T}$	transformation matrix	-
t	time	s
$u, \vec{u}$	voltage	V
V	volume	m^3
$v, \vec{v}$	velocity	m/s
$\vec{w}$	wrench	N, Nm
W_m	magnetic energy	J
x, y, z	Cartesian coordinates	m

Appendix B

3-DOF actuator with moving–magnets

In section 4.3, the commutation algorithm and the coil currents are demonstrated by means of a 3-DOF actuator with moving-magnets. This actuator [36] is a pre-prototype of the HPPA and used for initial validation of electromechanical models [41, 34], the commutation algorithm [75] and thermal models [77]. Figure B.1 shows the top and side views of the 3-DOF actuator. The three degrees-of-freedom of the actuator are translational movement in the x- and z-directions and rotational movement about the y-axis. The coils of the actuator are distributed according to a semi-four-phase system, i.e. $\tau_{cx} = \frac{3}{2}\tau_n$. The dimensions are listed in Table B.1. Figures B.2 and B.3 show photos of the translator and stator, respectively.

(a)

(b)
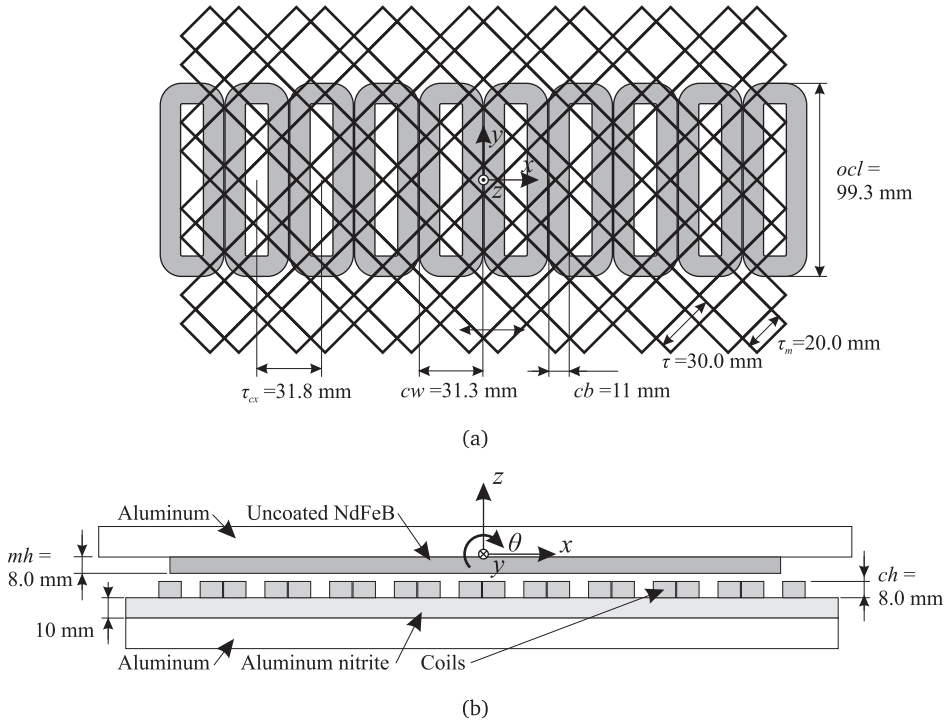
Figure B.1. *3-DOF actuator: a) Top view, b) side view.*
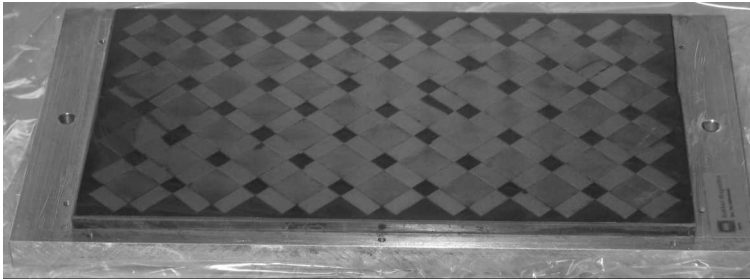
Figure B.2. *Magnet array of the 3-DOF actuator.*
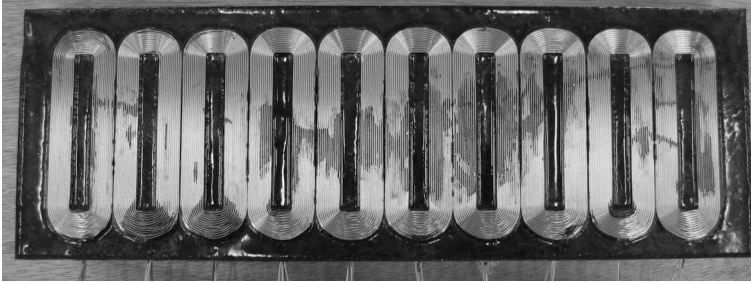
Figure B.3. *Coil array of the 3-DOF actuator.*

Table B.1. *Dimensions and properties of the 3-DOF actuator*

Parameter	Value	Unit
Pole pitch, τ	30.0	mm
Magnet size ratio, τ_m/τ	$\frac{2}{3}$	-
Magnet height, mh	8.0	mm
Outer length coil, ocl	99.3	mm
Outer width coil, cw	31.3	mm
Coil pitch (x-direction), τ_{cx}	$\frac{3}{2}\tau_n = 31.8$	mm
Coil height, ch	8	mm
Conductor bundle width, cb	11	mm
Number of turns	348	-
Total mass translator, m	5.6	kg

Appendix C

Material and equipment properties

Table C.1. *Properties of the coils*

Material	Copper
Wire diameter	0.45 mm
Number of turns	319
Resistance (20 °C)	5.7 Ω
Self-inductance	3.8 mH
Thermal conductivity (perpendicular to the current)	1.1 W m^{-1} K^{-1} [77]
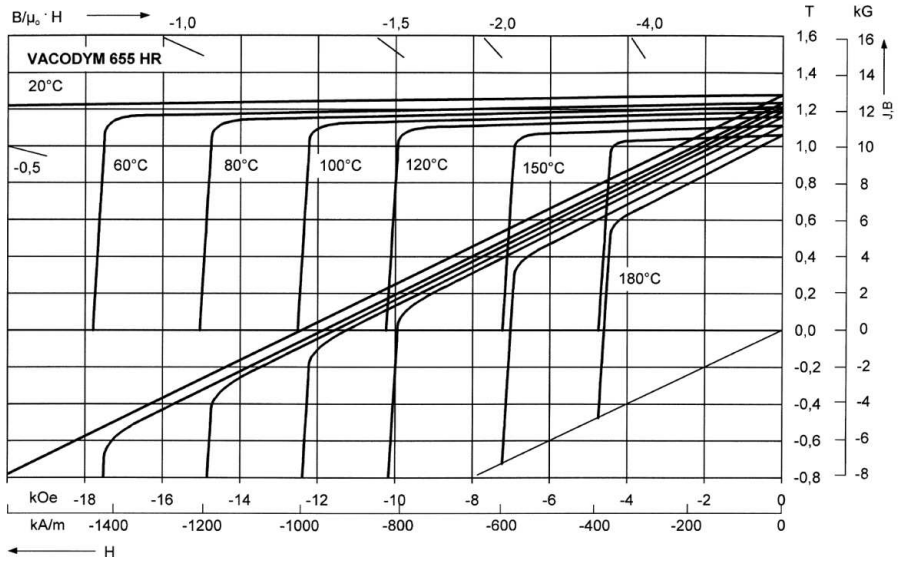
Figure C.1. *BH-curve of VACODYM 655 HR [72].*

Table C.2. *Physical properties of the permanent magnets*

Supplier	Vacuumschmelze
Type	VACODYM 655 HR
Material	NdFeB
Remanence (measured by supplier)	1.24 T
Relative permeability	1.03-1.05
Mass density	$7.7 \cdot 10^3$ kg m^{-3}
Resistivity	$1.2 - 1.6 \cdot 10^{-6}$ Ωm
Thermal conductivity	9 W m^{-1} K^{-1}

Table C.3. *Physical properties of aluminum*

Mass density	$2.7 \cdot 10^3$ kg m^{-3}
Thermal conductivity	235 W m^{-1} K^{-1}
Resistivity (20 °C)	$2.8 \cdot 10^{-8}$ Ωm

Table C.4. *Physical properties of the stator casting resin*

Supplier	Huntsman Advanced Materials
Type	RenCast CW 5156-1 REN HY 5158
Mass density	$1.62 \cdot 10^3$ kg m^{-3}
Thermal conductivity (estimated by supplier)	0.6-0.9 W m^{-1} K^{-1}

Table C.5. *Properties of the power amplifiers of the planar actuator*

Supplier	Prodrive
Type	PADC3AX52/6
Converter type	PWM
Bandwidth	4.0 kHz
Current (rms)	2 A
Current (max)	± 6 A
Voltage (max)	± 52 V
Interface	RS485 (1.5 Mbit)
DC-link	PSDC 59V-22A

Table C.6. *Properties of the eddy-current sensors*

Supplier	Lion inductive
Probe	U8B
Driver	ECL100
Range	2 mm
Resolution (rms)	0.16 μm
Linearity	$\pm$0.25 %
Error band	$\pm$0.5 %
Anti-aliasing filters	8th order Butterworth
Cut-off frequency of filters	2.5 kHz

Table C.7. *Properties of the DSP system*

Supplier	dSPACE
Type	DS1005-MP
Number of processors	2

Bibliography

[1] J. H. J. Almering, et al., *Analyse*. Delft uitgevers maatschappij, 1993.

[2] T. Asakawa, "Two-dimensional precise positioning device for use in a semi-conductor manufacturing apparatus," U.S. Patent 4,535,278, Aug. 13, 1985.

[3] M. S. Bazaraa, H. D. Sherali, and C. M. Shetty, *Nonlinear programming, theory and algorithms*, 2nd ed. Hoboken, NJ: John Wiley & Sons, 1993.

[4] M. B. Binnard, "Planar motor with linear coil arrays," U.S. Patent 6,445,093, Sep. 3, 2002.

[5] M. B. Binnard, "Six degree of freedom control of planar motors," U.S. Patent Application 2003/0 085 676, May 8, 2003.

[6] K. J. Binns, P. J. Lawrenson, and C. W. Towbridge, *The analytical and numerical solutions of electrical and magnetic fields*. Chichester, England: John Wiley & Sons, 1994.

[7] R. F. Burton, *The book of thousand nights and a night*. London, UK: The Burton club, 1885.

[8] *FLUX3D 9.30 User's guide*, Cedrat, Meylan, France, 2006.

[9] H. S. Cho, C. H. Im, and H. K. Jung, "Magnetic field analysis of 2-d permanent magnet array for planar motor," *IEEE Trans. Magn.*, vol. 37, no. 56, pp. 3762–3766, Sep. 2001.

[10] H. S. Cho and H. K. Jung, "Analysis and design of synchronous permanent-magnet planar motors," *IEEE Trans. Energy Conversion*, vol. 17, no. 4, pp. 492–499, Dec. 2002.

[11] J. H. Choi, J. H. Park, and Y. S. Baek, "Design and experimental validation of performance for a maglev moving-magnet-type synchronous pm planar motor," *IEEE Trans. Magn.*, vol. 42, no. 10, pp. 3419–3421, Oct. 2006.

[12] J. C. Compter, "Introductie electromechanica," Philips Centre for Industrial Technology (CFT), CTR 593-00-0022, Aug 2000.

[13] J. C. Compter, "Electro-dynamic planar motor," *Precision Engineering*, vol. 28, no. 2, pp. 171–180, Apr. 2004.

[14] J. C. Compter and P. C. M. Frissen, "Displacement device," Patent WO 01/18 944 A1, Mar. 15, 2001.

[15] J. C. Compter, P. C. M. Frissen, and J. van Eijk, "Displacement device," Patent WO 2006/075 291 A2, Jul. 20, 2006.

[16] J. C. Compter, J. W. Jansen, E. A. Lomonova, and A. J. A. Vandenput, "Six degrees-of-freedom planar motors," in *Proc. of 4th EUSPEN International Conference*, Glasgow, Scotland (UK), Jun. 2004, pp. 390–391.

[17] E. Durand, *Magnétostatique*. Paris, France: Masson et Cie, 1968.

[18] S. Earnshaw, "On the nature of the molecular forces which regulate the constitution of the luminuferous ether," *Trans. Camb. Phil. Soc.*, vol. VII:1, pp. 97–112, 1842.

[19] I. Etxaniz, A. Izpizua, M. S. Martin, J. Arana, and M. Axpe, "Design of magnetically levitated 2D drive," *COMPEL-lnt. J. Comput. & Math. Electr. & Electron. Eng.*, vol. 25, no. 3, pp. 732–740, 2006.

[20] A. A. F. Filho, A. A. Susin, and M. A. da Silveira, "Magnetic field analysis of 2-d permanent magnet array for planar motor," *IEEE Trans. Magn.*, vol. 39, no. 5, pp. 3364–3366, Sep. 2003.

[21] N. Fujii and M. Fujitake, "Two-dimensional drive characteristics by circular shaped motor," *IEEE Trans. Ind. Applicat.*, vol. 35, no. 4, pp. 803–809, Jul./Aug. 1999.

[22] E. P. Furlani, *Permanent magnet and electromechanical devices*. San Diego, CA: Academic Press, 2001.

[23] J. F. Gieras and M. Wing, *Permanent magnet motor technology*, 2nd ed. New York, NY: Marcel Dekker, Inc, 2002.

[24] S. Gurol and B. Baldi, "Overview of the general atomics urban magnlev technology development program," in *Proc of the 2004 ASME/IEEE Joint Rail Conference*, Baltimore, MD, Apr. 2004, pp. 187–191.

[25] K. Halbach, "Design of permanent multipole magnets with oriented rare earth cobalt material," *Nucl. Instr. meth.*, vol. 169, pp. 1–10, 1980.

[26] D. Hanselmann, *Brushless permanent magnet motor design*, 2nd ed. Cranston, Rhode Island, USA: The writers' collective, 2003.

[27] W. H. Hayt, *Engineering electromagnetics*, 5th ed. New York, USA: McGraw-Hill Book Company, 1989.

[28] A. J. Hazelton, M. B. Binnard, and J. M. Gery, "Electric motors and positioning devices having moving magnet arrays and six degrees of freedom," U.S. Patent 6,208,045, Mar. 27, 2001.

[29] J. R. Hendershot, jr. and T. J. E. Miller, *Design of brushless permanent-magnet motors*. Hillsboro, OH: Magna Physics Publishing, 1994.

[30] W. E. Hinds, "Single plane orthogonally moveable drive system," U.S. Patent 4,654,571, Mar. 31, 1987.

[31] S. A. J. Hol, "Design and optimization of a magnetic gravity compensator," Ph.D. dissertation, Eindhoven University of Technology, 2004.

[32] R. A. Horn and C. R. Johnson, *Matrix analysis*. Cambridge, UK: Cambridge university press, 1999.

[33] J. W. Jansen, E. A. Lomonova, A. J. A. Vandenput, and J. C. Compter, "Design tool for a 6-dof planar motor with moving permanent magnets and standstill coils," in *Proc. of the 4th international symposium on linear drives for industrial applications*, Birmingham, UK, Sep. 2003, pp. 93–96.

[34] J. W. Jansen, E. A. Lomonova, A. J. A. Vandenput, and C. M. M. van Lierop, "Analytical model of a magnetically levitated linear actuator," in *Conference Record of the 2005 Industry Applications Conference 40th Annual Meeting*, Hong Kong, Oct. 2005, pp. 2107–2113.

[35] J. W. Jansen, E. A. Lomonova, A. J. A. Vandenput, and C. M. M. van Lierop, "Design flow for a six degree-of-freedom planar actuator," in *Proc. of th 3rd IEEE Young Researchers Symposium in Electrical Power Engineering*, Ghent, Belgium, Apr. 2006.

[36] J. W. Jansen, J. M. van Essen, C. M. M. van Lierop, E. A. Lomonova, and A. J. A. Vandenput, "Design and test of an ironless, three degree-of-freedom, magnetically levitated linear actuator with moving magnets," in *IEEE Int. Electric Machines and Drives Conference (IEMDC'05)*, San Antonio, Texas, May 2005, pp. 93–96.

[37] J. W. Jansen, C. M. M. van Lierop, J. de Boeij, E. A. Lomonova, J. L. Duarte, and A. J. A. Vandenput, "Moving magnet multi-DOF planar actuator technology with contactless energy and data transfer," in *Proc. of the 6th international symposium on linear drives for industrial applications*, invited, Sep 2007.

[38] J. W. Jansen, C. M. M. van Lierop, and E. A. Lomonova, "Werkwijze voor het vervaardigen van een vlakke actuator alsmede een vlakke actuator aldus vervaardigd," Dutch Patent Application 1 029 246, Jun. 14, 2005.

[39] J. W. Jansen, C. M. M. van Lierop, E. A. Lomonova, and A. J. A. Vandenput, "Comparison of six-DOF planar actuator topologies," in *Proc. of the 16th international symposium on the computation of electromagnetic fields*, Aachen, Germany, June 2007, pp. 15–16.

[40] J. W. Jansen, C. M. M. van Lierop, E. A. Lomonova, and A. J. A. Vandenput, "Magnetically levitated planar actuator with moving magnets," in *IEEE Int. Electric Machines and Drives Conference (IEMDC'07)*, Antalya, Turkey, May 2007, pp. 272–278.

[41] J. W. Jansen, C. M. M. van Lierop, E. A. Lomonova, and A. J. A. Vandenput, "Modeling of magnetically levitated planar actuators with moving magnets," *IEEE Trans. Magn.*, vol. 43, no. 1, pp. 15–25, Jan. 2007.

[42] J. W. Jansen, C. M. M. van Lierop, E. A. Lomonova, and A. J. A. Vandenput, "Ironless magnetically levitated planar actuator," *J. Appl. Phys.*, in press.

[43] J. W. Jansen, C. M. M. van Lierop, E. A. Lomonova, and A. J. A. Vandenput, "Magnetically levitated planar actuator with moving magnets," *IEEE Trans. Ind. Applicat.*, in press.

[44] B. V. Jayawant, "Electromagnetic suspension and levitation techniques," *Proc. R. Soc. Lond.*, vol. A, no. 416, pp. 245–320, Apr. 1988.

[45] K. S. Jung and Y. S. Baek, "Precision stage using a non-contact planar actuator based on magnetic suspension technology," *Mechatronics*, vol. 13, no. 8-9, pp. 981–999, 2003.

[46] E. M. H. Kamerbeek, "On the theoretical end experimental determination of the electromagnetic torque in electrical machines," Ph.D. dissertation, Technische Hogeschool Eindhoven, 1970.

[47] K. Kemp and S. Wurm, "EUV lithography," *Comptes Rendus Physique*, vol. 7, pp. 875–886, 2006.

[48] W. J. Kim, "High-precision planar magnetic levitation," Ph.D. dissertation, Massachusetts Institute of Technology, 1997.

[49] N. Korenaga, "Alignment apparatus and exposure apparatus using the same," U.S. Patent 7,075,198, Jul. 11, 2006.

[50] W. L. L. Lenders, "The orthocyclic method of coil winding," *Philips technical review*, pp. 365–379, 1961/1962.

[51] E. Levi, *Polyphase motors*.   New York, NY: John Wiley, 1984.

[52] P. J. McKerrow, *Introduction to robotics*.   Syndney, Australia: Addison-Wesley Publishers Ltd., 1991.

[53] A. F. Mills, *Basic heat and mass transfer*, 2nd ed.   Upper Saddle River, NJ: Prentivce Hall, 1999.

[54] H. Ohsaki and Y. Ueda, "Numerical simulation of mover motion of a surface motor using halbach permanent magnets," in *Proc. Int. Symposium on Power Electronics, Electrical Drives, Automation and Motion, SPEEDAM 2006*, Taormina, Italy, May 2006, pp. 364–367.

[55] C. M. Ong, *Dynamic simulation of electric machinery*.   Upper Saddle River, NJ: Prentice Hall PTR, 1998.

[56] R. H. Park, "Two-reaction theory of synchronous machines - generalized method of analysis - part i," *AIEE Trans.*, vol. 48, pp. 716–730, Jul. 1929.

[57] M. P. Perry, "Eddy current damping due to a linear periodic array of magnetic poles," *IEEE Trans. Magn.*, vol. 20, pp. 149–155, 1984.

[58] "Maglev planar stage," Philips Applied Technologies, Eindhoven, The Netherlands, 2006.

[59] *ACM Micro Service manual*, Philips EMT, Eindhoven, The Netherlands, 2001.

[60] W. Potze and P. C. M. Frissen, "Method for controlling an electric motor, control unit and electri motor," Patent WO 2006/054 243 A2, May 26, 2006.

[61] C. R. Rao and S. K. Mitra, *Generalized inverse of matrices and its applications*. Wiley, 1971.

[62] M. N. O. Sadiku, *Electromagnetics*, 2nd ed. New York, USA: Oxford University Press, Inc., 1995.

[63] K. Sawada, "Devlopment of magnetically levitated high speed transport system in Japan," *IEEE Trans. Magn.*, vol. 32, no. 4, pp. 2230–2235, Jul. 1986.

[64] B. A. Sawyer, "Magnetic positioning device," U.S. Patent 3,376,578, Apr. 2, 1968.

[65] C. Schäffel, "Untersuchungen zur gestaltung integrierter mehrkoordinatenantriebe," Ph.D. dissertation, TU Ilmenau, 1996.

[66] H. M. J. R. Soemers, "The design of high performance manipulators," in *Proc. of the 2001 IEEE/ASME Int. Conf. on Advanced Intelligent Mechatronics*, Como, Italy, Jul. 2001, pp. 149–152.

[67] R. L. Stoll, *The analysis of eddy currents*. Oxford, UK: Oxford University Press, 1974.

[68] T. Teng, T. Ueda, S. Makinouchi, and B. Yuan, "Moving magnet type planar motor control," in *Proc. of the 1st Int. Conf. on Positioning Technology*, Hamamatsu, Japan, Jun. 2004, pp. 203–208.

[69] D. L. Trumper, W. J. Kim, and M. E. Williams, "Design and analysis framework for linear permanent-magnet machines," *IEEE Trans. Ind. Applicat.*, vol. 32, no. 2, pp. 371–379, Mar./Apr. 1996.

[70] Y. Ueda and H. Ohsaki, "Positioning charcteristics of a coreless surface motor using halbach permanent magnet array," in *Proc. of the 4th international symposium on linear drives for industrial applications*, Kobe, Japan, Sep. 2005, pp. 270–273.

[71] Y. Ueda and H. Ohsaki, "Positioning charcteristics of a coreless surface motor using halbach permanent magnet array," in *Proc. Power Conversion Conference, PCC '07*, Nagoya, Japan, Apr. 2007, pp. 614–621.

[72] "Rare earth permanent magnets, vacodym - vacomax," Vacuumschmelze, Hanau, Germany, 2003.

[73] C. M. M. van Lierop, "Magnetically levitated planar actuator with moving magnets," Ph.D. dissertation, Eindhoven University of Technology, 2008.

[74] C. M. M. van Lierop, J. W. Jansen, A. A. H. Damen, E. A. Lomonova, P. P. J. van den Bosch, and A. J. A. Vandenput, "Model based commutation of a long-stroke magnetically levitated linear actuator," in *Conference record of the 2006 IEEE Industry Applications Conference 41st Annual Meeting*, Tampa, Florida, Oct. 2006.

[75] C. M. M. van Lierop, J. W. Jansen, A. A. H. Damen, and P. P. J. van den Bosch, "Control of multi-degree-of-freedom planar actuators," in *Proc. of the 2006 IEEE International Conference on Control Applications, CCA 2006*, Munich, Germany, Oct. 2006, pp. 2516–2521.

[76] C. M. M. van Lierop, J. W. Jansen, E. A. Lomonova, A. A. H. Damen, P. P. J. van den Bosch, and A. J. A. Vandenput, "Commutation of a magnetically levitated planar actuator with moving magnets," in *Proc. of the 6th international symposium on linear drives for industrial applications*, Sep 2007.

[77] J. Vissers, J. W. Jansen, and E. A. Lomonova, "Thermal modeling of a 3-dof linear actuator with moving magnets," in *Proc. of th 3rd IEEE Young Researchers Symposium in Electrical Power Engineering*, Ghent, Belgium, Apr. 2006.

[78] J. P. Yonnet and G. Akoun, "3D analytical calculation of the forces exerted between two cuboidal magnets," *IEEE Trans. Magn.*, vol. 20, no. 5, pp. 1962–1964, 1984.

[79] Z. Q. Zhu and D. Howe, "Halbach permanent magnet machines and applications: a review," *IEE Proc. on Electric Power Applications*, vol. 148, pp. 229–308, 2001.

[80] Z. Q. Zhu, D. Howe, E. Bolte, and B. Ackermann, "Instantaneous magnetic field distribution in brushless permanent magnet dc motors, part 1: open-circuit field," *IEEE Trans. Magn.*, vol. 29, pp. 124–135, 1993.

Samenvatting

Door de steeds verdergaande miniaturisatie in bijvoorbeeld de halfgeleiderindustrie, moeten onderdelen tijdens de productie steeds nauwkeuriger en sneller worden gepositioneerd. Voor het verplaatsen van een object in het horizontale vlak (het xy-vlak), wordt vaak gebruik gemaakt van een systeem dat bestaat uit aan elkaar gekoppelde lineaire motoren. In plaats daarvan kan ook een magnetisch gelagerde planaire actuator worden toegepast, waarmee rechtstreeks een xy-beweging kan worden gemaakt. De translator, het bewegende deel, wordt hierbij slechts ondersteund door magnetische velden. Door het magnetisch lager kan de translator niet alleen in het xy-vlak bewegen, maar kan hij ook kleine roterende bewegingen maken en kan de hoogte waarop hij zweeft worden gevarieerd. De translator beweegt dus met zes vrijheidsgraden.

Dit proefschrift behandelt de elektromechanische analyse en het ontwerp van een contactloze, magnetisch gelagerde planaire actuator met bewegende magneten. De spoelen van de actuator liggen op de vaste wereld en hebben geconcentreerde niet-overlappende windingen. De magneten zijn in een schaakbordpatroon op de translator gelijmd en hebben een quasi-Halbach magnetisatie. Omdat er geen kabels aan het bewegende deel zitten, wordt deze actuator ook wel vergeleken met een vliegend tapijt. Alleen de spoelen die zich op een bepaald ogenblik onder de magneten bevinden, kunnen efficiënt gebruikt worden om de translator op te tillen en te bewegen. Om een lange slag in het xy-vlak te kunnen maken, wordt de set actieve spoelen steeds aangepast aan de positie van de magneetplaat. De slag van de actuator kan simpelweg worden vergroot door het aantal statorspoelen uit te breiden.

De planaire actuator bevat geen ijzer en heeft een driedimensionale, nietperiodieke structuur zonder symmetrieën. De analyse van deze actuator vraagt om een multi-disciplinaire aanpak. Om de krachten en de koppels die op de translator werken te bepalen zijn drie verschillende magnetostatische modellen ontwikkeld.

Deze modellen zijn gebaseerd op de berekening van de Lorentz kracht. Hierbij wordt het magneetveld van de permanente magneten steeds analytisch berekend en zijn zowel analytische als numerieke technieken gebruikt om Lorentz kracht uit te rekenen. Met behulp van deze modellen, die voornamelijk verschillen in nauwkeurigheid en snelheid, kunnen planaire actuatoren geanalyseerd, ontworpen en geregeld worden.

In de planaire actuator zijn het magnetische lager en de voortbeweging van de translator in het xy-vlak niet fysiek gescheiden maar gecombineerd. Standaard commutatietechnieken, die normaal gebruikt worden voor synchrone permanent-magneet motoren, kunnen daarom niet worden toegepast om de krachten en koppels in de planaire actuator te lineariseren en te ontkoppelen. Om dit wel te bereiken wordt in de regelaar van de planaire actuator continu een analytische uitdrukking van de krachten en koppels, die uitgeoefend worden door de individuele actieve spoelen, geïnverteerd en wordt tegelijkertijd de energie in het systeem geminimaliseerd. Met behulp van gladde weegfuncties wordt geschakeld van de ene naar de andere spoelset. De vorm van de stromen in de spoelen is niet sinusoïdaal. Elke spoel heeft daarom zijn eigen stroombron.

Het ontwerp van de planaire actuator is in twee stappen uitgevoerd. Allereerst is naar de vermogensdissipatie in de actuator gekeken. Om deze zo klein mogelijk te houden zijn de maten van de spoelen en magneten geoptimaliseerd zodat ze zo efficiënt mogelijk kracht produceren. Hiervoor zijn ontwerpregels opgesteld. Vervolgens zijn verschillende actuatorconfiguraties gesynthetiseerd waarbij gebruik is gemaakt van deze geoptimaliseerde spoelen en magneten. De vermogensdissipatie en de kracht- en koppelrimpels van deze verschillende configuraties zijn vergeleken en verschillende oorzaken van de deze rimpels zijn geïdentificeerd.

Op basis van de vergelijking van de verschillende actuatoren is een planaire actuator met rechthoekige spoelen in een visgraatpatroon uitgekozen en gebouwd. De actuator heeft 84 statorspoelen waarvan er hoogstens 24 tegelijkertijd actief zijn. De magnetostatische modellen en het commutatie-algoritme zijn geverifieerd en de actuator is met succes getest.

Dankwoord
Acknowledgements

Met het schrijven van het dankwoord, is er een eind gekomen aan een periode waarin het idee van een zwevend tapijt van permanente magneten is omgezet naar een werkend prototype. Dit was nooit gelukt zonder Nelis van Lierop, mijn collega promovendus, met wie ik vier jaar lang intensief en met veel plezier aan dit project heb gewerkt. Ik had me geen betere projectpartner kunnen wensen. Bedankt!

Ik wil André Vandenput bedanken voor de mogelijkheid om op dit onderwerp te kunnen promoveren en zijn jarenlange begeleiding en ondersteuning. Veel dank ben ik verschuldigd aan Elena Lomonova. Haar grote toewijding, de vele nuttige discussies en ideeën hebben veel bijgedragen aan het uiteindelijk resultaat. Je was een belangrijke bron van motivatie. Ook wil ik Paul van den Bosch en Ad Damen bedanken voor hun vertrouwen in het werk en hun waardevolle commentaar.

De overige kerncommissieleden, Dave Howe, John Compter en Maarten Steinbuch, wil ik bedanken voor hun tijd om mijn proefschrift te lezen en voor hun nuttige suggesties. I want to say a special word of thank to Dave Howe for traveling to Eindhoven. Ik wil Michel Antal bedanken voor het zitting nemen in mijn promotiecommissie en zijn inzet voor IOP-EMVT.

Ik wil Marijn Uyt De Willigen bedanken voor het vele werk dat hij heeft verzet in het laboratorium. Praktische problemen werden door jou altijd snel en vakkundig opgelost en je zorgde altijd voor een goede sfeer. Het bouwen van dit soort opstellingen kan niet zonder de hulp van veel leveranciers. De Gemeenschappelijk Technische Dienst van de TU/e heeft ons veel werk uit handen genomen. Met name wil ik Jovita Moerel en Patrick de Laat bedanken voor hun flexibiliteit en hun inspanningen om onze constructieproblemen op te lossen. Een aantal bedrijven heeft speciaal voor ons onderdelen gemaakt of aangepast. In het bijzonder wil ik hiervoor Korneel Wijnands (Prodrive), Mark van den Broek (Vacuumschmelze),

Peter Krechting (Tecnotion), Ad Vermeer (Assembléon) en Peter van Gils (ASML) bedanken.

Ook stagaires en afstudeerders hebben veel nuttig werk verricht in het project. Ik wil hiervoor met name Justin van Essen, Jochem Vissers, Jan Schellekens en Angelino Eijgermans bedanken.

Kamergenoot Paul Wingelaar wil ik bedanken voor de gezellige tijd die ik de afgelopen vier jaar op de TU/e heb gehad. Als laatste wil ik mijn familie en vrienden bedanken voor de steun tijdens de afgelopen jaren.

Curriculum Vitae

Helm Jansen was born on 3rd July 1978, in Wijchen, The Netherlands. Het attended secondary school at Dominicus College, Nijmegen. In 2003 he received his M.Sc. degree in Electrical Engineering (with honours) from the Eindhoven University of Technology, The Netherlands. In the summer of 2002 he was a trainee in the Electrical Machines and Drives group (EMD) at the University of Sheffield, UK and investigated a fault tolerant generator for aircraft application. He conducted his Master thesis in the Electromechanics and Power Electronics group (EPE) at the Eindhoven University of Technology from October 2002 to June 2003. The subject of this thesis was the preliminary investigation of a magnetically levitated planar actuator. For this work, he was awarded the KIvI-E prize. From July 2003 he continued his research in the field of moving-magnet planar actuators in the EPE-group and started working towards his Ph.D. degree, which resulted in this thesis.